NIST Technical Note
NIST TN 2162r1

The Global and Local Structure of Medium-Scale Pool Fires

Kunhyuk Sung
Ryan Falkenstein-Smith
Matthew Bundy
Marco Fernandez
Anthony Hamins

This publication is available free of charge from:
https://doi.org/10.6028/NIST.TN.2162r1

NATIONAL INSTITUTE OF STANDARDS AND TECHNOLOGY
U.S. DEPARTMENT OF COMMERCE

NIST Technical Note
NIST TN 2162r1

The Global and Local Structure of Medium-Scale Pool Fires

Kunhyuk Sung
Ryan Falkenstein-Smith
Matthew Bundy
Marco Fernandez
Anthony Hamins
Fire Research Division
Engineering Laboratory

This publication is available free of charge from:
https://doi.org/10.6028/NIST.TN.2162r1

October 2024

U.S. Department of Commerce
Gina M. Raimondo, Secretary

National Institute of Standards and Technology
Laurie E. Locascio, NIST Director and Under Secretary of Commerce for Standards and Technology

NIST TN 2162r1
October 2024

Certain equipment, instruments, software, or materials, commercial or non-commercial, are identified in this paper in order to specify the experimental procedure adequately. Such identification does not imply recommendation or endorsement of any product or service by NIST, nor does it imply that the materials or equipment identified are necessarily the best available for the purpose.

Publication History
Approved by the NIST Editorial Review Board on 2024-02-01
Supersedes NIST TN 2162 (June 2021) https://doi.org/10.6028/NIST.TN.2162

How to Cite this NIST Technical Series Publication
Kunhyuk Sung, Ryan Falkenstein-Smith, Matthew Bundy, Marco Fernandez, Anthony Hamins (2024) The Global and Local Structure of Medium-Scale Pool Fires. (National Institute of Standards and Technology, Gaithersburg, MD), NIST Technical Note (TN) 2162r1. https://doi.org/10.6028/NIST.TN.2162r1

Author ORCID iDs
Kunhyuk Sung: 0000-0002-0937-2332
Ryan Falkenstein-Smith: 0000-0001-7039-5835
Matthew Bundy: 0000-0002-1138-0307
Marco Fernandez: 0000-0002-4227-8866
Anthony Hamins: 0000-0001-7531-4256

Contact Information
anthony.hamins@nist.gov

Abstract

A series of experiments are reported that characterize key features of the structure of eight medium-scale pool fires (0.3 m to 0. 4 m) steadily burning a variety of liquid and gaseous fuel types, including 30 cm diameter liquid pool fires burning methanol, ethanol, acetone and heptane, and 37 cm diameter methane (34 kW) and propane (20 kW, 34 kW, and 50 kW) gaseous pool fires. The measurements and their uncertainty help establish a data repository for use in the rigorous evaluation of computational fluid dynamics fire models.

Steadily burning liquid and gaseous pool fires were established on water-cooled burners. After a 5 min to 10 min warm-up period, global and local measurements of the fires were conducted. The global measurements reported here include flame height, puffing frequency, mass burning rate, heat release rate, CO and soot yields, radiative fraction, and total heat feedback fraction to the burner. The local measurements reported here include the profiles of radiative and total heat flux onto the liquid pool surface, the radiative heat flux distribution to an array of flux gauges forming a cylindrical control surface around the fire, the fuel surface temperature, in-depth temperature at select locations inside the liquid pools, and the vertical and temperature centerline profiles above the fuel surface.

Many of the measurements reported here are new; some have been previously reported but are included here for completeness. Measurements of the centerline soot mass fractions and gas species profiles for these fires are available in complementary publications. In summary, the measurement results provide a comprehensive data set for the evaluation of computational fire models and offer insight on the complex structure of medium-scale pool fires.

Keywords

gas temperature; model validation; plume velocity; pool fires; radiative fraction.

Table of Contents

List of Tables

List of Figures

Preface to the Second Edition

The original version of this National Institute of Standard and Technology (NIST) Technical Note (TN 2162) was published in June 2021 and reported on a series of experiments in seven medium-scale liquid and gaseous pool fires including 30 cm diameter methanol, ethanol, acetone, and heptane liquid pool fires and 37 cm diameter gaseous methane (34 kW) and propane (20 kW and 34 kW) pool fires. The measurement results reported in the original edition of the report included the fuel mass burning rates and detailed profiles of the local temperature and velocity measured as a function of distance along the centerline above the burner surface. Bidirectional probe and thermocouple temperature measurements characterized the upward speed in the plumes of the pool fires. Fine, bare-bead thermocouples were used to characterize the local gas-phase temperature. A single-location radiative heat flux measurement was used to estimate the radiative fraction (χ_{rad}) in the 30 cm diameter methanol pool fires.

This edition of the report builds upon the original. Measurement results for a 37 cm diameter, 50 kW propane fire are included in this edition. This edition also significantly increases the types of measurements reported to include the time-averaged flame height, puffing or pulsation frequency, CO and soot yields, the profiles of radiative and total heat flux onto the liquid pool surface, the total heat feedback fraction to the fuel (or burner) surface, the temperature at select locations inside the liquid pools, the surface temperatures of the liquid fuel and the gaseous burner, and the radiative heat flux distribution to an array of heat flux gauges forming a cylindrical control surface about the fire. Single-location radiative heat flux measurements are reported as estimates of the radiative fraction (χ_{rad}) for all eight fires considered here. The results in this document have been checked for accuracy, consistency and uncertainty and supersede previously published results.

Acknowledgements

The authors are very grateful to Sung Chan Kim (Kyung-IL University, South Korea) and K.Y. Lee (Andong National University, South Korea) for their contributions to the measurements and their insight. The authors are indebted to Laurean DeLauter, Tony Chakalis, and Phil Deardorff of NIST for their outstanding technical assistance.

Author Contributions

Kunhyuk Sung: Software, Methodology, Investigation, Formal Analysis, Data curation, Validation, Writing- Original draft preparation and Editing. **Ryan Falkenstein-Smith**: Investigation. **Matthew Bundy**: Supervision, Software, Data curation, Methodology. **Marco Fernandez**: Investigation. **Anthony Hamins**: Supervision, Conceptualization, Methodology, Investigation, Formal Analysis, Validation, Writing- Original draft preparation, Reviewing and Editing.

1. Overview of NIST Pool Fire Data

This report describes a series of experiments to characterize medium-scale pool fires. This study is part of a larger body of work characterizing the structure and dynamics of pool fires [1]. The goal of this study is to improve the understanding of fire phenomena and support the development and validation of computational fluid dynamics (CFD) fire models such as the Fire Dynamics Simulator (FDS). This work also supports recent efforts by the International Association of Fire Safety Science (IAFSS) Working Group on Measurement and Computation of Fire Phenomena (the MaCFP Working Group), an international community of fire scientists sponsored by the International Association of Fire Safety Science. The MaCFP Working Group works to advance predictive fire models by addressing critical gaps in knowledge that hinder accurate modeling predictions by coordinating research among fire experimentalists and modelers [2-4]. Among the topics selected for investigation by the MaCFP are medium-scale pool fires such as those reported here.

Pool fires are a convenient testbed for model evaluation due to their well-defined boundary conditions, including an isothermal, flat, and horizontal fuel surface. The rate of evaporation in a liquid puddle or pool of burning liquid is controlled by heat transfer to the liquid pool, which is primarily due to gas-phase heat transfer processes involving convection and radiation. These heat transfer mechanisms are influenced by the fire size and its heat release rate. In this way, the heat and mass transfer in a pool fire are coupled, and the heat flux and corresponding mass burning rate ($\dot{m}$) of a pool fire depends on the total heat feedback to the pool surface ($\dot{Q}_s$). In a gaseous pool fire, the mass burning rate is independently controlled and the heat and mass transfer processes are decoupled.

Table 1 lists the eight pool fires considered here, including those burning gaseous methane and propane (at three distinct fuel flows/heat release rates), and those burning liquid methanol, ethanol, acetone, and heptane. The fuels were selected to complement previous studies that examined the structure of, and the heat and mass transfer processes in, these medium-scale pool fires [1, 5-11]. The fuels span a range of fuel-sooting tendencies from methanol which is non-sooting, to heptane which is moderately sooting. The measurements were conducted when the fires were steadily burning in a well-ventilated and quiescent environment. Supplementary measurements of soot mass fraction profiles are available in Refs. [1, 12, 13] and gas species volume fraction profiles for these fires are available in Refs. [1, 12, 13, 14].

Rigorous CFD fire model evaluation benefits from a large database of measurement results characterizing key features of the structure of a fire for a variety of fuel types and fire sizes. This report supports the construction of such a data repository. The measurements reported here include both global and local measurements as seen in Table 1. Some of the measurements reported are new, and some have been previously reported but are included here for

completeness. The global measurements include flame height, puffing frequency, mass burning rate, heat release rate, CO and soot yields, and radiative fraction. The local measurements include profiles of radiative and total heat flux onto the pool surface, radiative flux to an array of flux gauges forming a cylindrical control surface around the fire, the temperature at select locations inside the liquid pools, and the vertical and temperature centerline profiles above the fuel surface. The instrumentation used to conduct the measurements are also listed in Table 1. References for each of the measurements are provided in Table I2 in Appendix I.

There are few practical diagnostic options to quantify the velocity in a fire. Although many combustion studies and some fire studies have successfully employed various optical methods (alone or in combination with other measurements) to quantify the local velocity field [12-16]. The methods are expensive and not simple to implement, requiring particle seeding and sophisticated equipment. In addition, the method may be limited in the presence of soot. An effective and practical approach to velocity characterization in soot-laden fires is the use of a bidirectional probe in tandem with a fine-wire thermocouple [17, 18]. Such measurements are reported here for the profile of the upward speed as a function of distance above the pool centerline. The profile of the gas phase temperature as a function of distance above the pool centerline was measured using fine-wire, bare-bead, platinum thermocouples corrected for radiative loss and thermal inertia effects. Transient effects of the bidirectional probe were attempted but were unbelievably large and are not reported here.

In medium-scale pool fires, both radiative and convective heat transfer to the fuel surface are important [8, 11]. Here, new measurements of the total heat feedback to the surface of the gaseous pool fires are reported. Radiative heat transfer from a pool fire to its surroundings is also important as it can lead to fire spread to nearby items and, thereby, fire growth. In this study, estimates of the radiative fraction are reported based on single-location heat flux measurements and the assumption of isotropy.

This report is broken into several sections. Section 2 describes the experimental methods and apparatus, including the pool burners and instrumentation used to measure the gas phase and temperature, and the radiative heat flux emitted by the fire. Section 3 discusses the results and compares the measurements to previous studies and to theories and correlations in the technical literature. Section 4 summarizes the conclusions of the report. References are listed in Section 5. The Appendices represent nearly half of the report, presenting information characterizing fuel properties (Appendix A), pressure transducer and thermocouple instrumentation (Appendix B and C), the effect of the presence of the bidirectional probe on the thermocouple temperature measurements (Appendix D), a detailed analysis of measurement uncertainty (Appendix E and F), measurement results on the liquid fuel temperature and local heat flux (Appendix G and H), and a summary of references associated with Table 1 (Appendix I).

Table 1. List of measurements and instrumentation for the eight fires described in this report (indicated by an "X" in the table). References (when available) are provided for measurements not reported here.

Fuel			Methanol	Ethanol	Acetone	Heptane	Methane	Propane	Propane	Propane
		Case no.	1	2	3	4	5	6	7	8
		Nominal pool diameter (cm)	30	30	30	30	37	37	37	37
		Idealized heat release rate (kW)	18.4	27.8	42.0	106.6	34.5	20.7	34.4	50.1
	Measurement	Instrument								
Global	Mass burning rate	Load cell/flow meter	X	X	X	X	X	X	X	X
	Flame height	Video analysis	X	X	X	[8]	X	X	X	X
	Puffing frequency	Video & temp analysis	X	X	X	na [a]	X	X	X	X
	CO yield	NDIR [b]	X	X	X	X	X	X	X	X
	Soot yield	Laser transmission	X	X	X	X	X	X	X	X
	Radiative fraction	Heat flux gauge	X	X	X	X	X	X	X	X
	Total heat flux to pool surface	Thermocouples & integrated local flux profile	[11]	[11]	[11]	[8]	X	X	X	X
Local	Gas-phase temp profile	Fine Pt/Rh thermocouples	X	X	X	X	X	X	X	X
	Gas-phase velocity profile	Bi-directional probes	X	X	X	X	X	X	X	X
	Radiative flux to surroundings	Heat flux gauges	X, [11]	X	X	X	X	X	X	X
	Radiative flux onto fuel surface	Custom flux gauge	[11]	[11]	[11]	[8]	na	na	na	na
	Heat flux profile on fuel surface	Heat flux gauge	[11]	[11]	[11]	[8]	na	na	na	na
	Fuel surface temperature	Thermocouples	X	X	X	na	X	X	X	X
	In-depth liquid fuel temperature	Thermocouples	X	X	X	na	-	-	-	-

a. Parameters indicated by "na" are not available.

b. NDIR is an instrument that provides a non-dispersive infrared radiation measurement.

2. Experimental Methods

Experiments were conducted using water-cooled liquid and gaseous fuel burners. The pool fires were established under a canopy hood surrounded by a cubic enclosure, about 3 m on a side, made of a double-layer wire-mesh screen (6 mesh/cm with 83 % porosity) to reduce the impact of air currents and room ventilation. The effect of ambient convective currents on the fire was minimized by closing all inlet vents in the lab. The exhaust flow was maintained below about 1 kg/s, helping to avoid perturbations (such as flame lean) and minimizing the influence of the exhaust on fire behavior.

Steady-state burning conditions were established before measurements were initiated. A warm-up period of 5 min to 10 min was required for the mass burning rate to become steady. Since back diffusion of water and other gas-phase species can slowly accumulate in the fuel pool, fresh fuel was used for all the liquid fuel experiments [8, 19].* The liquid solvents methanol, acetone, ethanol, and heptane experiments were all conducted using high-purity (99.9 %) fuels. The gaseous fuels were of commercial purity or higher (99 %). The thermophysical properties of key materials are listed in *Appendix A*. Appendix F presents a complete uncertainty analysis for all measured parameters. Unless otherwise stated, the error bars presented in this report represent the expanded (k=2) combined uncertainty, corresponding to a 95 % confidence interval.

2.1. The 30 cm Liquid Burner

A circular stainless-steel pan with an inner diameter (D) of 0.301 m, a depth of 0.15 m, and a wall thickness of 0.0013 m held the liquid fuels. Figures. 1 - 2 show a schematic and an image of a liquid burner, illustrating its features and coordinate system. For convenience, all experimental data reported here use a cylindrical coordinate system with the fuel surface as the z-axis origin (see burner drawing in Fig. 2) and the pool center as the r-axis origin. A number of previous studies referred to in this report specified the top of the burner rim (instead of the fuel surface) as the z-axis origin, e.g., [8, 9, 20].

The bottom of the burner was maintained at a constant temperature by flowing tap water (nominally 20 °C) through a 3 cm section on the bottom of the fuel pan. The burner was mounted on legs such that the burner was about 0.3 m above the floor. A fuel overflow section attached to the burner was included for safety - it was positioned 10 cm below the burner rim and extended 2.5 cm in the radial direction beyond the fuel reservoir outer wall. The fuel inlet

* Water was observed in the residual fuel in the liquid pool after burning a heptane pool fire for an extended duration (order 1 hour) during experiments reported in Refs. [8, 19]

line was insulated and covered with a reflective foil to prevent the fuel from preheating. A baffle situated in the fuel pool just above the fuel entry port ensured that the upward momentum of fuel entering the liquid pool was eliminated, which reduced mixing in the fuel pool.

The liquid fuel temperature was measured using thermocouples positioned in the pool, as shown in Fig. 1. Fuel to the burner was gravity-fed from a reservoir on a mass load cell raised about 2 m above the floor. Using a calibrated load cell, the mass burning rate was measured by monitoring the mass flowing from the liquid fuel reservoir feeding the liquid pool.

During the majority of experiments reported here, the fuel level was maintained 1 cm below the burner rim by regulating the fuel supply from the reservoir to the burner. Some previous liquid fuel studies referred to in this report maintained a lip height of 0.5 cm [8, 9, 20]. This difference in lip height did not have a significant effect on the measured parameters. The liquid fuel level in the burner was verified throughout the experiment by visually observing a video feed of the tiny tip of a sharpened (1 mm diameter) pointer that formed a barely discernable dimple on the fuel surface. The fuel level indicator is seen towards the left of the burner in Fig. 1. A camera with optical zoom focused on the fuel level near the pointer, allowing observation of the fuel level. Manual adjustment of the fuel flow valve allowed maintenance of the liquid fuel level, which varied less than ± 2 mm during the experiment. An IR camera (Teledyne FLIR, Model: FLIR E30) with a spectral range from 7.5 µm to 13 µm was located 5 m away from the burner center to measure the burner side wall temperature. The thermal image was recorded with a 160 pixel x 120 pixel resolution at 1 Hz sampling rate. A part of the burner side wall was sprayed with black paint; the emissivity of the paint is 0.95. All measurements reported here are referenced to the center of the fuel surface, as seen in Fig. 2.

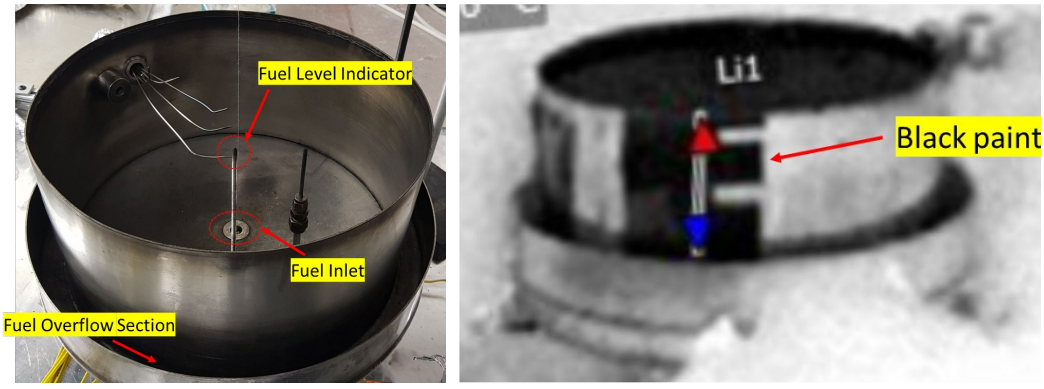

Fig. 1. The round, 30 cm diameter, water-cooled, steel burner with fuel level indicator and fuel overflow section (left) a photograph, (right) a thermal image.

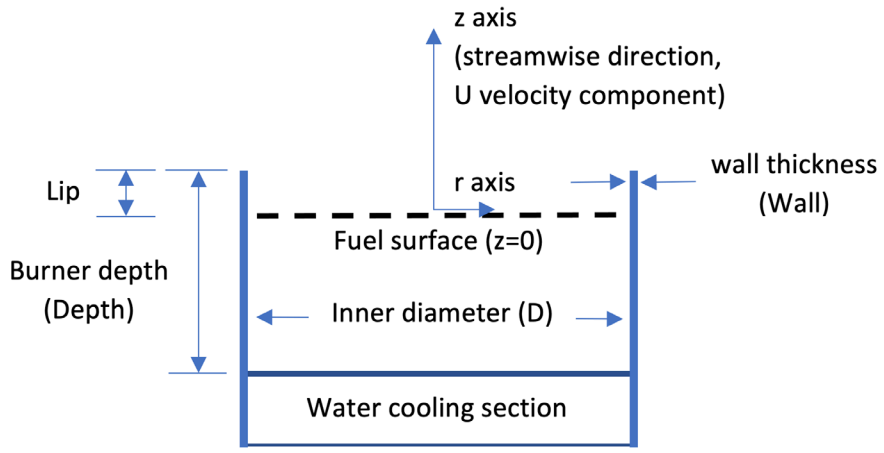

Fig. 2. Schematic of the liquid burner, illustrating its features and coordinate system.

2.2. The 37 cm Gas Burner

The steadily burning gaseous pool fires were established in a 37 cm diameter, porous bronze, circular burner (with zero lip height), as seen in Fig. 3. The depth of the porous metal section was approximately 10 cm. The burner had legs that established the burner about 0.8 m above the floor. Fuel to the gas burner was controlled via a mass flow controller located outside of the enclosure. The bottom and sides of the burner were cooled by circulating water to maintain a constant temperature during the experiments. The total heat feedback from the fire to the burner (or fuel surface) was determined by measurements of the cooling water flow and the temperature difference of the water at the burner's inlet and outlet.

The burner surface temperature was measured by spring-loading the thermocouple wire onto the burner's metal surface for the gaseous fuels. A small ceramic shield was placed over the thermocouple to prevent radiative gain at the thermocouple bead. During a methane fire experiment, an infrared camera was used to determine the uniformity of the surface temperature.

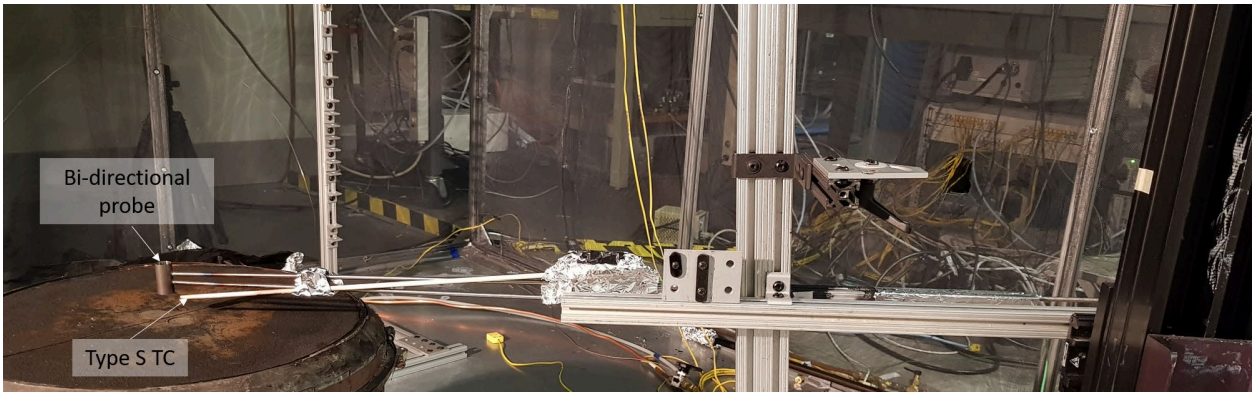

Fig. 3. The 37 cm diameter, water-cooled, porous bronze, gas burner in the fire compartment. The bidirectional probe and Type S thermocouple were attached to a horizontal rod mounted on the vertical moving traverse.

2.3. Flame Height Measurements

A 30 Hz video record of the fires was used to determine the flame height and the dominant puffing frequency. The video camera was located at $(x, y) = (216.5\ cm, 52\ cm)$ from the center of the burner surface. About 1800 frames, extracted every 2 frames in 2 min, in the video record were analyzed by Image-J software to determine the flame height. The video record of the flame appearance was converted to 8-bit images. The flame region could be distinguished from the background in these images, considering the threshold suggested by Otsu [21], and the images were transformed into binary images. The RGB and binary images of the flame in the same frame are shown in Fig. 4.

The instantaneous flame height was defined as the distance between the burner and the flame tip. The flame surface was estimated when the intermittency is 0.5 [22]. The flame height in each frame was corrected for image distortion error due to parallax. The detailed correction method is explained in *Appendix E*.

A fast Fourier transform was applied to the transient flame height to determine the dominant puffing frequency. In cases without video recordings, the puffing frequency of flames was calculated using temperature measurements with a fine thermocouple at a high sampling rate (500 Hz – 1000 Hz).

The experimental measurements were compared to the empirical model for the flame height suggested by Heskestad [22].

$$\frac{Z_f}{D} = 15.6N^{1/5} - 1.02 \qquad (1)$$

where N is the non-dimensional parameter defined by:

$$N = \left[\frac{c_p T_\infty}{g\rho_\infty^2 \left(\frac{H_c}{\gamma}\right)^3}\right]\frac{\dot{Q}^2}{D^5} \quad (2)$$

where c_p is the specific heat of air at constant pressure, H_c is the actual lower heat of combustion, and γ is the actual mass stoichiometric ratio of air to volatiles. ρ_∞ and T_∞ are the ambient density and temperature, respectively, g is the acceleration of gravity, $\dot{Q}$ is the total heat release rate (the product of the mass burning rate and the heat of combustion), and D is the diameter of the pool.

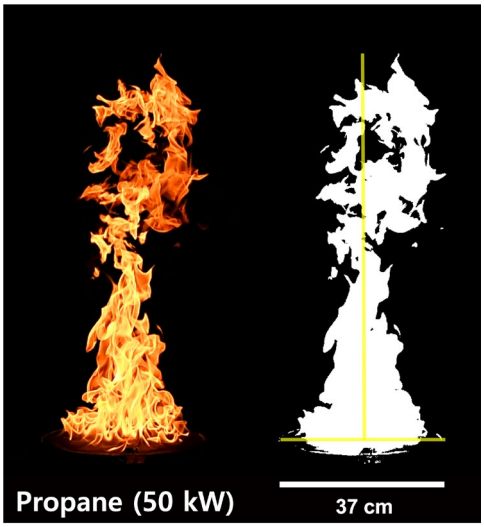

Fig. 4. The RGB and processed, a binary image of a fire taken from the video record of the 50 kW propane fire. The yellow vertical line represents the flame height.

2.4. CO and Soot Yields Measurements

The steady-state CO concentration was determined via extractive sampling and non-dispersive infrared (NDIR) measurements. The steady-state soot mass fraction was measured in the duct using laser transmission at 632 nm. The detailed experimental setup is explained in Ref. [23].

2.5. Thermocouple Temperature Measurements

The local temperature was measured using Type S (Pt with 10 % Rh/Pt) or Type R (Pt with 13 % Rh/Pt) bare-bead thermocouples with wire diameters varying from 13 µm to 50 µm. The selection of the diameter of a fine wire thermocouple must consider trade-offs between the durability of the instrument and measurement needs. The finer the wire, the smaller the radiative exchange with the environment and the faster the measurement time response, but

the more fragile the thermocouple. The thermocouple bead was approximately spherical, as determined using an optical microscope. Figure 5 shows images of the thermocouple bead. The thermocouple bead diameter (d_b) is estimated using an image processing software (Image-J). The bead diameters varied from about 52 µm to 199 µm. *Appendix C* presents thermocouple information and temperature measurement information in each experiment.

Table C1 lists thermocouple type and wire and bead diameters. Table C2 lists the information on temperature measurement positions and data acquisition sampling rate for the thermocouple employed in each experiment.

A computer-controlled translation device was used to adjust the position of the thermocouple along a vertical axis. The vertical translation device was mounted on a horizontal rail to adjust the position of the thermocouple in the radial direction. The thermocouple assembly, lead wires, and connections were insulated and covered with aluminum foil.

The measured signal was acquired at the sampling rate presented in Table C2 for 120 s at each position, representing about 280 flame puffing cycles. The temperature was typically measured three times at each location, sometimes more, and always at least two times at each location.

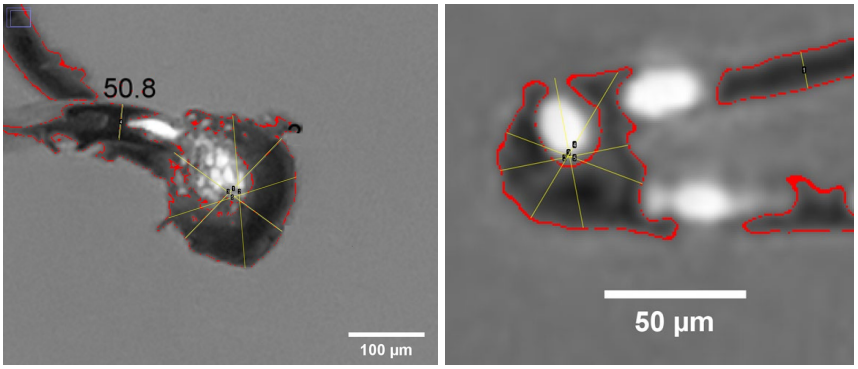

Fig. 5. Images of thermocouple bead; (a) TC 1: d_b = 199 µm and (b) TC 2: d_b = 52 µm.

2.5.1. Gas Temperature Determination: Energy Balance at the Thermocouple Bead

The energy balance on a thermocouple bead consists of convective, radiative, and conductive heat transfer. The details of the energy balance on the thermocouple bead and assumptions are explained in Ref. [24]. Following Ref. [24], the conductive heat transfer between the spherical bead and the lead wire is assumed to be negligible. Considering the energy balance at the thermocouple bead, the instantaneous gas temperature $T_g(t)$ is estimated as:

$$T_g(t) = T_b(t) + \tau \frac{dT_b(t)}{dt} + \frac{\epsilon\sigma}{h}(T_b^4(t) - T_{surr}^4) \quad (3)$$

where $T_b(t)$ is the instantaneous thermocouple bead temperature, h is the convective heat transfer coefficient of the gas flow near the bead, σ is the Stefan-Boltzmann constant ($5.67 \cdot 10^{-8}$ W/m^2/K^4), and ϵ is the thermocouple emissivity. The mean and expanded (k=2) combined uncertainty of ambient temperature during the experiment was 298 K ± 5 K, which is taken as the surrounding temperature, T_{surr}.[1] In Eq. 3, the second and third terms on the right side represent the thermal inertia and radiative loss corrections, respectively. Here, the flame is taken as optically thin based on estimates using the updated RADCAL software [25], which is a radiation subroutine in Ref. [2]. The thermocouple emissivity was taken as that of platinum based on inspection after each experiment. Assuming a spherical bead shape, the time constant (τ) is estimated as:

$$\tau = \frac{\rho_b c_{p,b} d_b^2}{6 \mathrm{Nu} \lambda_g} \tag{4}$$

where ρ_b and $c_{p,b}$ are the thermocouple's density and specific heat, respectively, assumed to be pure platinum. In Eqs. $4-5$, the convective heat transfer coefficient is defined as $h = \mathrm{Nu} \cdot \lambda_g / d_b$, where λ_g is the thermal conductivity of the gas and d_b is the thermocouple bead diameter. The Nusselt number (Nu) is empirically associated with the Reynolds and Prandtl numbers. The Ranz-Marshall model [26] applies the following Nusselt number correlation for convective heat transfer:

$$\mathrm{Nu} = 2.0 + 0.6\, \mathrm{Re}_d^{1/2}\, \mathrm{Pr}^{1/3}; \qquad 0 < \mathrm{Re}_d < 200 \tag{5}$$

The temperature-dependent gas properties are taken as those of air [27]. The temperature-dependent emissivity and thermophysical properties of platinum are taken from Refs. [28, 29] and are listed in *Appendix A*.

2.6. Bidirectional Probe Velocity Measurements

A bidirectional probe was located above the burner centerline. The external and internal diameters of the probe were 15.9 mm and 13.6 mm, respectively. The pressure difference between the front and rear of the probe was measured with multiple pressure transducers, each with a different instrument response time. As many as three transducers were used for any single time series measurement. A Type S, bare-bead thermocouple was positioned 5 mm upstream of the probe, as seen in Fig. 6. This position was based on being as close to the probe

[1] Unless otherwise stated, the error bars presented in this report represent the expanded (k=2) combined uncertainty, corresponding to a 95 % confidence interval.

as practical while preventing damage to the fine thermocouple by the fire, which tended to move the thermocouple downstream towards the bidirectional probe when instruments were inserted into the upward-moving fire plume. The percentage temperature difference between the mean gas temperature measurements with and without the bidirectional probe in the fire is 4 % on average, which is less than the mean of the expanded (k=2) combined uncertainty of the mean gas temperature measured using thermocouples without a nearby bidirectional probe (see *Appendix D*). Thus, the presence of the probe is regarded as having a negligible impact on the thermocouple measurement.

Voltage signals from the pressure transducers and the thermocouples were obtained using a DAQ (Model: SCXI-1600, National Instrument Inc). Detailed information about the pressure transducers' calibration factors and response time are provided in *Appendix B*. The voltage and temperature data sampling rates ranged from 20 Hz to 1000 Hz. Data was acquired for 2 min at each position along the axial centerline above the burner.

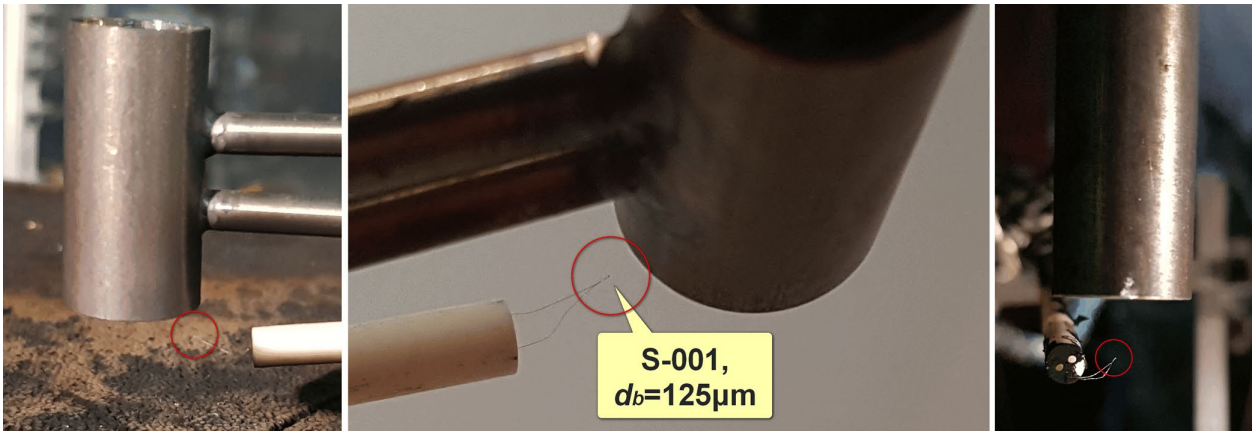

Fig. 6. Photograph of a bidirectional probe with a 25 µm diameter wire, bare-bead, Type S, thermocouple a few cm above the gas burner.

2.6.1. Gas Velocity Determination

The instantaneous gas velocity in the upward direction ($V_g(t)$) is estimated from the measurement of the pressure difference across the bidirectional probe and the simultaneously measured gas temperature near the upstream face of the probe, applying the velocity model for a bidirectional probe [17] as:

$$V_g(t) = \frac{1}{k_p(t)}\sqrt{\frac{2\Delta P_c(t)}{\rho(t)}} \tag{6}$$

where $k_p(t)$ is the instantaneous probe constant, and $\Delta P_c(t)$ and $\rho(t)$ are the instantaneous corrected pressure difference and gas density, respectively. The gas density $\rho(t)$ is determined from thermocouple temperature measurements using a fine, bare-bead, Type S thermocouple corrected for radiative loss and the assumption[2] that the gas constant corresponds to that of air.

The instantaneous measured pressure difference $(\Delta P(t))$ is corrected to consider the pressure transducer time response, which is treated like the inertia correction in the thermocouple measurement (see Eq. 3). The instantaneous corrected pressure difference $(\Delta P_c(t))$ is defined as:

$$\Delta P_c(t) = \Delta P(t) + \tau_p \frac{d\big(\Delta P(t)\big)}{dt} \tag{7}$$

where the second term on the right side of the equation is the instantaneous time-response correction term. Solving for the correction term, the time derivative of the pressure difference is calculated using a second-order polynomial fit using three consecutive data points in the pressure difference time series. The parameter, τ_p, is the pressure transducer response time, which is experimentally determined by applying a step function of pressure difference, as discussed in *Appendix B*.

The value of the dimensionless parameter, $k_p(t)$ in Eq. 6, depends on several factors, including the Reynolds number, probe shape, and flow approach angle. Reference [17] provides a polynomial curve fit for low Reynolds number flows ($40 < \mathrm{Re}_p < 3800$) with a combined expanded relative uncertainty of 5 %, which is given as:

$$\begin{aligned} k_p(t) = \quad & 1.53 - 1.37 \cdot 10^{-3}\mathrm{Re}_p(t) + 1.69 \cdot 10^{-6}\mathrm{Re}_p^2(t) + 9.71 \cdot 10^{-10}\mathrm{Re}_p^3(t) \\ & +2.56 \cdot 10^{-13}\mathrm{Re}_p^4(t) - 2.48 \cdot 10^{-17}\mathrm{Re}_p^5(t) \end{aligned} \tag{8}$$

where $\mathrm{Re}_p(t)$ is defined as $(V_g\ (t)d_p)/\nu(t)$, and the parameters d_p and $\nu(t)$ are the bidirectional probe diameter and the instantaneous kinematic viscosity of the gas (taken here as air), respectively. In this study, the mean Reynolds number $\left(\overline{\mathrm{Re}_p}\right)$ varied from about 100 to 1500, depending on the distance from the burner surface. The temperature-dependent gas

[2] This assumption is better away from the burner. An estimate of the efficacy of the assumption can be determined considering the square root of the ratio of the mean molecular weight of gas species to that of air as a function of position (see Eq. 4), which can be estimated from the mean species concentrations and temperatures along the fuel centerline reported in Ref. [1]. For example, in the 30 cm methanol pool fire, the assumption is good to better than ± 5 % of the mean velocity result near the fuel surface. For locations larger than one-half pool diameter above the fire, the assumption is good to better than ± 2 % of the mean velocity result.

properties in Eqs. 3 – 8 are taken as those of air [27], calculated using the polynomial fits presented in *Appendix A*. The instantaneous thermocouple temperature corrected for radiative loss was determined following the procedure outlined in *Section 2.5.1* with the results presented in *Section 3.5*.

In this study, the time series datasets of the bidirectional probe pressure difference were acquired at each measurement location using multiple pressure transducers, with the measurements typically repeated 2 to 3 times and as often as 10 times. The temperature and velocity measurement results are discussed in *Section 3* below, with the details of the uncertainty analysis presented in *Appendix F*.

2.7. Heat Flux Measurements to the Surroundings and Radiative Fraction

The radiative heat flux emitted to the surroundings was measured using a wide-view angle (150°), water-cooled, Gardon-type, total heat flux gauges with 1.3 cm diameter faces. Multiple gauges were used to measure the heat flux distribution of the pool fire, as shown in Fig. 7. The gauge locations were selected considering the laboratory confines and the fire size. Radial heat flux gauges were aligned along the plane of the burner rim to measure the heat flux in the downward direction. Vertical heat flux gauges were aligned to measure the heat flux distribution in the radial direction away from the fire.

A heat flux gauge was located at $r/D > 5$ to estimate the radiative fraction using a single-location measurement (see *Section* 2.8). The gauges were calibrated using a secondary standard in NIST's heat flux radiometer calibration facility. Voltage signals from the gauges were acquired at 1 Hz and time-averaged. The measured heat flux was corrected considering the background heat flux from the surroundings, as described in detail in Ref. [24].

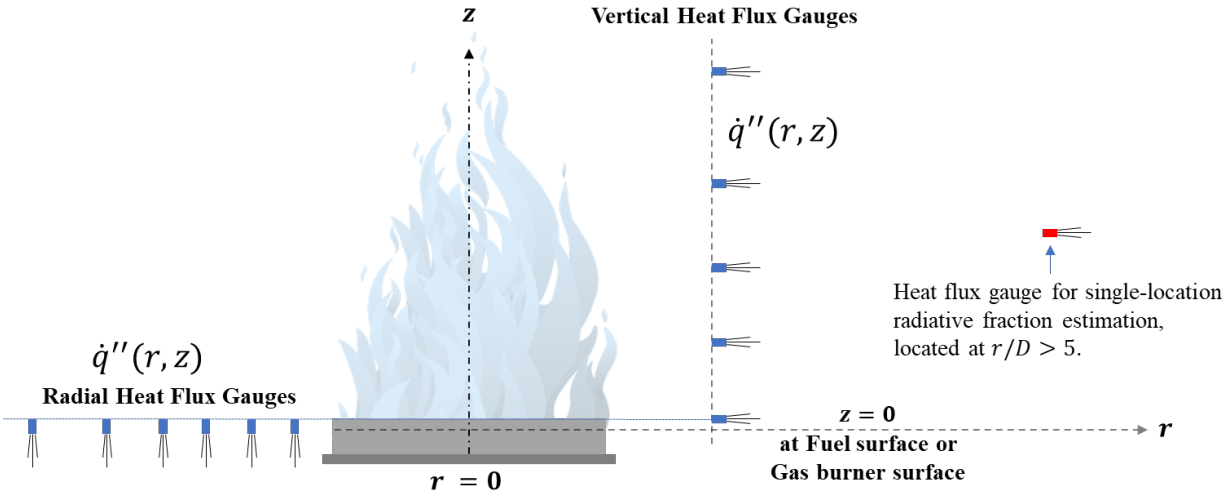

Fig. 7. A schematic diagram of the heat flux gauge set-up.

2.8. Single Location Heat Flux Measurement and Estimate of Radiative Fraction

The radiative fraction of the steadily burning pool fires is estimated from a single location measurement of the heat flux. The measurements are compared to previous ones based on single and multiple heat flux gauges. Figure 8 shows a schematic drawing of the single-point heat flux gauge measurement used to estimate the radiative fraction. A gauge was located at a distance (r) from the pool center and at a vertical position (z) above the fuel surface.

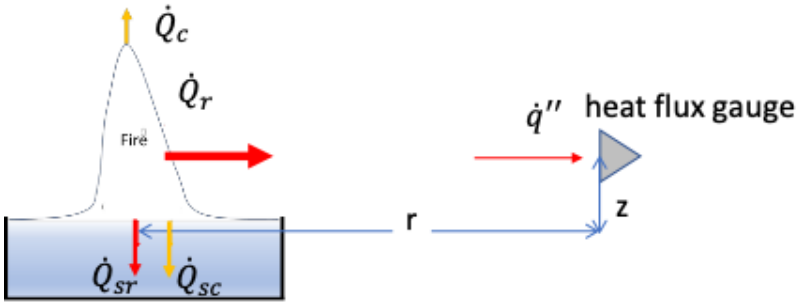

Fig. 8. Schematic drawing of the determination of the radiative fraction using a single-point heat flux measurement in a steadily burning fire, where *z* represents the distance above the fuel surface.

In the figure, the convective energy transferred to the fuel surface per unit time is $\dot{Q}_{sc}$. The total energy radiated by the fire to the surroundings per unit time is denoted as $\dot{Q}_r$, whereas the energy radiated back to the fuel surface per unit time is denoted as $\dot{Q}_{sr}$. The energy per unit time radiated by the fire $(\dot{Q}_{rad})$ is the sum of the energy radiated per unit time to the surroundings and to the fuel surface:

$$\dot{Q}_{rad} = \dot{Q}_r + \dot{Q}_{sr} \tag{9}$$

For suitably far distances from the fire, the radiative fraction, χ_{rad}, can be determined from a single measurement of the radiative heat flux as:

$$\chi_{rad} = \frac{\dot{Q}_{rad}}{\dot{m}H_c} = \frac{4\pi r^2 \dot{q}''}{\dot{m}H_c} \tag{10}$$

where $(\dot{q}'')$ is the radiative heat flux measured at a distance r from the fire, $\dot{m}$ is the fuel mass burning rate, and H_c is the fuel's net heat of combustion (assuming water as a gaseous product). Here, fire symmetry and radiative isotropy are assumed. The product, $\dot{m}H_c$, is the ideal heat release rate of the fire. According to Modak [30], a single location estimate of the radiative fraction is accurate to 95% for distances (*r*) greater than 5 times the pool's diameter from the fire.

2.9. Heat Feedback

New results as well as results from previous investigations measuring the heat feedback to the surface of the liquid pool and the gaseous burner are highlighted in this section.

2.9.1. Profiles of Local Heat Feedback

The profiles of the total heat flux onto the surface of the liquid fuel fires were measured using a total heat flux gauge [8].

For the liquid fuel fires, previous studies reported on the time-averaged local heat flux in the downward direction onto the fuel surface was measured with a water-cooled, Gardon-type, heat flux gauge positioned just above the fuel surface as a function of distance from the pool center [8]. The gauge was a custom-designed 1.25 cm diameter (1.0 cm depth) circular gauge with the sensing portion of the gauge positioned 3 mm ± 1 mm above the burner rim facing upward towards the fire. The gauge was translated across the surface of the pool such that the total heat flux was determined as a function of distance from the pool center. The signal output and the water cooling in/out lines (3 mm outer diameter) were embedded within a straight 9 mm diameter metal tube connected to the side of the gauge. The detailed experimental setup is described in Ref. [11].

In addition, profiles of the local radiative heat flux to the fuel surface were measured as a function of radial location in the 30 cm methanol and heptane pool fires. The measurements were conducted using a narrow view-angle, nitrogen-purged radiometer. The total heat feedback onto the fuel surface was calculated by integrating the measured local heat flux measurements, assuming axisymmetric [8].

2.9.2. Total Heat Feedback

For the liquid fuel fires, the total heat feedback per unit time to the fuel surface was determined by integrating the profiles of the local heat feedback measurements (see *Section 2.9.1* above) across the pool surface [8].

For the fires burning gaseous fuels, the total heat feedback per time to the burner surface was determined using the burner as a calorimeter. The measured steady-state average temperature difference (ΔT_w) between the water inlet and outlet and the volumetric rate of water flow ($\dot{V}_w$) was used to determine the total heat feedback per unit time to the burner ($\dot{Q}_b$) [31]:

$$\dot{Q}_b = \dot{V}_w C_{p,w} \Delta T_w \tag{11}$$

where $C_{p,w}$ is the volumetric heat capacity of the burner cooling water (4.18 J/ml/K at 20 ºC, 101 kPa). For a fire in steady-state, the fractional total heat feedback onto the burner (χ_b) is

defined as $\dot{Q}_b/\dot{Q}$. The cooling water volumetric flow rate was measured using a stopwatch and a graduated cylinder with a resolution of 1 ml. The steady-state averaged temperature of the inlet and outlet of the cooling water was measured using a Type K thermocouple with a sampling rate of 1 Hz.

The convective component of the total heat feedback to the fuel, or burner surface, was estimated using thin film theory as outlined for the gaseous fuels in Ref. [31], enabling calculation of the radiative component of the total heat feedback denoted as (χ_{br}). Values of χ_{br} for the liquid fuels were reported in [11].

3. Results and Discussion

Figures 9 - 10 show images of the fires as they undergo one puffing cycle. The methanol fire is purely blue, whereas the heptane fires is highly luminous, yellow, and opaque. The ethanol and the 20 kW propane fires are observed to include some number of bluish flames very close to the base of the fire, which is difficult to capture in a photo image, but is visibly observable. The other fires appear more luminous than ethanol, but less so than heptane. Observations of the surface of the liquid fuels confirm the existence of waves. The waves were difficult to photograph but with appropriate lighting, their presence was recognizable. Figure 11 shows standing waves on the surface of the methanol fire. The image was taken through the wire mesh screens surrounding the fire. The amplitude of the waves was about 1 mm, and its frequency was approximately 2.4 Hz ± 0.6, which was synchronous with the gas-phase fire puffing frequency. This should not be surprising - as the free pool surface boundary responds to pressure fluctuations generated from the fire itself. The waves were most visible in the methanol fire, probably due to its coherence and the extreme necking-in of the methanol fire as compared to the other fires (see Fig. 9). Waves on the surface of the other fuels had different modes and smaller amplitudes but were clearly visible as seen in the image of the ethanol fire in Fig. 11.

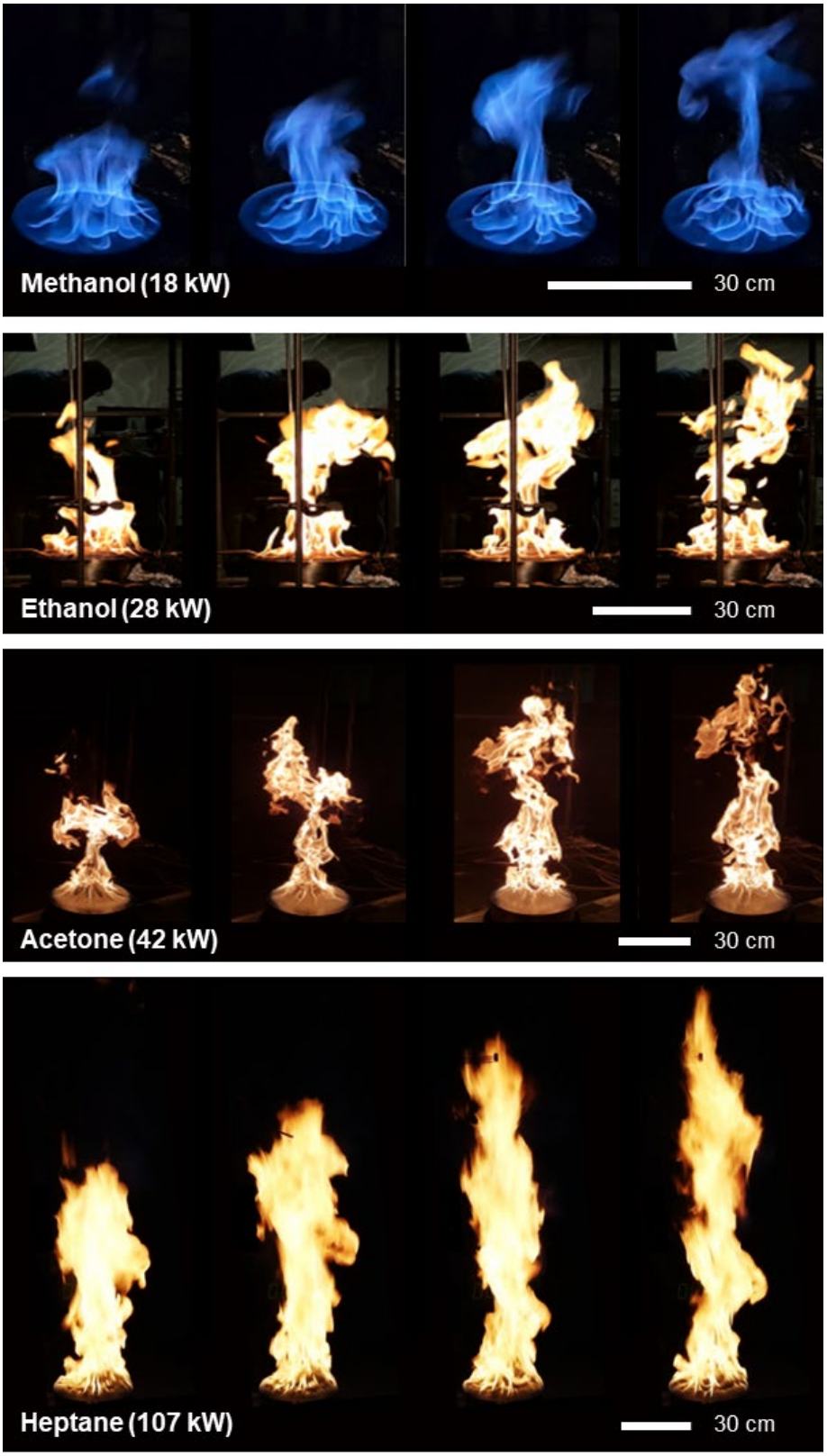

Fig. 9. Sequential images of flame in the methanol, ethanol, acetone, and heptane fires during one puffing cycle.

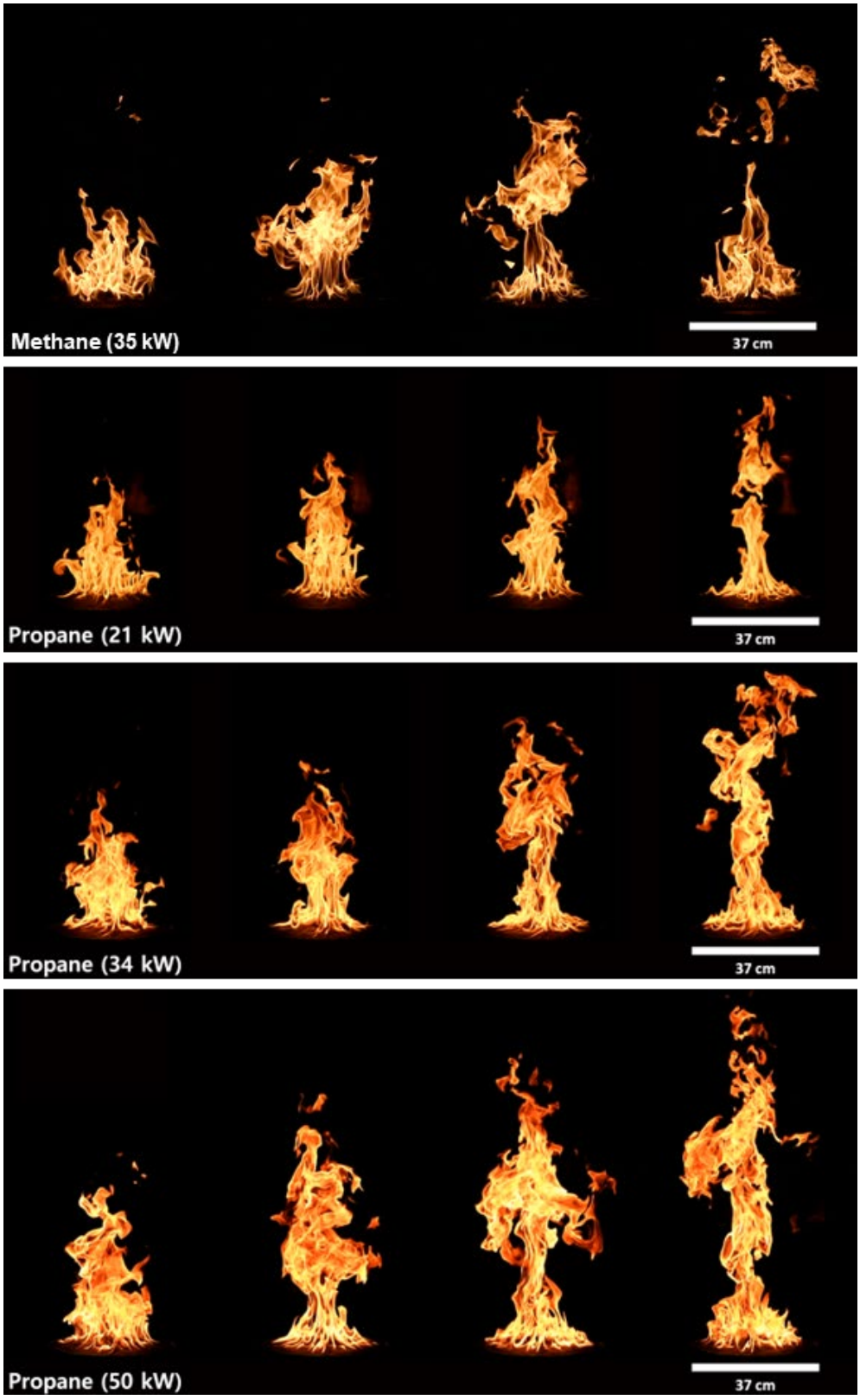

Fig. 10. Sequential images of flame in the methane and the 20 kW, 34 kW and 50 kW propane fires during one puffing cycle.

Fig. 11. Waves on the surface of the burning methanol (left) and ethanol (right) pool fires. The gas phase methanol flames, which are present, are difficult to see in this image.

3.1. Ideal Heat Release Rate

The ideal heat release rate $(\dot{Q})$, i.e., $\dot{m}\Delta H_c$ was estimated from the mass burning rate $(\dot{m})$, where ΔH_c is the net heat of combustion listed in Table A1. The fuel pool diameter, the measured mass burning flux, and the ideal heat release rate are presented in Table 2.

Table 2. List of the lower (or net) heat of combustion (ΔH_c), the pool diameter (D), the measured mass flux $(\dot{m}'')$, and the ideal heat release rate $(\dot{Q} = 0.25\pi D^2 \dot{m}'' \Delta H_c)$ averaged over the n repeat experiments.

	Case no.	Fuel	ΔH_c [kJ/kg][a]	D [m]	$\dot{m}''$ [g/m^2-s]	$\dot{Q}$ [kW]	n
Liquid Fuels	1	Methanol	19.9	0.301 ± 0.002 [b]	13.0 ± 0.4	18.4 ± 0.5	14
	2	Ethanol	26.8	0.301 ± 0.002 [b]	14.6 ± 0.2	27.8 ± 0.4	4
	3	Acetone	28.5	0.301 ± 0.002 [b]	20.7 ± 3.1	42.0 ± 6.4	7
	4	Heptane	44.6	0.301 ± 0.002 [b]	33.6 ± 3.3	106.6 ± 10.4	2
Gaseous Fuels	5	Methane	50.0	0.37 ± 0.005	6.4 ± 0.1	34.5 ± 0.5	c
	6	Propane	46.3	0.37 ± 0.005	4.2 ± 0.2	20.7 ± 0.9	c
	7	Propane	46.3	0.37 ± 0.005	6.9 ± 0.2	34.4 ± 1.2	c
	8	Propane	46.3	0.37 ± 0.005	10.0 ± 0.3	50.1 ± 1.7	c

a) from Ref. [32]. The uncertainty is listed in Table A1.
b) The inner pool diameter is specified (see Fig. 2).
c) The gaseous fuel flows were set but not measured.

3.2. Flame Height and Puffing Frequency

Table 3 shows the mean and standard deviation of the flame height normalized by the burner diameter (Z_f/D) in the methanol, ethanol, acetone, heptane, methane, and propane gas fires,

using Heskestad's model [22] and image processing of the video records. Calculating the fast Fourier power spectrum of the time-varying flame height, the relationship between frequency and amplitude is shown in Fig. 12. The dominant frequency of the 34 kW methane gas fire is 2.48 Hz. The first harmonic of the dominant frequency is also evident, exemplifying this pulsing fire's repetitive and coherent nature. Flame puffing frequency in the liquid and gaseous fuel fires is listed in Table 3. As expected, the puffing frequency in the 37 cm diameter fires is generally smaller than the fire burning in the 30 cm diameter fires [33]. Zukoski [34] showed that the mean puffing frequency (f) is inversely proportional to the square root of the burner diameter (D), defiend as: $f = (0.5 \pm 0.04)\sqrt{g/D}$[3]; where g is the gravitational acceleration. The mean puffing frequencies estimated by the correlation are 2.9 Hz ± 0.4 Hz and 2.6 Hz ± 0.4 Hz for the 30 cm and 37 cm burners, respectively. The results are in agreement with the measured puffing frequency listed in Table 3 within the expanded (k=2) measurement uncertainty.

Table 3. The mean and RMS of the flame height (Z_f/D) normalized by the burner diameter in the methanol, ethanol, acetone, heptane, methane, and propane gas fires, using image processing of the video record as compared to Heskestad's model [22]. The flame puffing frequency and its standard deviation are also listed.

Case No.	Fuel	$\dot{Q}$ [kW]	D [cm]	Normalized Flame Height, $\frac{Z_f}{D}$		Puffing Frequency [b] [Hz]
				Heskestad model [22]	Image processing [a]	
1	Methanol	18.4	30.1	1.4	1.2 ± 0.5	2.49 ± 0.01 [c]
2	Ethanol	27.8	30.1	1.9	2.0 ± 0.9	2.41 ± 0.09 [c]
3	Acetone	42.0	30.1	2.3	2.8 ± 0.6	2.45 ± 0.12 [c]
4	Heptane	106.6	30.1	4.3	4.4 ± 0.7 [d]	na
5	Methane	34.5	37	1.6	1.9 ± 0.5	2.48 [e]
6	Propane	20.7	37	1.1	1.4 ± 0.4	2.22 ± 0.02 [e]
7	Propane	34.4	37	1.6	2.0 ± 0.4	2.39 ± 0.02 [e]
8	Propane	50.1	37	2.1	2.6 ± 0.5	2.39 [e]

a) the uncertainty represents the root mean square (RMS) of the measured flame height.
b) the uncertainty represents the standard deviation of the mean puffing frequency determined from repeat measurements.
c) calculated using temperature measurements with a fine thermocouple at a high sample rate (500 Hz ~ 1000 Hz).
d) the mean flame height is consistent with the result reported in Ref. [8].
e) calculated using video recordings at frame rates of 15 and 30 Hz.

[3] where the uncertainty in the correlation is one standard deviation

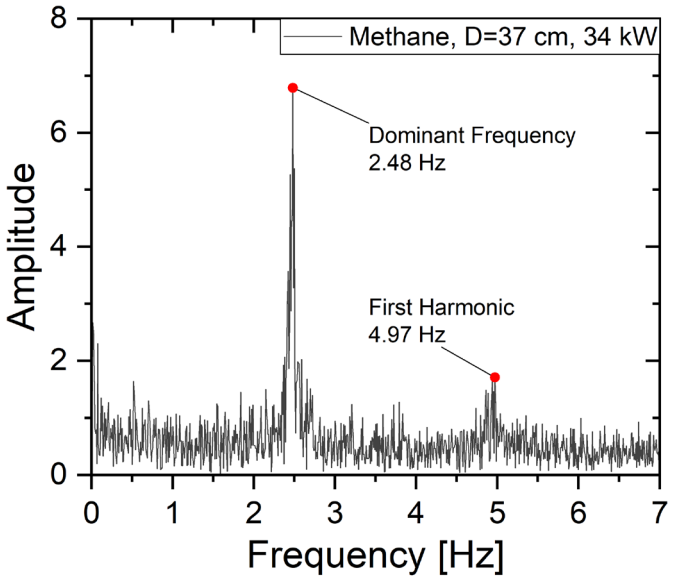

Fig. 12. Fast Fourier power spectrum of the time-varying flame height in the 34 kW methane gas pool fire.

3.3. CO and Soot Yields

CO and Soot Yields in the liquid and gaseous pool fires are listed in Table 4. The carbon monoxide (CO) yield was determined via extractive sampling from the exhaust duct during steady burning. Gases were extracted from the duct with soot and water filtered from the sample. Carbon monoxide was measured using a non-dispersive infrared sensor. The mass flow of CO was calculated with the duct mass flow, which was measured using thermocouples and bidirectional velocity probes as described in Ref. [35]. Soot concentration measurements were obtained in the duct using a smoke concentration meter based on light extinction with a helium-neon laser [36]. The mass-specific extinction coefficients were taken as 8.7 m^2/g [37]. The soot yield was determined by considering the ratio of the soot mass flow to the fuel mass burning rate following Ref. [35].

Table 4. The measured CO and soot yields in the liquid and gaseous pool fires. The uncertainty represents the standard deviation of the mean from n repeat measurements.

Case no.	Fuel	$\dot{Q}$ [kw]	CO Yield [10^{-3} g/g]	Soot Yield [10^{-3} g/g]	n (Repeats)
1	Methanol	18.4	a	0 [b]	6
2	Ethanol	27.8	0.3 ± 0.1	a	3
3	Acetone	42.0	1.0 ± 0.2	0.9 ± 0.3	3
4	Heptane	106.6	10.1 ± 1.3	16.9 ± 0.5	3
5	Methane	34.5	1.2 ± 0.1	a	8
6	Propane	20.7	4.0 ± 0.4	1.9 ± 0.5	4
7	Propane	34.4	3.6 ± 0.4	4.6 ± 0.4	4
8	Propane	50.1	a	0 [b]	7

a. below detection limits (< 1E-4).
b. soot was not observed at any fire location.

3.4. Gas-Phase Temperature Distribution

The gas temperature profiles measured using the various thermocouple types and data acquisition sampling rate (listed in Table C2) are plotted and compared with previous studies. The pooled (or ensemble) mean gas temperature at a particular measurement position ($\overline{T}_g$) was estimated by averaging the mean gas temperatures from all thermocouple data. Estimation of the pooled mean and RMS of the gas temperature and uncertainty analysis method are discussed in *Appendix F.2.*

3.4.1. Methanol Fire

Figure 13 shows the mean gas temperature along the fire centerline as a function of axial distance above the surface of the 30 cm methanol pool fire. Here, as everywhere else in this report unless otherwise stated, the error bars indicate the expanded (k=2) combined uncertainty, representing a 95 % confidence interval. The maximum mean temperature was about 1315 K, approximately 0.1 m above the fuel surface. The temperature gradient near the fuel surface is steep. At 1 cm above the fuel surface, the gas temperature was about 922 K ± 293 K. The temperature at two locations on the fuel surface was approximately the boiling point of methanol-338 K (see discussion in *Section 3.9*), yielding a gas-phase temperature gradient near the fuel surface of about 580 K/cm ± 290 K/cm.

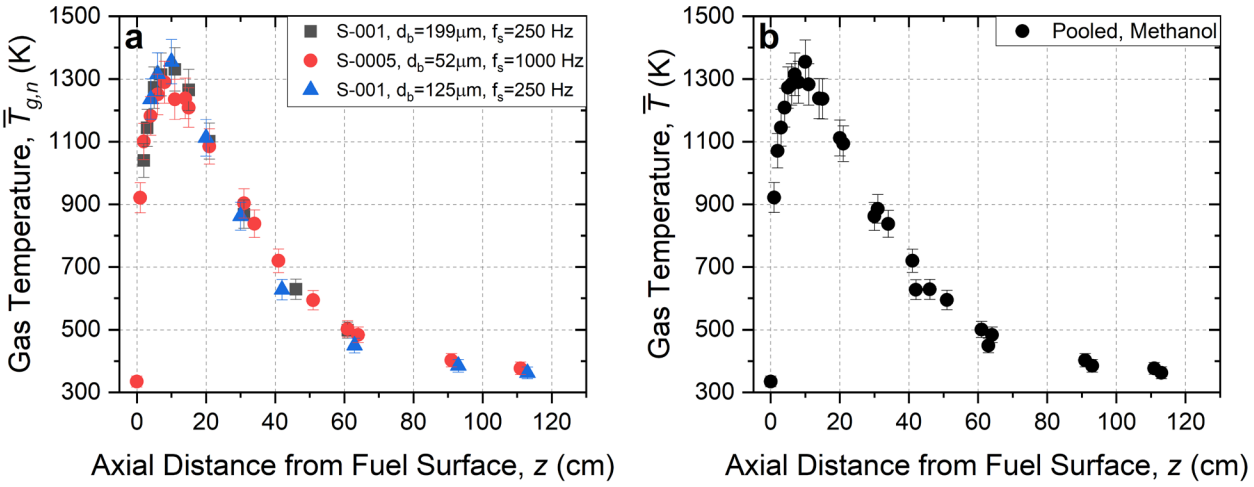

Fig. 13. The mean gas temperature along the fire centerline as a function of axial distance above the surface of the 30 cm methanol pool fire for: (a) different combinations of thermocouple type and sampling frequencies and (b) the pooled mean gas temperature.

Figure 14 shows the pooled mean gas temperature as a function of radial distance from the pool center at z = 41 cm, 51 cm, and 61 cm in the 30 cm methanol pool fire. Measurements on either side of the centerline demonstrate that the fire is axisymmetric on-average. The peak temperature values occur on the centerline (*r=0*) and begin to approach ambient temperatures at one burner radii off the centerline.

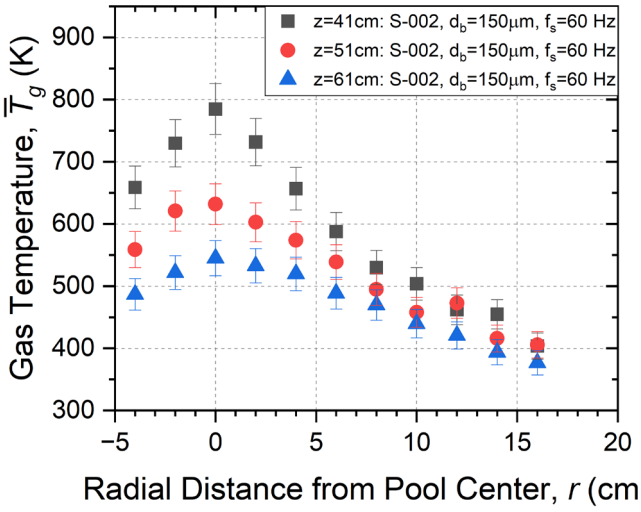

Fig. 14. The pooled mean gas temperature as a function of the radial distance from the pool center at z = 41 cm, 51 cm, and 61 cm above the fuel surface in the 30 cm methanol pool fire.

Figure 15 shows the pooled mean and the e of the temperature centerline profile as a function of the scaled axial distance above the burner. Here, a Froude number scaling collapses the results. The measurements are consistent with previous measurements in 30 cm diameter methanol pool fires [7, 20, 38] and a 1 m diameter methanol pool fire [38]. Weckman and Strong [7] measured the temperature in a 30.2 cm (inner) diameter methanol pool fire with a lip height of 1 cm using a 50 µm wire diameter, bare-bead, Type S (Pt, 10 % Rh/Pt), thermocouple similar to the thermocouples used in this study. Hamins and Lock [20, 39] conducted temperature measurements using a 75 µm wire diameter, bare-bead, Type S thermocouple in the steadily burning, 30.1 cm diameter methanol pool fire with a 0.5 cm lip. Sung et al. [38] measured temperature in a 100.6 cm diameter methanol pool fire with a lip height of 1 cm using a 50 µm diameter, bare-bead, Type S thermocouple and calculated the corrected gas temperature, considering the radiative loss and thermal inertia effects. A comparison of the results in Figure 15 shows that the temperature profiles as a function of axial distance above the burner normalized by $\dot{Q}^{2/5}$ are similar. The scatter in the results provides a gauge of the repeatability of the measurement.

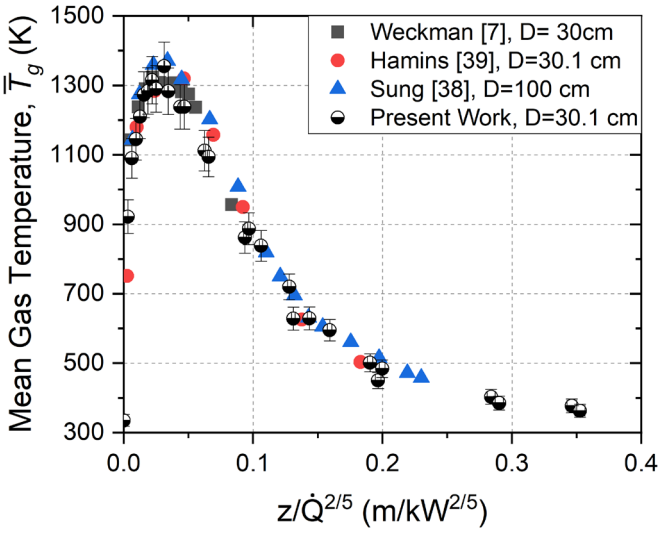

Fig. 15. The mean gas temperature along the fire centerline as a function of axial distance normalized by $\dot{Q}^{2/5}$ in the 30 cm methanol pool fire. normalized by $\dot{Q}^{2/5}$ The results from Refs. [7, 38, 39] are also shown.

3.4.2. Ethanol Fire

Figure 16 shows the mean gas temperature measured using various thermocouples and the pooled mean gas temperature as a function of axial distance above the centerline of the 30 cm ethanol pool fire surface. The error bars indicate the expanded (k=2) combined uncertainty, representing a 95 % confidence interval.

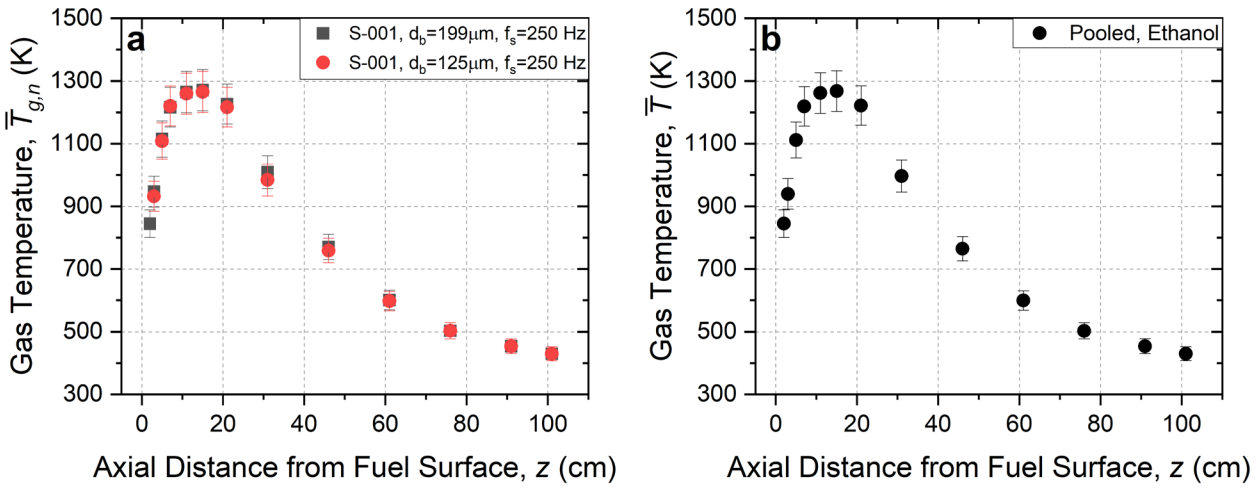

Fig. 16. The mean gas temperature along the fire centerline as a function of axial distance above the fuel surface in the 30 cm ethanol pool fire: (a) mean gas temperatures measured using the *n*th thermocouple ($\overline{T}_{g,n}$), (b) the pooled mean gas temperatures ($\overline{T}_g$).

Figure 17 shows the mean gas temperature as a function of axial distance above the fuel surface normalized by $\dot{Q}^{2/5}$. The results are similar to those of Fischer et al. [40], who made measurements in a 50 cm diameter ethanol pool fire with a lip height of 1 cm. The ideal heat release rate calculated from the measured mass burning flux (13.8 g/m^{2}s ± 0.5 g/m^{2}s) was 72.8 kW. Temperature was measured using a 75 µm wire diameter, bare-bead, Type K thermocouple with a bead diameter of 100 µm. The thermocouple temperature was corrected considering radiative loss and thermal inertia effects [40]. A comparison of the results shows the temperature profiles agree with the axial distance normalized by $\dot{Q}^{2/5}$. The horizontal uncertainty error for data with large values of $z/\dot{Q}^{2/5}$ in the figure increases due to the increasing absolute value of the uncertainty in $\dot{Q}$.

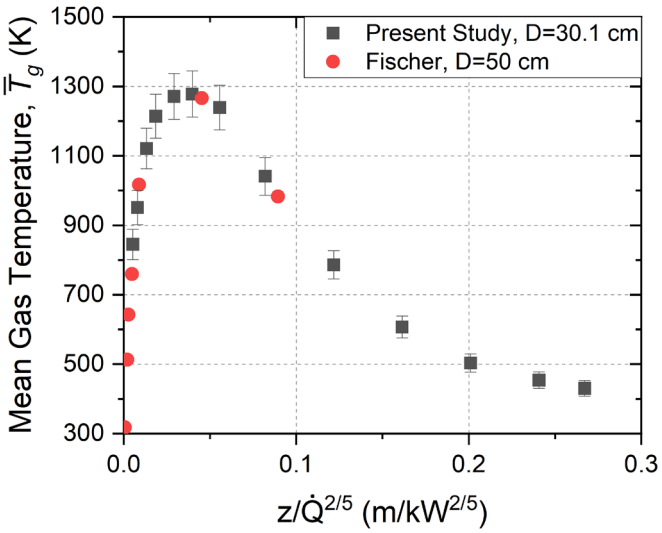

Fig. 17. The mean gas temperature along the fire centerline as a function of axial distance above the fuel surface normalized by $\dot{Q}^{2/5}$ in the 30 cm ethanol pool fire. The measurements from Ref. [40] are also shown.

3.4.3. Acetone Fire

Figure 18 shows the mean gas temperature measured using various thermocouples and the pooled mean gas temperature as a function of axial distance above the fuel surface in the 30 cm acetone pool fire. The error bars indicate the expanded (k=2) combined uncertainty, representing a 95 % confidence interval.

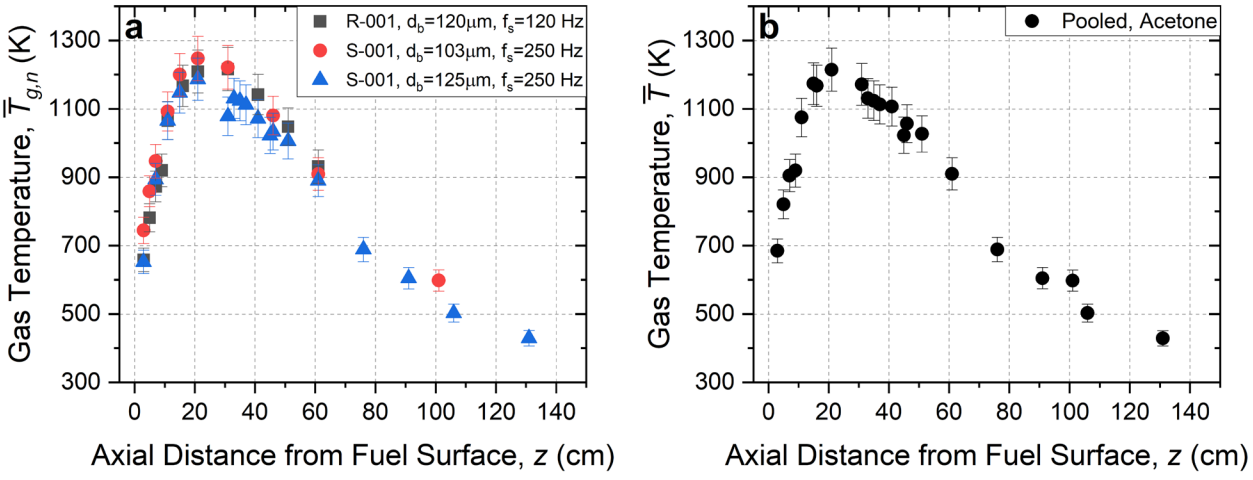

Fig. 18. The mean gas temperature along the fire centerline as a function of axial distance above the fuel surface in the 30 cm acetone pool fire: (a) mean gas temperature measured using the *nth* thermocouple ($\overline{T}_{g,n}$), (b) the pooled mean gas temperature ($\overline{T}_g$).

Figure 19 shows the mean gas temperature as a function of axial distance above the fuel surface normalized by $\dot{Q}^{2/5}$. Previous measurements in a 30 cm acetone pool fire from Ref. [41] are also shown. A comparison of the results shows that the temperature profiles are in general agreement.

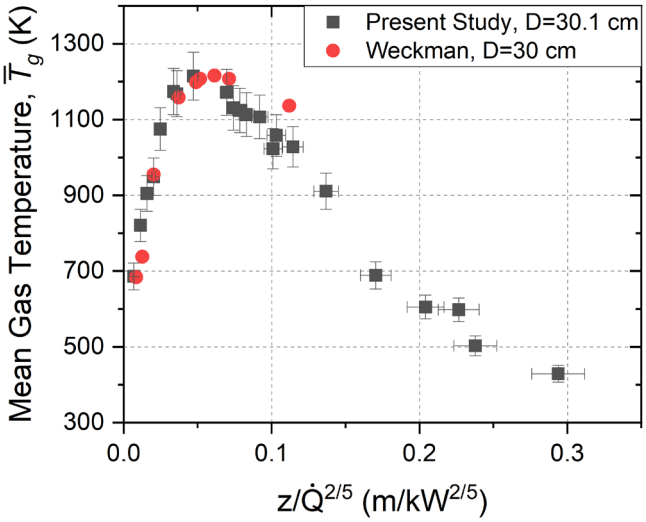

Fig. 19. The mean gas temperature along the fire centerline as a function of the axial distance above the fuel surface normalized by $\dot{Q}^{2/5}$ in the 30 cm acetone pool fire. The measurements by Weckman [41] are also shown.

3.4.4. Heptane Fire

Figure 20 shows the pooled mean gas temperature as a function of axial distance above the burner in the 30 cm heptane pool fire.

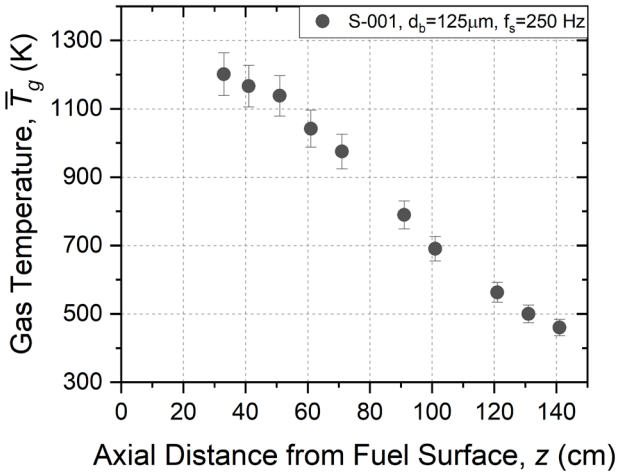

Fig. 20. The pooled gas temperature ($\overline{T}_g$) along the fire centerline as a function of axial distance above the fuel surface in the 30 cm heptane pool fire.

3.4.5. Methane Fire

Figure 21 shows the mean gas temperature measured using various thermocouples and the pooled mean gas temperature as a function of axial distance above the burner in the methane gas fire. The error bars indicate the expanded (k=2) combined uncertainty, representing a 95 % confidence interval.

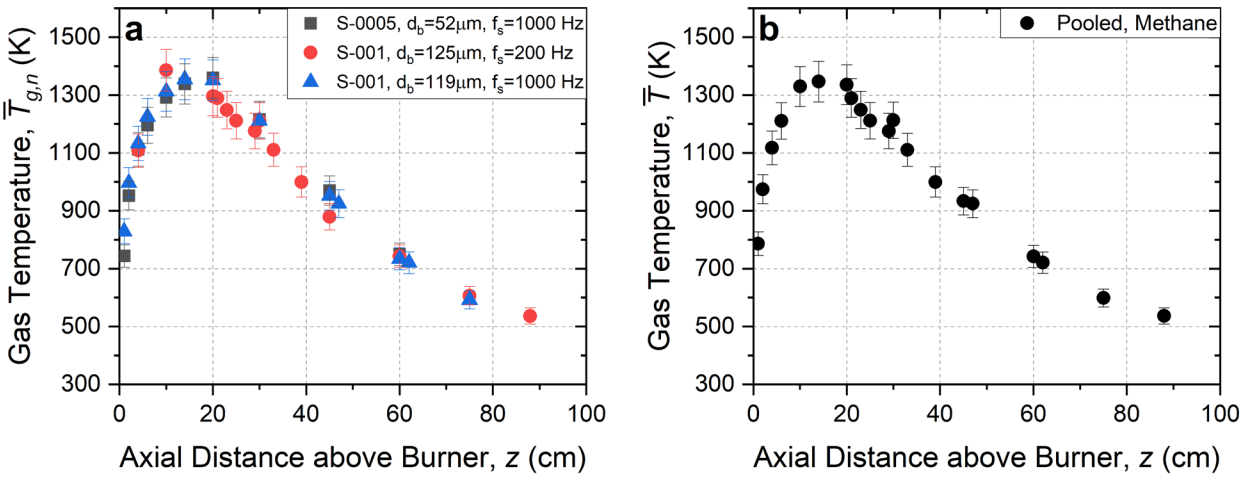

Fig. 21. The mean gas temperature along the fire centerline as a function of the axial distance above the burner surface in the methane gas fire: (a) mean gas temperature measured using the *n*th thermocouple ($\overline{T}_{g,n}$), (b) the pooled mean gas temperature ($\overline{T}_g$).

3.4.6. Propane Fires

Figures 22 - 24 show the mean gas temperature measured using various thermocouples and the pooled mean gas temperature as a function of axial distance above the burner in the propane gas fires.

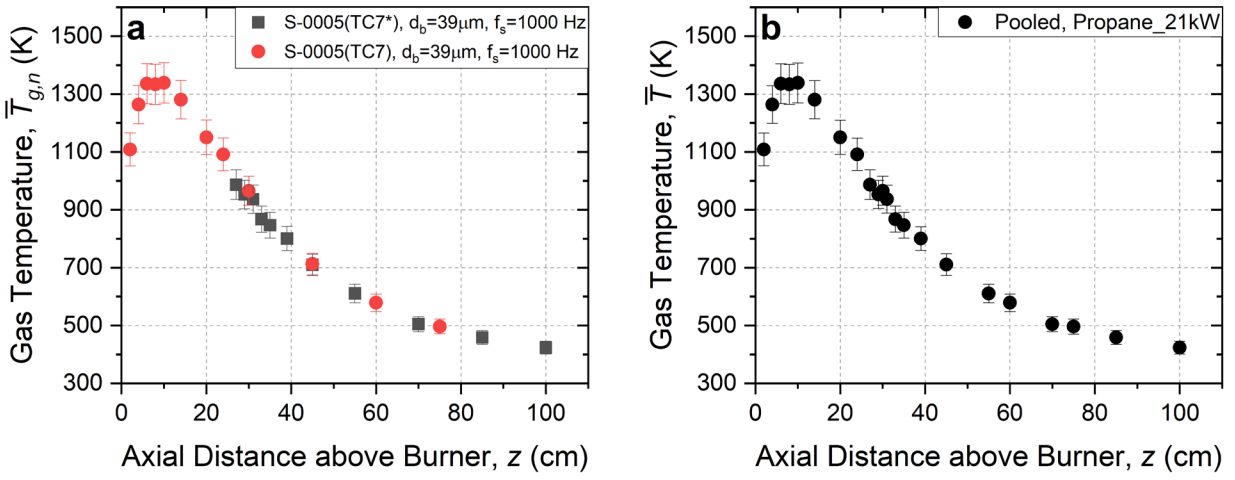

Fig. 22. The mean gas temperature along the fire centerline as a function of the axial distance above the burner in the 20 kW propane gas fire: (a) mean gas temperature measured using the *n*th thermocouple ($\overline{T}_{g,n}$), (b) the pooled mean gas temperature ($\overline{T}_g$).

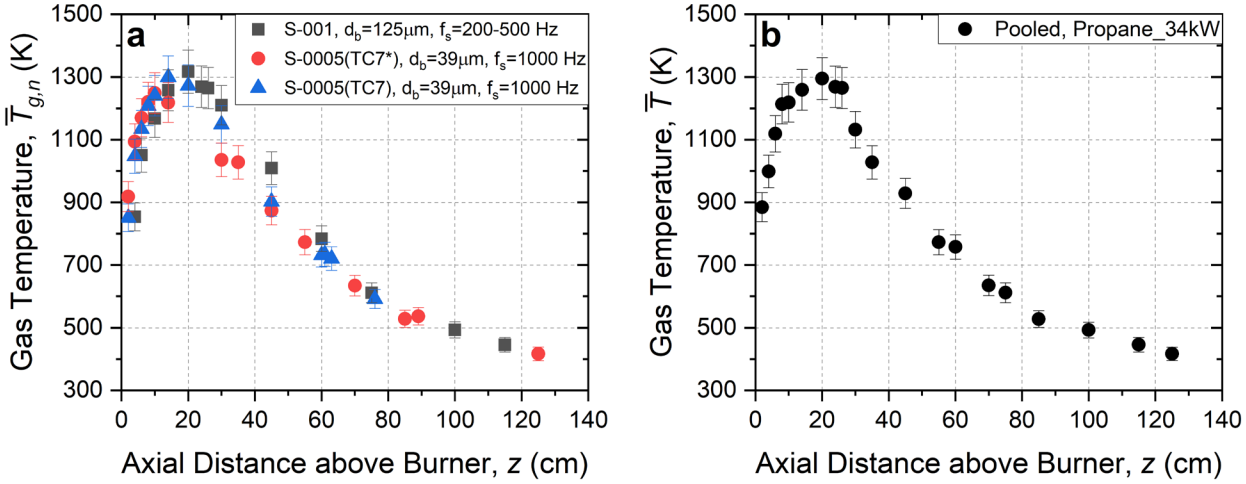

Fig. 23. The mean gas temperature along the fire centerline as a function of the axial distance above the burner in the 34 kW propane gas fire: (a) mean gas temperature measured using the *n*th thermocouple ($\overline{T}_{g,n}$), (b) the pooled mean gas temperature ($\overline{T}_g$).

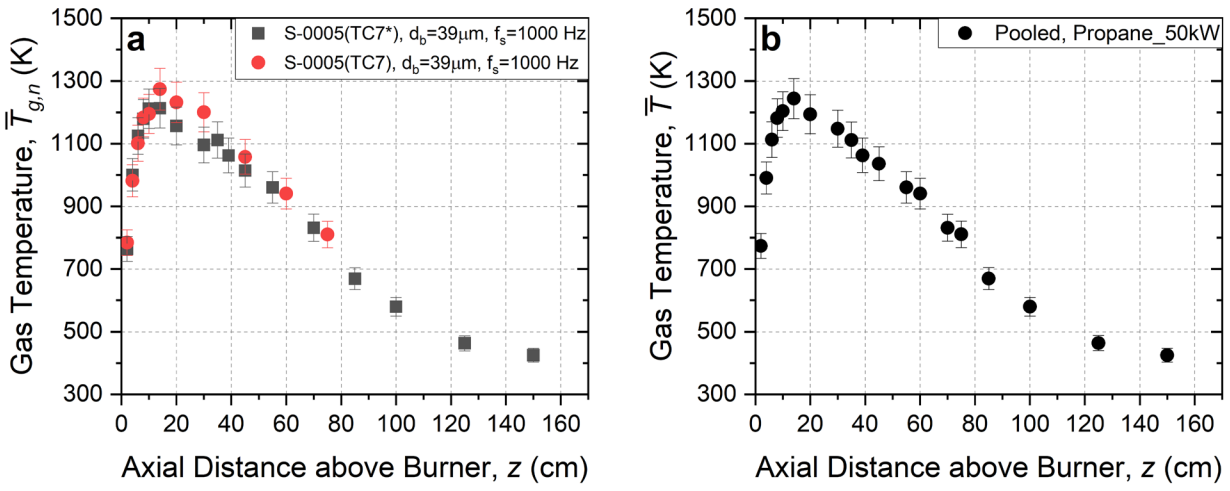

Fig. 24. The mean gas temperature along the fire centerline as a function of the axial distance above the burner in the 50 kW propane gas fire: (a) mean gas temperature measured using the n^{th} thermocouple ($\overline{T}_{g,n}$), (b) the pooled mean gas temperature ($\overline{T}_g$).

Table 5 lists the value and location of the measured peak temperature in the pool and gas. As expected, the methanol fire, has zero soot emission, exhibited the highest peak temperature. The acetone fire recorded the lowest peak temperature, approximately 140 K lower than that of the methanol fire. The location of the peak temperature occurred between 10 and 21 cm above the fuel surface in all the fires. An uncertainty analysis of the local temperature measurements is provided in *Appendix F.2*.

Table 5. Summary of the value and location of the measured peak temperature in the liquid and gaseous pool fires.

Case no.	Fuel	D [m]	$\dot{Q}$ [kW]	Peak $\overline{T}_g$ [K]	Peak location [cm]
1	Methanol	0.30	18.4	1355	10
2	Ethanol	0.30	27.8	1278	15
3	Acetone	0.30	42.0	1215	21
4	Heptane	0.30	112	na	na
5	Methane	0.30	34.5	1347	14
6	Propane	0.37	20.7	1339	10
7	Propane	0.37	34.4	1299	20
8	Propane	0.37	50.1	1254	14

3.5. Profile of the Upward Component of Velocity along the Fire Centerline

The mean of the upward component of velocity along the fire centerline for all of the fires tested is described in this section. The measurements were made by pressure transducers connected to a bidirectional probe in proximity to a fine thermocouple, as outlined in *Section 2.6*. The root mean-square (RMS) measurement of the mean upward flow speed in the fires is not included in this report. An uncertainty analysis of the measurements is provided in *Appendix F.1*.

3.5.1. Methanol Fire

Figure 25 shows the pooled mean gas velocity as a function of axial distance above the fuel surface in the 30 cm methanol fire. Careful measurements reported by Weckman and Strong [7], who used laser Doppler velocimetry (LDV) to determine the velocity field in the 30 cm methanol pool fire with a 1 cm lip height, are also shown and appear to agree with the current measurements within experimental uncertainty. The current dataset represents an extension of Weckman's centerline results [7] to locations more than four diameters downstream of the burner.

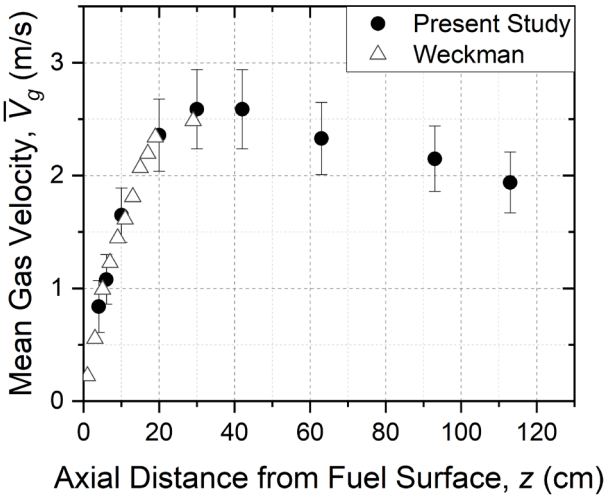

Fig. 25. The pooled mean gas velocity along the centerline in the upward direction as a function of axial distance above the fuel surface in the 30 cm methanol pool fire. Laser Doppler velocity measurements reported by Weckman and Strong [7] in a 30 cm methanol pool fire are also shown.

3.5.2. Ethanol Fire

Figure 26 shows the pooled mean gas velocity as a function of axial distance above the fuel surface in the 30 cm ethanol fire.

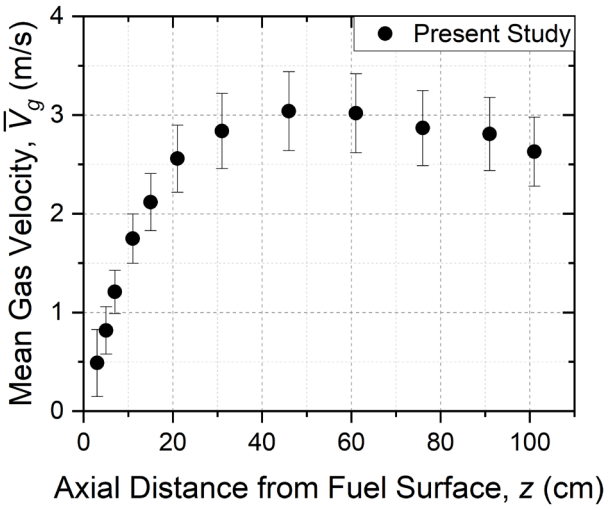

Fig. 26. The pooled mean gas velocity along the centerline in the upward direction as a function of axial distance above the fuel surface in the 30 cm ethanol pool fire.

3.5.3. Acetone Fire

Figure 27 shows the pooled mean gas as a function of axial distance above the fuel surface in the 30 cm acetone fire. Results by Weckman [41] in the 30 cm acetone pool fire (also with a 1 cm lip height) determined using LDV analogous to Ref. [7] are also shown. The measurements are in agreement with experimental uncertainty. The current dataset represents an extension of Weckman's results [41] to locations more than four diameters downstream of the burner.

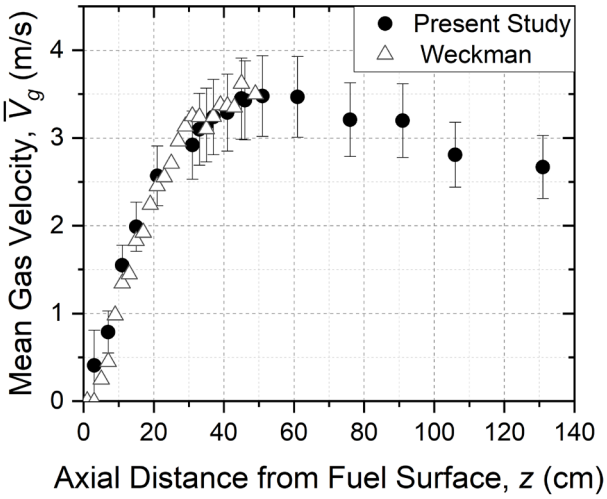

Fig. 27. The pooled mean gas velocity along the centerline in the upward direction as a function of axial distance above the fuel surface in the 30 cm acetone pool fire. Laser Doppler velocity measurements reported by Weckman [41] in a 30 cm acetone pool fire are also shown.

3.5.4. Heptane Fire

Figure 28 shows the pooled mean gas velocity as a function of axial distance above the fuel surface in the 30 cm heptane fire.

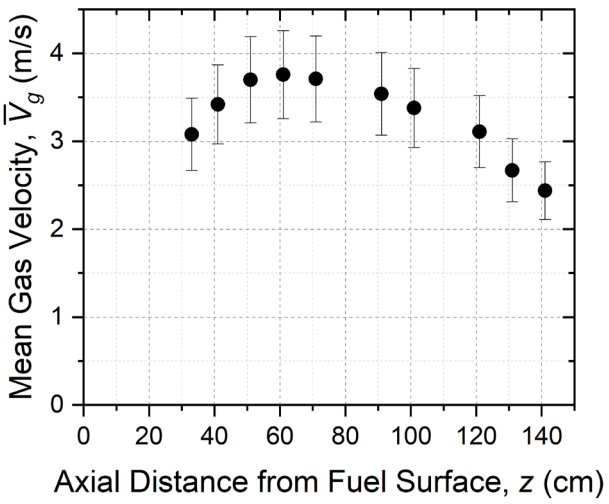

Fig. 28. The pooled mean gas velocity along the centerline in the upward direction as a function of axial distance above the fuel surface in the 30 cm heptane pool fire.

3.5.5. Methane Fire

Figure 29 shows the pooled mean gas as a function of axial distance above the burner (which is the fuel surface) in the 30 cm methane fire.

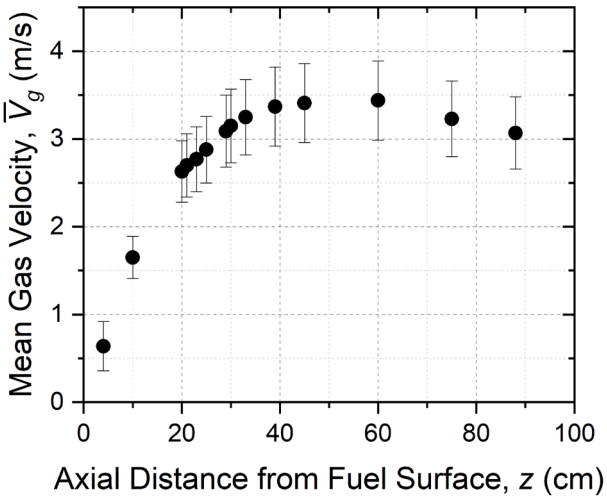

Fig. 29. The pooled mean gas velocity along the centerline in the upward direction as a function of axial distance above the burner in the 37 cm methane gas burner fire.

3.5.6. Propane Fires

Figures 30 - 32 show the pooled mean gas velocity measured by multiple pressure transducers as a function of axial distance above the burner in the 20 kW, 34 kW, and 50 kW propane gas fires, respectively.

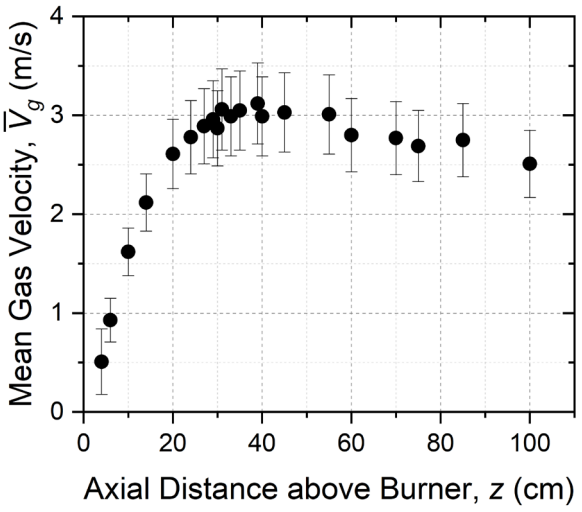

Fig. 30. The pooled mean gas velocity along the centerline in the upward direction as a function of axial distance above the burner in the 20 kW propane gas fire.

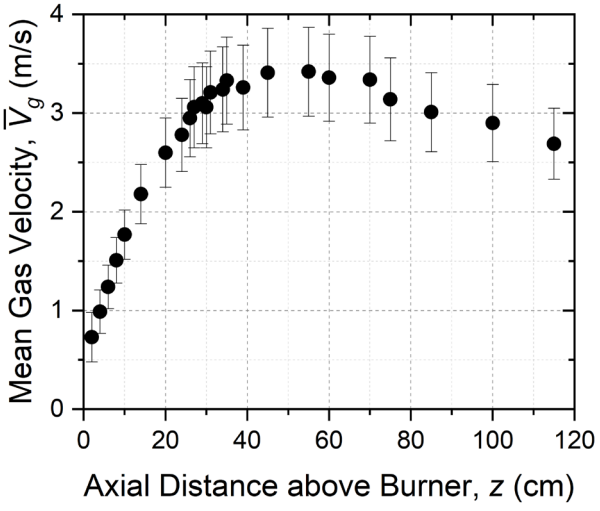

Fig. 31. The pooled mean gas velocity along the centerline in the upward direction as a function of axial distance above the burner in the 34 kW propane gas fire.

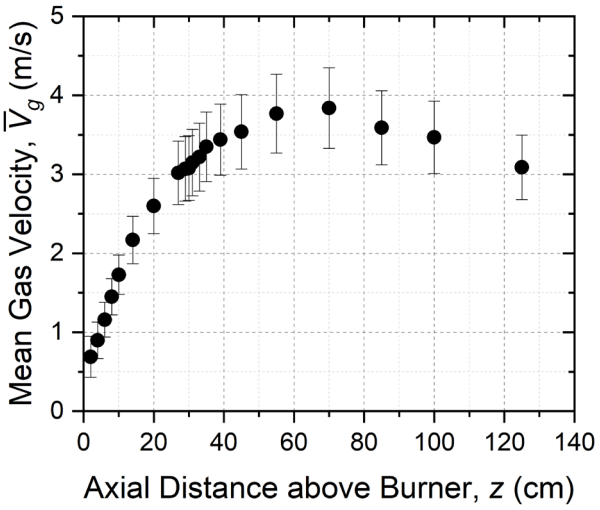

Fig. 32. The pooled mean gas velocity along the centerline in the upward direction as a function of axial distance above the burner in the 50 kW propane gas fire.

3.5.7. Comparison to Plume Theory

Baum and McCaffrey [42] developed a theoretical plume correlation based on kinematic relationships between the velocity, vorticity, and heat release field in an isolated fire plume non-dimensionalized by D^* for length scale and $\sqrt{gD^*}$ for velocity. The upstream gas velocity along the centerline is defined as:

$$\frac{V_g}{\sqrt{gD^*}} = A\left(\frac{z}{D^*}\right)^n \tag{12}$$

where D^* is the plume scaling involving the heat release rate, defined by $(\dot{Q}/(\rho_o c_p T_o \sqrt{g}))^{\frac{2}{5}}$; where $\dot{Q}$ is the ideal heat release rate, and ρ_o and c_p are the density and specific heat of air, respectively, at the ambient temperature (T_o). The quantities n and A for each plume region are defined by the range of z/D^* as given in Table 6. Details of the plume correlation and the plume regions are described in Ref. [42].

Table 6. Baum and McCaffrey's [42] plume correlation parameters in different fire regions.

Plume Region	Range	n	A
Flame	$0 < z/D^* < 1.32$	1/2	2.18
Intermittent	$1.32 < z/D^* < 3.30$	0	2.45
Plume	$3.30 < z/D^*$	-1/3	3.64

Figure 33 shows the dimensionless mean gas velocity ($V_g/\sqrt{gD^*}$) as a function of the dimensionless distance above the burner (z/D^*), compared with Baum and McCaffrey's plume theory (solid line) [42] in the pool fires. Error bars indicate the expanded (k=2) combined uncertainty. The hollow circle and solid triangle symbols represent the present study and Weckman's results [7, 41], respectively. Baum and McCaffrey's correlation overpredicts at every measurement position for all fuels. On the other hand, the velocity profile structure for the distinct plume regions follows the trends of Baum and McCaffery's correlation.

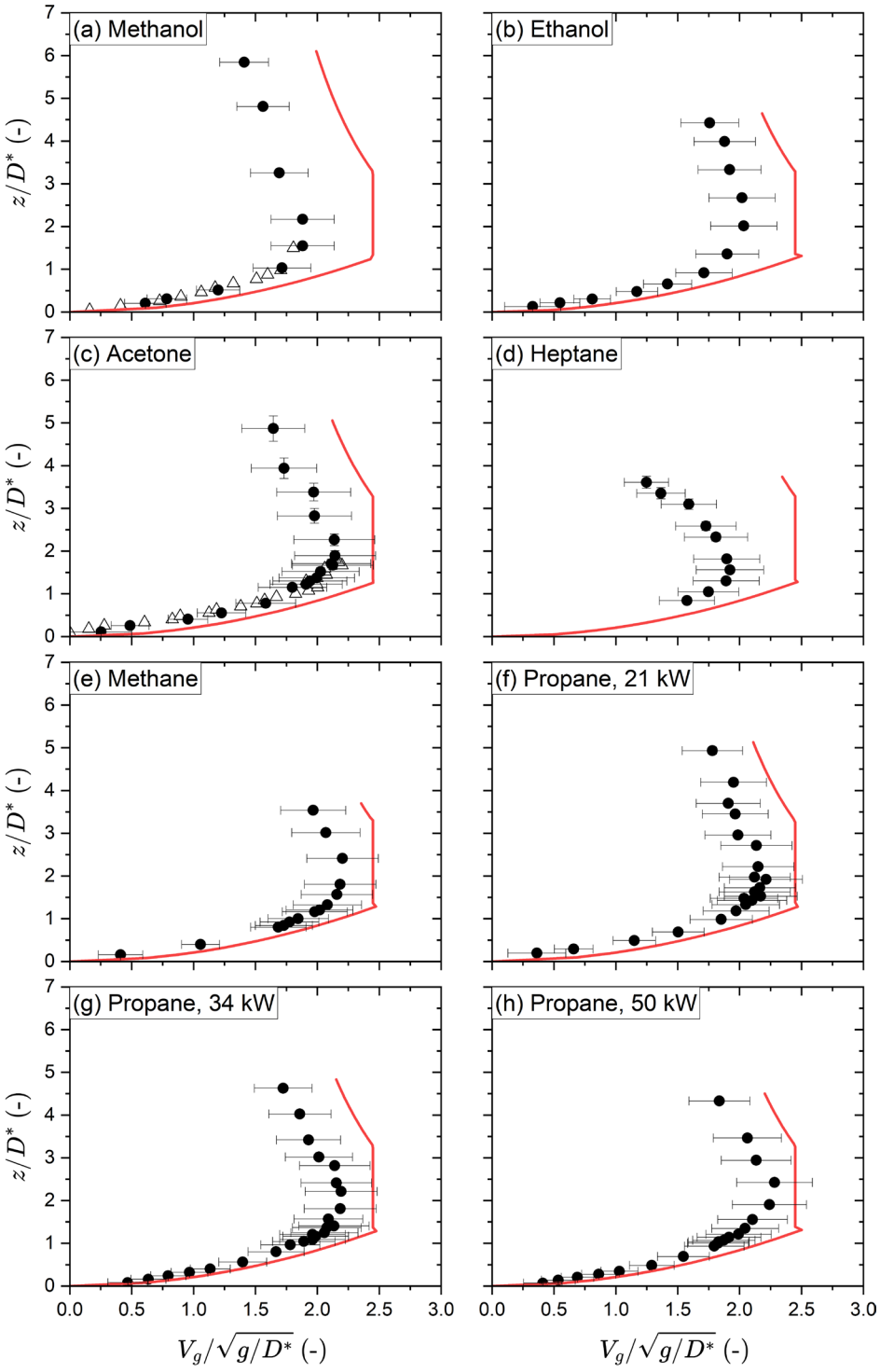

Fig. 33. The dimensionless mean gas velocity $V_g/\sqrt{g/D^*}$ along the fire centerline as a function of dimensionless axial distance above the pool surface (z/D^*) compared with Baum and McCaffrey plume theory (solid line) in the (a) methanol, (b) ethanol, (c) acetone, (d) heptane, (e) methane, (f) 20 kW propane, (g) 34 kW propane, and (h) 50 kW propane pool fires. The solid circles and hollow triangles represent the present study and Weckman's results [7, 41], respectively.

Table 7 lists the value and location of the measured peak upward axial velocity. The results showed that the largest fires (in terms of heat release rate) had the largest peak velocity and that the smallest fires had the smallest peak velocity. Although there are correlations that provide an estimate of the value of the peak velocity above the pool centerline, they are not employed here because the inputs for those correlations are not accurately known for the fires studied here. The needed information includes the position of the virtual origin of the fires, the combustion efficiency, the radiative fraction to the surroundings (including the fuel surface), the fractional heat losses to the burner, and the fractional enthalpy that convectively heats the fuel surface [43]. Many correlations provide the virtual origin, which differs significantly, particularly for low Froude number pool fires such as those studied here.

Table 7. Summary of the value and location of the measured peak upward axial velocity along the centerline.

Case no.	Fuel	D [m]	$\dot{Q}$ [kW]	Peak $\overline{V}_g$ [m/s]	Peak $\overline{V}_g$ location [cm]
1	Methanol	0.30	18.4	2.6	29 – 41
2	Ethanol	0.30	27.8	3.0	45
3	Acetone	0.30	42.0	3.5	50
4	Heptane	0.30	106.6	3.8	60
5	Methane	0.37	34.5	3.4	60
6	Propane	0.37	20.7	3.1	35 – 40
7	Propane	0.37	34.4	3.4	45 – 55
8	Propane	0.37	50.1	3.8	70

3.6. Local Heat Flux Distribution to the Surroundings

Figures 34 - 40 show (a) the local radiative heat flux normalized by the ideal heat release rate in the radial direction as a function of the normalized axial distance from the fuel surface normalized by the pool diameter and (b) the local radiative heat flux in the downward direction as a function of the radial distance from the pool centerline normalized by the pool diameter. Error bars indicate the expanded (k=2) combined uncertainty, representing a 95 % confidence interval.

The heat flux in the radial direction typically obtained maxima at about 10 cm to 20 cm above the fuel surface and then decreased. The heat flux in the downward direction decreased with distance from the fire as $\dot{q}'' \sim 1/r^2$. Tables H1 - H5 list the local radiative heat flux for each of the fires 1 in the radial direction as a function of the vertical location at a distance (r) from the pool centerline and 2 in the downward direction as a function of position in the radial direction at a z-location equal to the fuel surface or gas burner (see Fig. 7).

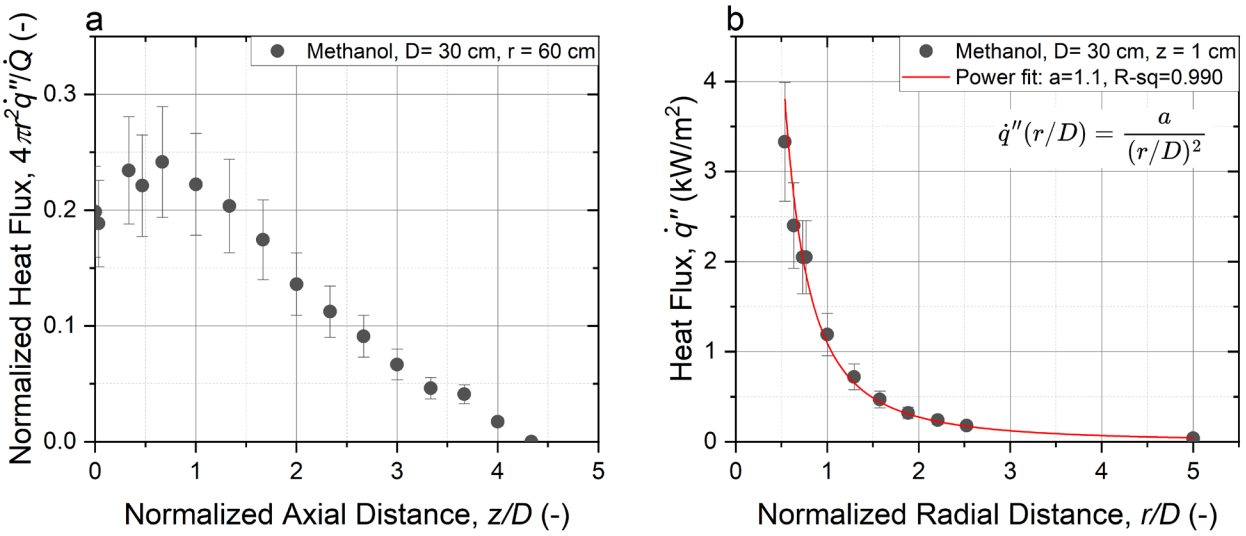

Fig. 34. (a) Mean heat flux normalized by the total heat release rate as a function of the axial distance normalized by the pool diameter in the 30 cm methanol fire, (b) Mean heat flux as a function of the radial distance normalized by the pool diameter [11].

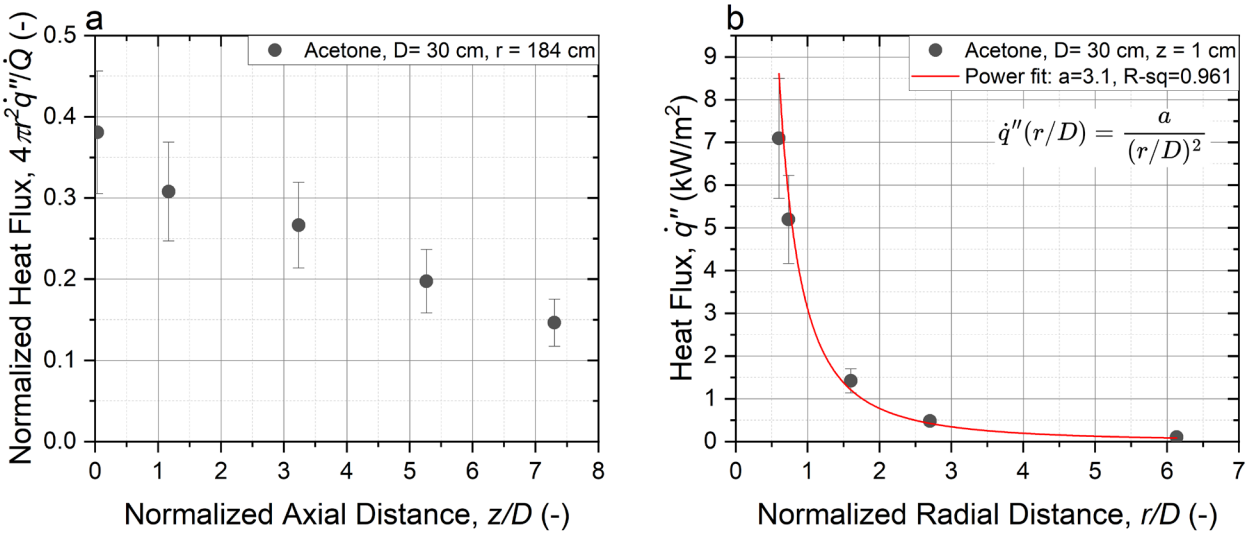

Fig. 35. (a) Mean heat flux normalized by the total heat release rate as a function of the axial distance normalized by the pool diameter in the 30 cm acetone fire, (b) Mean heat flux as a function of the radial distance normalized by the pool diameter.

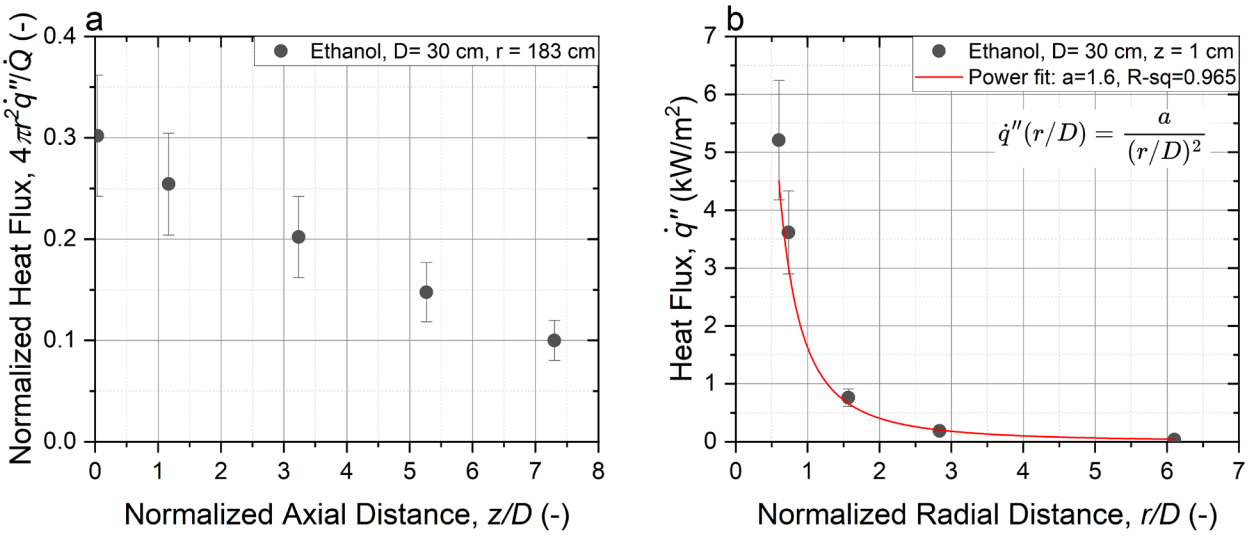

Fig. 36. (a) Mean heat flux normalized by the total heat release rate as a function of the axial distance normalized by the pool diameter in the 30 cm ethanol fire, (b) Mean heat flux as a function of the radial distance normalized by the pool diameter.

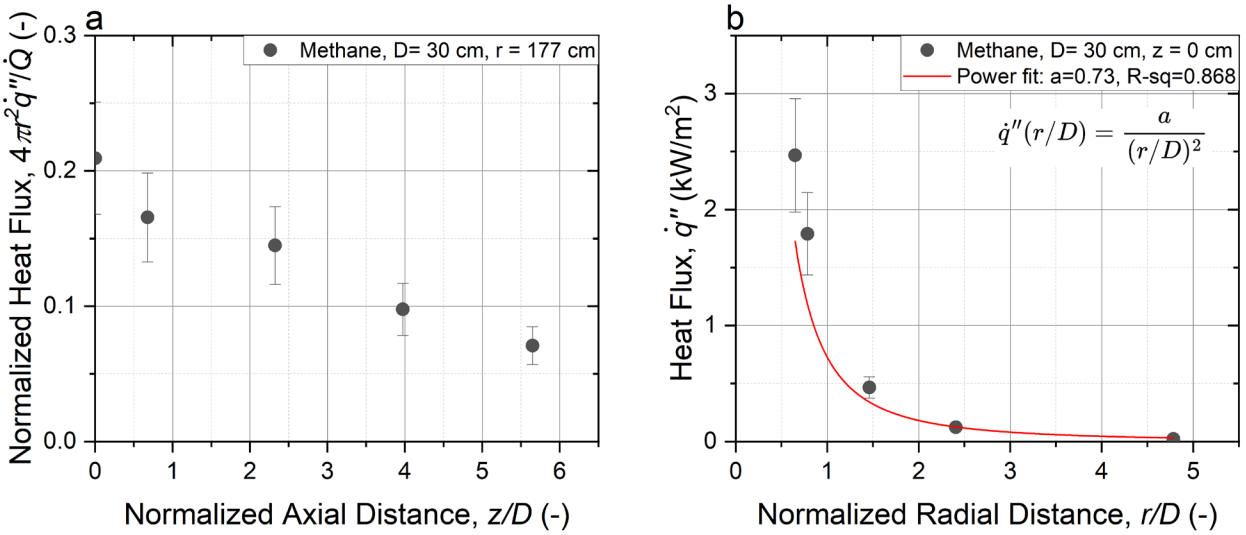

Fig. 37. (a) Mean heat flux normalized by the total heat release rate as a function of the axial distance normalized by the burner diameter in the methane fire, (b) Mean heat flux as a function of the radial distance normalized by the burner diameter.

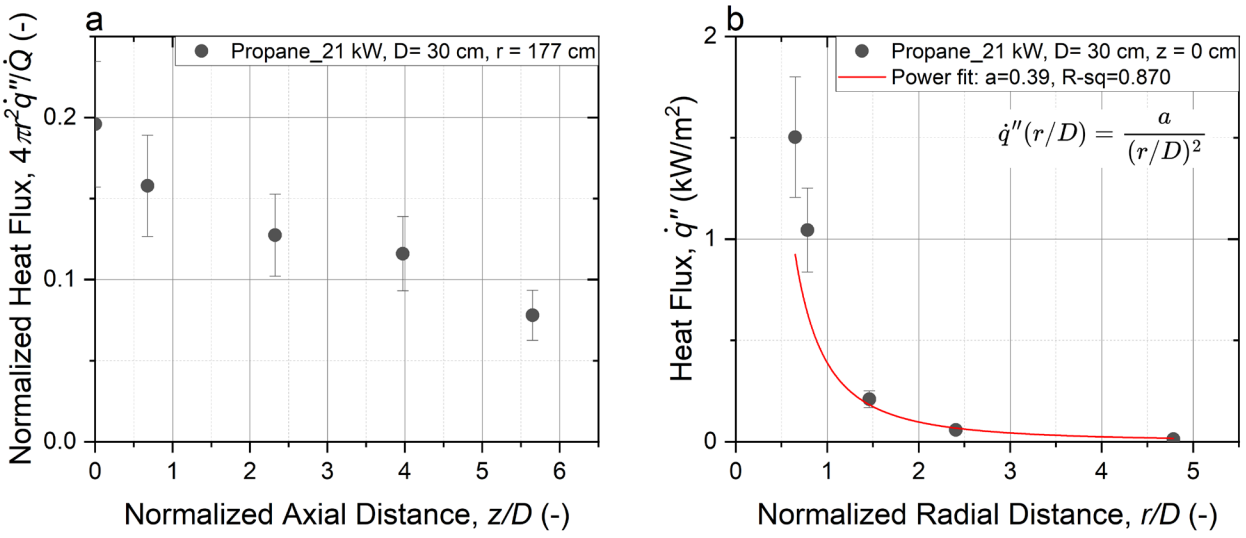

Fig. 38. (a) Mean heat flux normalized by the total heat release rate as a function of the axial distance normalized by the burner diameter in the 20 kW propane fire, (b) Mean heat flux as a function of the radial distance normalized by the burner diameter.

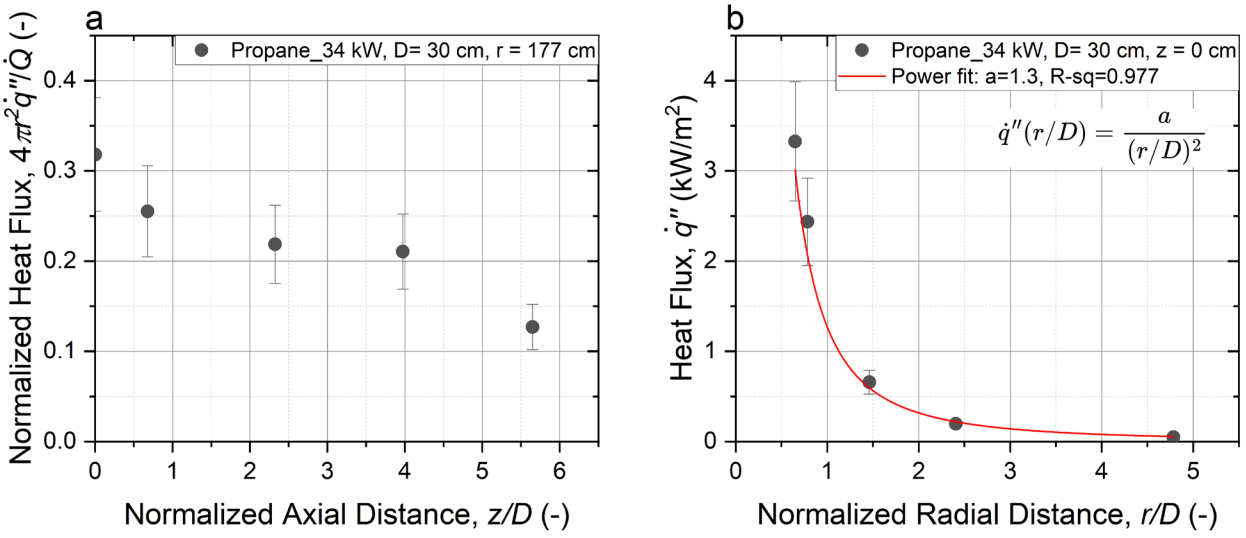

Fig. 39. (a) Mean heat flux normalized by the total heat release rate as a function of the axial distance normalized by the burner diameter in the 34 kW propane fire, (b) Mean heat flux as a function of the radial distance normalized by the burner diameter.

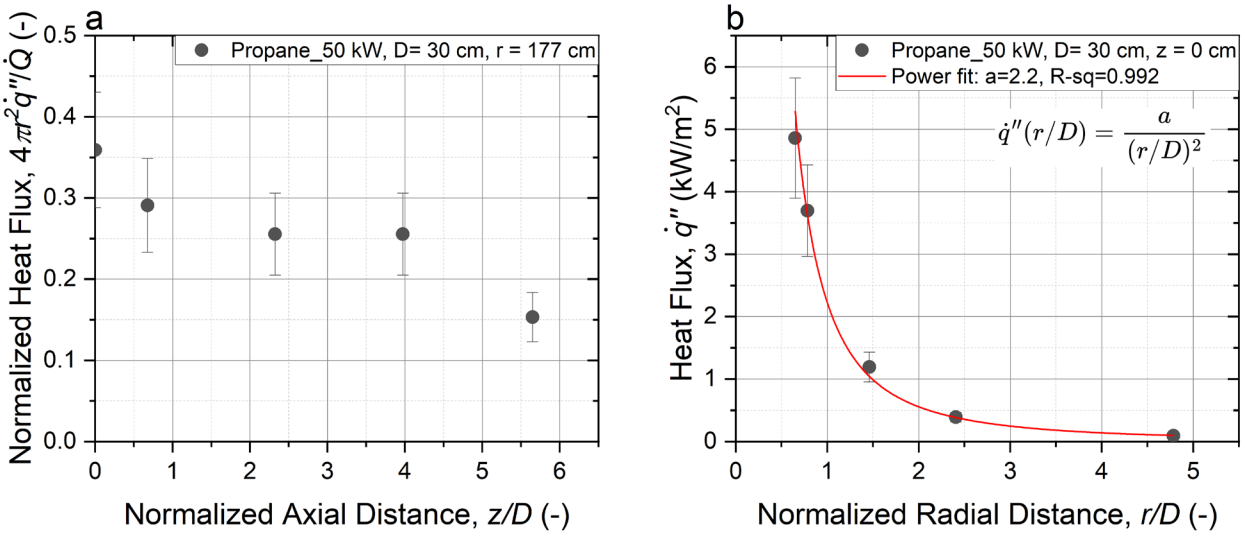

Fig. 40. (a) Mean heat flux normalized by the total heat release rate as a function of the axial distance normalized by the burner diameter in the 50 kW propane fire, (b) Mean heat flux as a function of the radial distance normalized by the burner diameter.

3.7. Single-Location Radiative Fraction

The radiative fraction determined for the 30 cm liquid and 37 cm gaseous pool fires was estimated from a single location heat flux measurement, assuming isotropy. Table 8 presents the ideal heat release rate and radiative fraction from single-location measurements in the 30 cm pool liquid fuel fires and the 37 cm burner gas fires. The uncertainty represents a 95 % confidence interval, where r is the radial distance from the pool center where the heat flux was measured.

The radiative fraction of each fuel fire in each repeat measurement and uncertainty analysis are provided in *Appendix F.5*. The radiative fraction estimate was about the same regardless of the radial distance in each fuel fire.

Table 9 presents a summary of previous measurements reported on the radiative fraction (χ_{rad}) determined using single- and multi-location heat flux measurements and the fractional energy radiated to the surroundings (χ_r) in steadily burning 30 cm methanol pool fires with 0.5 cm and 1 cm lip heights (see Section 2.8).

Table 8. The ideal heat release rate ($\dot{Q}$) and the estimated radiative fraction from single-location measurements (χ_{rad}) in the 30 cm liquid and the 37 cm gaseous pool fires, where r is the radial distance from the pool center.

Case no.	Fuel	D [m]	$\dot{Q}$ [kW]	χ_{rad} [-]	r/D [-]
1	Methanol	0.30	18.4	0.23 ± 0.04	6.4 - 10.0
2	Ethanol	0.30	27.8	0.26 ± 0.04	6.9 - 8.4
3	Acetone	0.30	42.0	0.31 ± 0.07	6.8 - 10.2
4	Heptane	0.30	106.6	0.35 ± 0.09	6.8 - 7.8
5	Methane	0.37	34.5	0.21 ± 0.04	5.0 - 6.2
6	Propane	0.37	20.7	0.23 ± 0.04	5.5 - 6.2
7	Propane	0.37	34.4	0.30 ± 0.05	5.5 - 6.2
8	Propane	0.37	50.1	0.33 ± 0.06	5.5 - 6.2

Some studies measured one or sometimes two of the parameters of interest. It is possible to estimate the value of χ_{rad} for the 30 cm methanol fire from the measurement of χ_r using the relationship between these parameters determined from the measurements described in Ref. [11], which shows that:

$$\chi_{rad} = 1.13\ \chi_r \tag{13}$$

The average values of χ_{rad}, considering all the single and multi-location measurements from the literature and the measurements from this study, are listed in Table 9 and are equal to 0.22 ± 0.02 where the uncertainty represents the standard deviation, considering all of the measurement results).

Table 9. Summary of previous measurements of χ_{rad} from single and multi-location measurements and χ_r in the 30 cm methanol pool fire.

χ_r	χ_{rad} (multi-location)	χ_{rad} (single-location)	References
-	-	0.23 ± 19 % [a]	Table F30 (this study)
0.18	0.20 [b]	0.2	Hamins et al. [44]
-	0.23 [c]	-	Hamins et al. [8]
0.20 [d]	0.23	-	Klassen and Gore [9]
0.22	0.24 [b]	-	Buch et al. [45]
0.19	0.24	-	Kim et al. [11]
0.20 ± 0.02	0.22 ± 0.02		Average ± SD

a) Expanded (k=2) combined uncertainty corresponding to a 95 % confidence interval.
b) Eq. 10 was used to estimate χ_{rad} from the reported measurement of χ_r.
c) Results from Ref. [8] were recalculated, correcting errors in H_c and assumptions about $\dot{Q}_{sr}$ [24].
d) Recalculated χ_r, using ΔH_c = 19.90 kJ/g [32], not 22.37 kJ/g, assuming gaseous water as the product of combustion.

Figure 41 shows the radiative fraction (χ_{rad}) as a function of ideal heat release rate ($\dot{m}H_c$) in the propane gas fires compared with Ref. [31]. The radiative fraction increased with the ideal heat release rate and the current measurements agree with the results in Ref. [31] within experimental uncertainty.

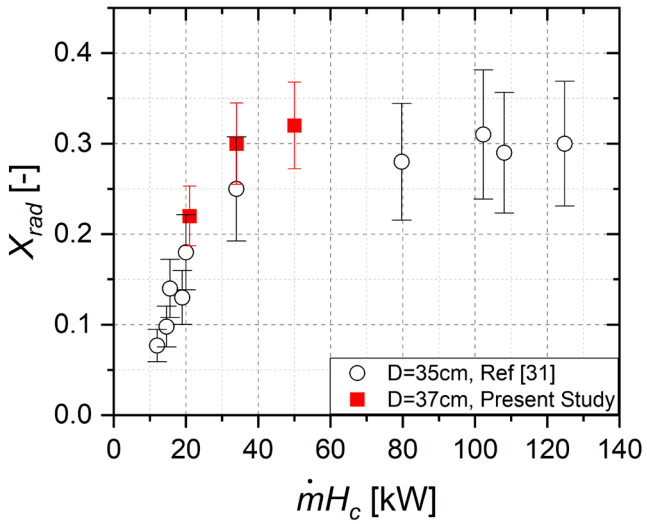

Fig. 41. Radiative fraction (χ_{rad}) as a function of the ideal heat release rate ($\dot{m}H_c$) in the 37 cm diameter propane gas fires as compared to Ref. [31].

3.8. Heat Feedback to the Pool Surface

3.8.1. Profile of Local Heat Feedback

Figure 42 shows the measured local heat flux towards the fuel surface at a vertical location approximately 3 mm above the fuel surface as a function of radial distance from the burner centerline in the methanol, ethanol, acetone, and heptane fires – these results are taken from Refs. [8, 11][4] and are shown here for completeness. The local heat flux measurement results are also tabulated in *Appendix F.5*. For all of the fires burning the liquid fuels, the results show that the total local heat flux decreases moderately from the pool center, where it is between 22 kW/m^2 to 33 kW/m^2 until about r =12 cm, where the total heat flux is nominally 20 kW/m^2. For the methanol and ethanol fires, the total heat flux rapidly decreases from 12 cm to 14.5 cm, near the burner edge, where it is less than 10 kW/m^2. For the acetone and heptane fires, the total heat flux increases from 12 cm to 14.5 cm. The acetone data in Figure 42 includes about 60 independent measurements from 5 different experiments; the data at r = 14 cm and r = 14.5 cm represent 14 independent measurements.[5] Differences in the local heat flux seen in Figure 42 is attributed to the details of the complex structure of the fires, which influences the details of the radiative and convective heat transfer from the fires to the pool surface.

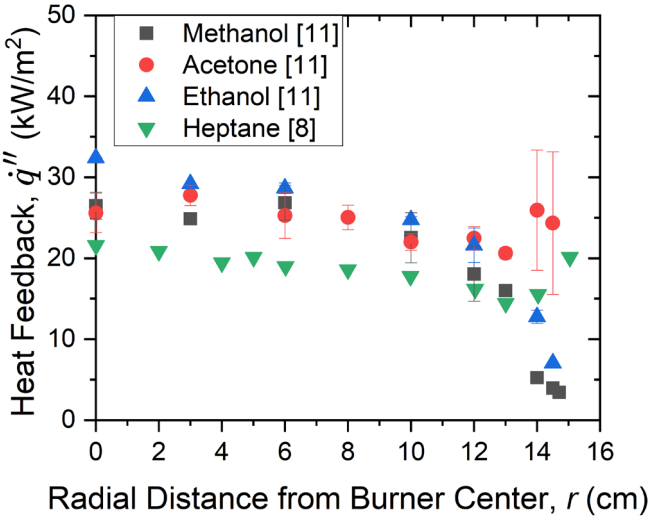

Fig. 42. Total local heat feedback onto the pool surface as a function of radial distance from the burner centerline in the methanol, ethanol, acetone and heptane fires [8, 11]. Error bars indicate the standard deviation of the mean heat flux from repeat measurements.

[4] for which the same 30.1 cm diameter, water-cooled, stainless steel burner was employed as used here.

[5] The standard deviation for these locations in the acetone fire is relatively large, which may be due to the sensitivity of the flux gauge to its azimuthal and vertical location relative to the channels and nodes associated with the dynamic structure of the acetone fire.

3.8.2. Total Heat Feedback to the Pool Surface

The total heat feedback to the burner surface per unit time in the gaseous pool fires ($\dot{Q}_b$) was calculated using Eq. 11. Normalizing by the total heat release rate ($\dot{Q}$) allows calculation of the fractional total heat feedback (χ_b).

Table 10 lists the fractional total heat feedback (χ_b) and the fractional radiative heat feedback to the pool surface (χ_{br}) of the liquid and gaseous fuel pool fires. Reference [11] provides values of χ_b and χ_{br} for the methanol, ethanol and acetone pool fires. Results for heptane were obtained by integrating the detailed local profiles of total heat flux and radiative heat flux to the pool surface [8] and normalizing the results by the total heat release rate of the fire. The model described in Ref. [31] was used to determine χ_{br} in the gaseous pool fires. The relative expanded (k=2) combined uncertainty for χ_{br} is approximately equal to 15 % [31]. The results in Table 10 indicate that the fractional percentage of heat feedback due to radiative heat transfer (χ_{br}/χ_b) varies widely for these medium-scale pool fires, ranging about 30 % in the methane fire to 87 % and 95 % in the acetone and heptane fires, respectively.

Table 10. The fractional total heat feedback (χ_b) and the fractional radiative heat feedback to the pool surface (χ_{br}) of the liquid and gaseous pool fires.

Case no.	Fuel	D [cm]	χ_b [-]	χ_{br} [-]
1 [11]	Methanol	0.30	0.082 ± 0.020	0.055 ± 0.012
2 [11]	Ethanol	0.30	0.050 ± 0.012	0.042 ± 0.007
3 [11]	Acetone	0.30	0.046 ± 0.011	0.040 ± 0.006
4 [8]	Heptane	0.30	0.011 ± 0.003	0.010 ± 0.002
5	Methane	0.37	0.07 ± 0.003	0.02 ± 0.003
6	Propane	0.37	0.13 ± 0.010	0.05 ± 0.010
7	Propane	0.37	0.08 ± 0.007	0.03 ± 0.002
8	Propane	0.37	0.05 ± 0.005	0.03 ± 0.008

Figure 43 shows χ_b for the 37 cm diameter propane pool fires as a function of the heat release rate normalized by the pool surface area ($\dot{m}H_c/A_b$). The results in the figure are compared to the experimental and modeling results reported in Ref. [31], which used the same burner.

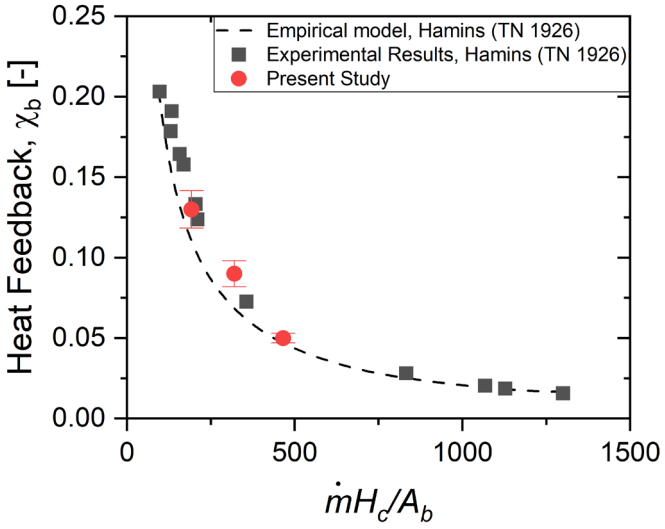

Fig. 43. The measured fractional total heat feedback (χ_b) to the burner surface for propane fires as a function of the heat release rate normalized by the pool surface area. The results of the present study are compared to the experimental and modeling results given in Ref. [31].

3.9. Fuel Surface Temperature

Table 11 lists the steady-state burner surface temperature at *r* = 2.5 cm and 16 cm from the burner center, as well as the cooling water temperature at the inlet/outlet of the burner in the methane and propane gas fires. The gas burner surface temperatures depend on the cooling water flow and the water inlet temperature. The difference between the water temperature at the burner inlet and outlet allows the calculation of the total heat feedback to the burner, as reported in *Section 2.1*. For the conditions considered here, the burner surface temperature was about 74 °C ± 3 °C on average for all the experiments. Tables F36 - F37 in *Appendix F.5* list the mean values of the burner cooling water temperature, the water flow rate, the estimated heat feedback, and the fractional heat feedback to the burner in the gaseous methane and propane fires.

Table 11. Burner surface temperature (T_{surf}) at *r* = 2.5 cm and 16 cm from the burner center and the cooling water temperature (T_w) at the inlet/outlet of the burner in the methane and propane gas fires. The uncertainty represents the standard deviation of the mean temperature in repeat measurements.

Case no.	Fuel	$\dot{Q}$ [kW]	T_{surf} at *r*=16 cm [ºC]	$T_{w,in}$ [ºC]	$T_{w,out}$ [ºC]	Repeat
5	Methane	34.5	73 ± 2	18 ± 0.2	61 ± 2	4
6	Propane	20.7	71	18	64	1
7	Propane	34.4	77	18	64	1
8	Propane	50.1	76	18	61	1

Figure 44 shows the fuel temperature profile as a function of time at each measurement position in the 30 cm diameter methanol, acetone, and ethanol fires, where z is the absolute value of the axial distance below the fuel surface. The burner side wall temperature was measured using the IR camera in the acetone fire, which is indicated by the lines with symbols in the figure. Figure 45 shows an IR image of the fuel surface in the ethanol fire immediately after the fuel was shut and within 2 s after the flames went out. The fuel surface temperature appears to be nearly uniform with the temperature near the pool center equal to about 61 ℃ according to the thermal camera. The thermocouple results show that the fuel surface temperature slowly increased with time until after about 2000 s, the surface temperature was larger than the fuel boiling point by about 1 K to 2 K in the acetone and ethanol fires. We speculate that this is possibly due to the changing chemical composition of the liquid surface from a pure fuel to a pure fuel diluted by water and potentially other combustion products as they back diffuse from the gas phase to condense on the fuel surface. This phenomenon of water back diffusion and condensation has been previously documented in a counterflow liquid pool flame [19]. This topic would benefit from further investigation.

The fuel surface temperature increased linearly in time. The fuel surface temperature is about 3 ℃ larger than the boiling temperature in the ethanol fire after 4000 s. The fuel temperatures in the 30 cm methanol, acetone, and ethanol fires are listed in *Appendix G* every 50 s using a 10 s running average.

A summary of the measured liquid fuel temperature is provided in Table 12. Summary of the measured pool surface temperature. The boiling point is also provided. The uncertainty represents the temperature increase during an experiment of about 1 hr duration. Table 12. The surface temperature was found to be very similar to the boiling point of the liquid fuel.

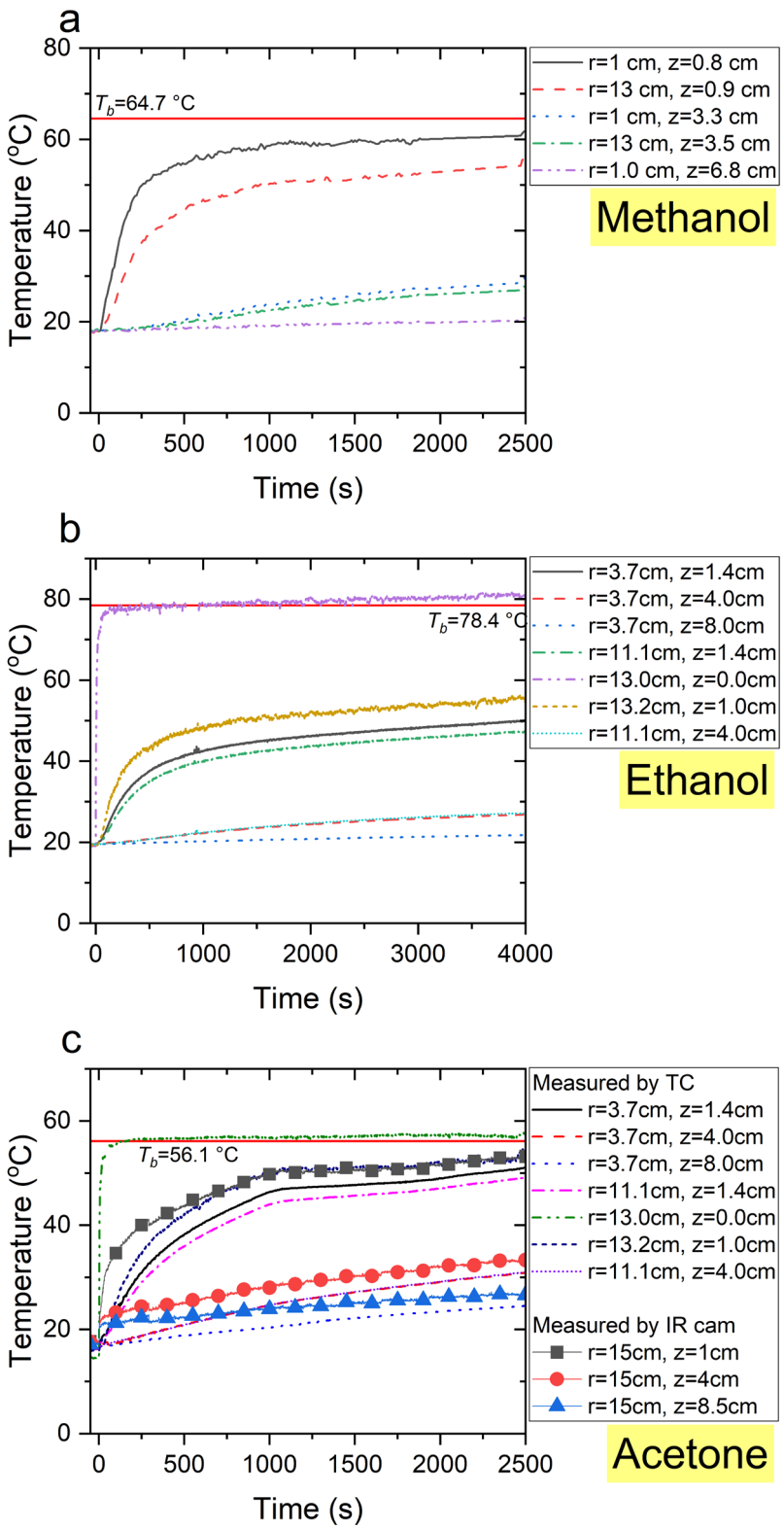

Fig. 44. Liquid fuel temperature profile as a function of time: (top) methanol, (middle) acetone, (bottom) ethanol. The lines with symbols in the acetone fire indicate the burner side wall temperatures measured using an IR camera.

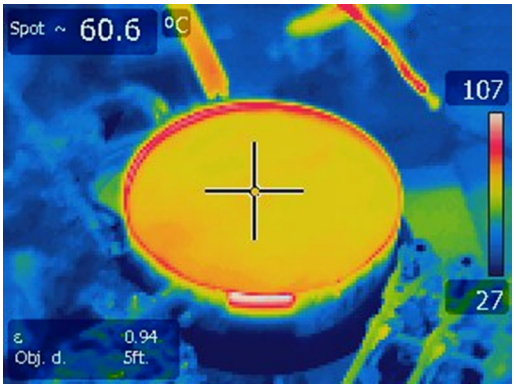

Fig. 45. An IR image of the fuel surface in the 30 cm ethanol pool fire immediately within 2 s after the flames were suppressed.

Table 12. Summary of the measured pool surface temperature. The boiling point is also provided. The uncertainty represents the temperature increase during an experiment of about 1 hr duration.

Case no.	Fuel	$\dot{Q}$ [kW]	T_{surf} [ºC]	T_b [ºC]
1	Methanol	18.4	65 ± 1	64.7
2	Ethanol	27.8	79 ± 2	78.3
3	Acetone	42.0	57 ± 1	56.1
4	Heptane	106.6	65 ± 1	98.4

4. Conclusions

In summary, this report presents global and local measurements characterizing key features of the structure of eight medium-scale pool fires (0.3 m to 0. 4 m) steadily burning a variety of liquid and gaseous fuels. This report includes new measurements and incorporates previous NIST measurements to provide a comprehensive description of these steadily burning fires. The following global and local measurements are reported:

Global measurements

Compilation of Global Pool Fire Features

Table 13 presents a compilation of measurements from the technical literature that characterizes the key global features of nine pool fires studied by NIST and others. The table includes the eight medium-scale pool fires (0.3 m to 0. 4 m) addressed in this report plus a 1 m diameter liquid pool fire burning methanol, which was previously investigated by NIST. The eight medium-scale fires include four 30 cm diameter liquid pool fires (burning methanol, ethanol, acetone, and heptane) and four 37 cm diameter gaseous pool fires burning methane

(34 kW) and propane (20 kW, 34 kW, and 50 kW). The table shows the average values of the pool fires' mass burning flux, the radiative fraction, the heat feedback to the pool surface, flame height, fractional heat feedback to the fuel from the fire, and the CO and soot yields. The table summarizes the measurements presented in this report as well as measurements from the technical literature. References for each of the measurements are provided in a companion table (Table I1 in *Appendix I*).

Table 13. Compilation of mean global pool fire characteristics from the literature, including the measured fuel mass flux ($\dot{m}''$), fuel surface temperature (T_s), radiative fraction (χ_{rad}), the dominant puffing frequency (Freq), the flame height (L_f), the fractional heat feedback to the fuel surface (χ_b), and the yields of CO (Y_{CO}) and soot (Y_s). The uncertainties in the table represent the standard deviation of the averaged values.

ID	Fuel	$\dot{m}''$	T_s	χ_{rad}	Freq	L_f	χ_b	Y_{CO}	Y_s
cm	-	g/(m^2-s)	°C	-	Hz	m	-	10^{-3} g/g	10^{-3} g/g
30.1	Methanol	13.1±0.8	65±1	0.24±0.01	2.7 ±0.1	0.41±0.06	0.082	b	0 [c]
30.1	Ethanol	14.6±0.9	79±2	0.26	2.4	0.60	0.050	0.3±0.1	b
30.1	Acetone	18.8±1.0	57±1	0.31	2.5	0.84	0.046	1.0±0.2	0.9±0.3
30.1	Heptane	35.5±1.4	na[d]	0.31±0.04	2.8	1.32±0.01	0.011	10.1±1.3	16.9±0.5
37	Methane	6.4	73±2	0.18±0.028	2.5	0.74±0.03	0.048 ±0.023	1.2±0.1	b
37	Propane	4.2	71	0.21±0.02	2.2	0.53	0.13	4.0±0.4	1.9±0.5
37	Propane	6.9	77	0.25±0.05	2.4	0.75	0.078 ±0.002	3.6±0.4	4.6±0.4
37	Propane	10.0	76	0.33	2.4	0.96	0.048 ±0.003	3.4±0.3	5.6±0.3
100.6	Methanol	15.9±0.6	65±1	0.20±0.01	1.4	1.23±0.13	na[d]	0.16±0.02	0 [c]

a. The fuel surface temperature for the liquid pool fires is near the fuel boiling point [38, 46, 47]. Measurements at the pool surface [38, 46] also show that the temperature for the liquid fuels slowly increase on the order of 2 °C/hr. See discussion below.
b. below detection limit (< 10^{-4}).
c. soot was not observed at any fire location.
d. "na" is not available.

Flame height and Puffing frequency: The flame appearance was recorded and analyzed to determine flame heights as a function of time by image processing. The flame puffing frequency was estimated using video recordings or temperature measurements and fast Fourier transform analysis. As expected, the puffing frequency did not differ much from fire to fire in Table 13,

ranging from 2.2 Hz to 2.5 Hz in the liquid and gaseous fuel fires. The normalized flame height varied from 1.2 to 4.4, which roughly followed Eq. (1) in Section 2.3.

CO and Soot yields: The concentration of carbon monoxide (CO) in the exhaust duct was determined via extractive sampling and non-dispersive infrared (NDIR) measurements. Table 13 shows the CO yield varied from near zero to 1 %, depending on the fire. The soot mass fraction was measured in the duct using He-Ne laser transmission, and the soot yield varied from below detection limits to about 2%, depending on the fire. The soot yield was less than the CO yield for the acetone and the 20 kW propane fires, otherwise, it was larger than the CO yield.

Radiative faction: A single location radiative heat flux measurement was used to determine the radiative fraction. The results were favorably compared to previous measurements using multi-location and single-location heat flux measurements. As seen in Table 13, the radiative fraction varied from 21 % in the methane fire to 35 % in the heptane fire.

Total heat feedback to the pool surface: The total heat feedback to the burner surface in the gaseous fuel fires was estimated by using the water-cooled burner as a calorimeter. For completeness, the total heat feedback for the burning liquid fuels is calculated from detailed local heat flux measurements or reproduced from previous work [8, 11]. As seen in Table 13, the heat feedback normalized by the idealized heat release rate differed widely from fire to fire – varying from 1 % for the heptane fire to 13 % for the 20 kW propane fire. The heat feedback is due to several factors, including the fire size, the mass burning rate of the fuel, and the effect of *"blowing"* on the convective heat transfer to the pool surface.

Local measurements

Gas velocity: The upward velocity and the gas phase temperature were measured along the centerline in the flame and plume regions of medium-scale pool fires. Time-averaged local measurements of the upward velocity were conducted using a bidirectional probe in the plumes of the liquid and gaseous fuel fires. The upward component of the velocity on the plume centerline in the pool fires compared favorably to previous measurements. The results showed that the upward velocity increased with distance above the plume for about 1 to 2 diameters above the fuel surface and then decreased with distance, which followed the general trends of Baum and McCaffrey's plume theory.

Gas temperature: The gas-phase temperatures were measured using fine-wire, bare-bead thermocouples with nearly spherical beads of various diameters. The gas-phase thermocouple temperatures were corrected considering radiative loss and thermal inertia effects. The corrected profiles of mean axial temperature in the methanol, ethanol and acetone fires were similar to previous results when scaled by $\dot{Q}^{2/5}$.

Local heat flux distribution: The local heat flux distribution in the radial and downward direction was measured to estimate the radiative heat flux through a virtual cylinder surrounding the fire. The heat flux in the radial direction typically obtained a maximum at about 10 cm to 20 cm above the fuel surface and then decreased. The heat flux in the downward direction decreased with radial distance from the fire approximately following the form: $\dot{q}'' \sim r^{-2}$. Results from previous studies are reported, which show that for all liquid fuel pool fires, the local total heat flux onto the fuel surface monotonically decreased with distance from the pool center until about 12 cm to 13 cm from the burner edge, where the flux continued to decrease for the methanol and ethanol pool fires but increased for the acetone and heptane pool fires. These results exemplify the complex dynamic structure of the fires particularly near the burner edge where the fire is anchored and where nodes and channels are formed.

Fuel temperature:

- Liquid Fuels: The liquid fuel surface and in-depth temperature were measured using thermocouples. The fuel surface temperature in the liquid fuels was observed to be approximately equal to the fuel boiling point. After long burning times (~2000 s to 3000 s), the liquid fuel surface temperatures were observed to slowly increase 1 ℃ to 3 ℃. This phenomenon may be due to the back diffusion of combustion products (such as water) in the gas phase, condensing on the liquid pool surface and changing its composition and thereby its boiling point.
- Gaseous Fuels: The porous metal burner surface temperature for fires burning gaseous fuels studied here was about 60℃. Qualitative observations showed that this value was dependent on the water flow rate used to cool the burner.

Summary:

This report presents new measurements alongside previous data from previous studies to offer a comprehensive overview of steadily burning pool fires. Complementary information on the local, detailed chemical structure of these fires is available in Ref.[1]. Analogous measurements characterizing a 1 m diameter methanol pool fire are found in Ref. [24]. In total, the measurement results provide a comprehensive data set for the evaluation of computational fire models and offer insight on the complex structure of medium-scale pool fires burning a variety of fuel types. The measurements and their uncertainty help establish a data repository for use in the rigorous evaluation of computational fluid dynamics fire models.

5. References

[1] Falkenstein-Smith, R., Sung, K., Chen, J., Harris, K. and Hamins, A., *The Structure of Medium-Scale Pool Fires*, NIST Technical Note 2082e2, National Institute of Standards and Technology, Gaithersburg, MD, February 2022, https://doi.org/10.6028/NIST.TN.2082e2.

[2] McGrattan, K., Hostikka, S., Floyd, J., McDermott, R. and Vanella, M., *Fire Dynamics Simulator Technical Reference Guide Volume 3: Validation*, NIST special publication 1018-3, Sixth Ed., National Institute of Standards and Technology, Gaithersburg, MD, March 2020, http://dx.doi.org/10.6028/NIST.SP.1018.

[3] Brown, A., Bruns, M., Gollner, M., Hewson, J., Maragkos, G., Marshall, A., McDermott, R., Merci, B., Rogaume, T., Stoliarov, S., Torero, J., Trouvé, A., Wang, Y. and Weckman, E., Proceedings of the First Workshop Organized by the IAFSS Working Group on Measurement and Computation of Fire Phenomena (MaCFP), *Fire Safety Journal*, ***101***, 1-17, (2018), https://doi.org/10.1016/j.firesaf.2018.08.009.

[4] Merci, B. and Trouvé, A., Call for Participation in the Second Workshop Organized by the IAFSS Working Group on Measurement and Computation of Fire Phenomena, *Fire Technology*, ***55***, 1911-1917, (2019), https://doi.org/10.1007/s10694-019-00844-6.

[5] Corlett, R. and Fu, T., Some Recent Experiments with Pool Fires, *Pyrodynamics*, ***1***, 253-269, (1966).

[6] Weckman, E. J. and Sobiesiak, A., The Oscillatory Behaviour of Medium-Scale Pool Fires, *Proceedings of the Combustion Institute*, ***22***, 1299-1310, (1989), https://dx.doi.org/10.1016/s0082-0784(89)80141-9.

[7] Weckman, E. J. and Strong, A. B., Experimental Investigation of the Turbulence Structure of Medium-Scale Methanol Pool Fires, *Combustion and Flame*, ***105***, 245-266, (1996), https://doi.org/10.1016/0010-2180(95)00103-4.

[8] Hamins, A., Fischer, S. J., Kashiwagi, T., Klassen, M. E. and Gore, J. P., Heat Feedback to the Fuel Surface in Pool Fires, *Combustion Science and Technology*, ***97***, 37-62, (1994), https://doi.org/10.1080/00102209408935367.

[9] Klassen, M. and Gore, J., *Structure and Radiation Properties of Pool Fires*, NIST-GCR-94-651, National Institute of Standards and Technology, Gaithersburg, MD, June 1994, https://ntrl.ntis.gov/NTRL/dashboard/searchResults/titleDetail/PB94193802.xhtml.

[10] Hogben, C. D. A., Young, C. N., Weckman, E. J. and Strong, A. B., Radiative Properties of Acetone Pool Fires, in *33rd ASME National Heat Transfer Conference*, Albuquerque, pp12, (1999).

[11] Kim, S. C., Lee, K. Y. and Hamins, A., Energy Balance in Medium-Scale Methanol, Ethanol, and Acetone Pool Fires, *Fire Safety Journal*, ***107***, 44-53, (2019), https://doi.org/10.1016/j.firesaf.2019.01.004.

[12] Papadopoulos, G., Bryant, R. and Pitts, W., Flow Characterization of Flickering Methane/Air Diffusion Flames Using Particle Image Velocimetry, *Experiments in Fluids*, ***33***, 472-481, (2002), https://doi.org/10.1007/s00348-002-0483-y.

[13] Tieszen, S. R., O'Hern, T. J., Schefer, R. W., Weckman, E. J. and Blanchat, T. K., Experimental Study of the Flow Field in and around a One Meter Diameter Methane Fire, *Combustion and Flame*, ***129***, 378-391, (2002), https://dx.doi.org/10.1016/s0010-2180(02)00352-8.

[14] Devaud, C. B., Weisinger, J., Johnson, D. A. and Weckman, E. J., Experimental and Numerical Characterization of the Flowfield in the Large-Scale Uw Live Fire Research Facility, *International Journal for Numerical Methods in Fluids*, ***60***, 539-564, (2009), https://doi.org/10.1002/fld.1906.

[15] Welle, E. J., Roberts, W. L., Decroix, M. E., Carter, C. D. and Donbar, J. M., Simultaneous Particle-Imaging Velocimetry and Oh Planar Laser-Induced Fluorescence Measurements in an Unsteady Counterflow Propane/Air Diffusion Flame, *Proceedings of the Combustion Institute*, ***28***, 2021-2027, (2000), https://doi.org/10.1016/S0082-0784(00)80609-8.

[16] Bouvier, M., Cabot, G., Yon, J. and Grisch, F., On the Use of PIV, LII, PAH-PLIF and OH-PLIF for the Study of Soot Formation and Flame Structure in a Swirl Stratified Premixed Ethylene/Air Flame, *Proceedings of the Combustion Institute*, (2020), https://doi.org/10.1016/j.proci.2020.10.002.

[17] McCaffrey, B. J. and Heskestad, G., A Robust Bidirectional Low-Velocity Probe for Flame and Fire Application, *Combustion and Flame*, ***26***, 125-127, (1976), https://doi.org/10.1016/0010-2180(76)90062-6.

[18] McCaffrey, B. J., *Purely Buoyant Diffusion Flames: Some Experimental Results*, NBSIR 79-1910, National Bureau of Standards, Washington, D.C. 20234, October 1979, https://nvlpubs.nist.gov/nistpubs/Legacy/IR/nbsir79-1910.pdf.

[19] Hamins, A. (1985). *The Structure and Extinction of Diffusion Flames.* (Ph.D.). University of Califonia at San Diego.

[20] Hamins, A. and Lock, A., *The Structure of a Moderate-Scale Methanol Pool Fire*, NIST Technical Note 1928, National Institute of Standards and Technology, Gaithersburg, MD, November 2016, https://doi.org/10.6028/NIST.TN.1928.

[21] Otsu, N., A Threshold Selection Method from Gray-Level Histograms, *IEEE transactions on systems, man, and cybernetics*, ***9***, 62-66, (1979), http://doi.org/10.1109/TSMC.1979.4310076.

[22] Heskestad, G., Luminous Heights of Turbulent Diffusion Flames, *Fire Safety Journal*, ***5***, 103-108, (1983), https://doi.org/10.1016/0379-7112(83)90002-4.

[23] Falkenstein-Smith, R. L., Sung, K. and Hamins, A., Characterization of Medium-Scale Propane Pool Fires, *Fire Technology*, ***59***, 1865-1882, (2023), https://dx.doi.org/10.1007/s10694-023-01412-9.

[24] Sung, K., Chen, J., Bundy, M., Fernandez, M. and Hamins, A., *The Thermal Character of a 1 m Methanol Pool Fire*, NIST Technical Note 2083, Rev.1, National Institute of Standards and Technology, Gaithersburg, MD, June 2021, https://doi.org/10.6028/NIST.TN.2083r1.

[25] Grosshandler, W. L., *RADCAL: A Narrow-Band Model for Radiation Calculations in a Combustion Environment*, NIST Technical Note 1402, National Institute of Standards and Technology, Gaithersburg, MD, April 1993, https://nvlpubs.nist.gov/nistpubs/Legacy/TN/nbstechnicalnote1402.pdf.

[26] Ranz, W. and Marshall, W., Evaporation from Drops, *Chem. eng. prog*, ***48***, 141-146, (1952).

[27] Çengel, Y. A. and Ghajar, A. J., Heat and Mass Transfer: Fundamentals and Applications, 7th Ed., McGraw-Hill Education, 2020.

[28] Shaddix, C. R., Correcting Thermocouple Measurements for Radiation Loss: A Critical Review, American Society of Mechanical Engineers, New York, NY (US); Sandia National Labs., Livermore, CA (US), 1999. https://www.osti.gov/etdeweb/biblio/20002672

[29] Jaeger, F. M. and Rosenbohm, E., The Exact Formulae for the True and Mean Specific Heats of Platinum between 0° and 1600℃, *Physica*, ***6***, 1123-1125, (1939), https://doi.org/10.1016/S0031-8914(39)90111-4.

[30] Modak, A. T., Thermal Radiation from Pool Fires, *Combustion and Flame*, ***29***, 177-192, (1977), https://doi.org/10.1016/0010-2180(77)90106-7.

[31] Hamins, A., *Energetics of Small and Moderate-Scale Gaseous Pool Fires*, NIST Technical Note 1926, National Institute of Standards and Technology, Gaithersburg, MD, November 2016, https://doi.org/10.6028/NIST.TN.1926.

[32] Design Institute for Physical Properties (DIPPR 801), American Institute of Chemical Engineers, 2017. https://www.aiche.org/dippr

[33] Hamins, A., Yang, J. C. and Kashiwagi, T., An Experimental Investigation of the Pulsation Frequency of Flames, *Symposium (International) on Combustion*, ***24***, 1695-1702, (1992), https://doi.org/10.1016/S0082-0784(06)80198-0.

[34] Zukoski, E. E., Properties of Fire Plumes, In: Combustion Fundeamentals of Fire (Ed. G. Cox), Academic Press, London, (1995).

[35] Bryant, R. A. and Bundy, M. F., *The NIST 20 MW Calorimetry Measurement System for Large-Fire Research*, NIST Technical Note 2077, National Institute of Standards and Technology, Gaithersburg, MD, December 2019, https://doi.org/10.6028/NIST.TN.2077.

[36] Mulholland, G. W., Johnsson, E. L., Fernandez, M. G. and Shear, D. A., Design and Testing of a New Smoke Concentration Meter, *Fire and Materials*, ***24***, 231-243, (2000), https://onlinelibrary.wiley.com/doi/abs/10.1002/1099-1018%28200009/10%2924%3A5%3C231%3A%3AAID-FAM743%3E3.0.CO%3B2-N

[37] Mulholland, G. W. and Croarkin, C., Specific Extinction Coefficient of Flame Generated Smoke, *Fire and Materials*, ***24***, 227-230, (2000), https://doi.org/10.1002/1099-1018(200009/10)24:5%3C227::AID-FAM742%3E3.0.CO;2-9

[38] Sung, K., Chen, J., Bundy, M. and Hamins, A., The Characteristics of a 1 m Methanol Pool Fire, *Fire Safety Journal*, ***120***, 103121, (2021), https://doi.org/10.1016/j.firesaf.2020.103121.

[39] Hamins, A., MaCFP Github Website accesed on 01/24/2024; https://raw.githubusercontent.com/MaCFP/macfp-db/master/Liquid_Pool_Fires/NIST_Pool_Fires/Experimental_Data/Methanol_30_cm_TC_r%3D0_Hamins_2016.csv

[40] Fischer, S. J., Hardouin-Duparc, B. and Grosshandler, W. L., The Structure and Radiation of an Ethanol Pool Fire, *Combustion and Flame*, ***70***, 291-306, (1987), https://doi.org/10.1016/0010-2180(87)90110-6.

[41] Weckman, E. J., MaCFP Github Website accesed on 11/14/2023; https://github.com/MaCFP/macfp-db/blob/master/Liquid_Pool_Fires/Waterloo_Acetone/Experimental_data/test1_mean_and_rms_r0cm.csv

[42] Baum, H. R. and McCaffrey, B. J., Fire Induced Flow Field-Theory and Experiment, in *Proceedings of the Second International Symposium on Fire Safety Science*, Hemisphere, New York, ***2***, pp129-148, (1989). https://publications.iafss.org/publications/fss/2/129

[43] Heskestad, G., SFPE Handbook of Fire Protection Engineering, 5th edition, Socierty of Fire Protection Engineers, Springer, 2016, https://www.sfpe.org/publications/handbooks/sfpehandbook.

[44] Hamins, A., Klassen, M., Gore, J. and Kashiwagi, T., Estimate of Flame Radiance via a Single Location Measurement in Liquid Pool Fires, *Combustion and Flame*, ***86***, 223-228, (1991), https://doi.org/10.1016/0010-2180(91)90102-H.

[45] Buch, R., Hamins, A., Konishi, K., Mattingly, D. and Kashiwagi, T., Radiative Emission Fraction of Pool Fires Burning Silicone Fluids, *Combustion and Flame*, ***108***, 118-126, (1997), https://doi.org/10.1016/S0010-2180(96)00098-3.

[46] Sung, K., Falkenstein-Smith, R. and Hamins, A., *Velocity and Temperature Structure of Medium-Scale Pool Fires*, NIST Technical Note 2162, National Institute of Standards and Technology, Gaithersburg, MD, 2021-06-22 2021, https://nvlpubs.nist.gov/nistpubs/TechnicalNotes/NIST.TN.2162.pdf ; see also Sung, K., Falkenstein-Smith, R. and Hamins, A., The Global and Local Structure of Medium-Scale Pool Fires, NIST Technical Note 2162 Rev.1, National Institute of Standards and Technology, Gaithersburg, MD, 2024, https://10.6028/NIST.TN.2162r1.

[47] Donald R. Burgess, J. and Hamins, A., *Heats of Combustion and Related Properties of Pure Substances*, NIST Technical Note 2126, National Institute of Standards and Technology, Gaithersburg, MD, December 5 2023, https://doi.org/10.6028/NIST.TN.2126; also to appear in the Appendix of the SFPE Handbook of Fire Protection Engineering, 6th Ed.

[48] NIST REFPROP Database Version 9.1 (2013) accesed on 11/15/2023; https://www.nist.gov/programs-projects/reference-fluid-thermodynamic-and-transport-properties-database-refprop

[49] National Instruments Inc., *SCXI-1600 User Manual and Specifications*, 2004.

[50] Taylor, B. N. and Kuyatt, C. E., *Guidelines for Evaluating and Expressing the Uncertainty of NIST Measurement Results*, NIST Technical Note 1297, National Institute of Standards and Technology, Gaithersburg, MD, September 1994. https://www.nist.gov/pml/nist-technical-note-1297

[51] Pitts, W. M., Murthy, A. V., De Ris, J. L., Filtz, J.-R., Nygård, K., Smith, D. and Wetterlund, I., Round Robin Study of Total Heat Flux Gauge Calibration at Fire Laboratories, *Fire Safety Journal*, ***41***, 459-475, (2006), https://dx.doi.org/10.1016/j.firesaf.2006.04.004.

[52] Bryant, R., Johnsson, E., Ohlemiller, T. and Womeldorf, C., Estimates of the Uncertainty of Radiative Heat Flux Calculated from Total Heat Flux Measurements, in *Proc. 9th Interflam Conference in Edinburgh, Interscience Communications London*, pp 605-616, (2001).

[53] Falkenstein-Smith, R., Sung, K., Chen, J. and Hamins, A., Chemical Structure of Medium-Scale Liquid Pool Fires, *Fire Safety Journal*, ***120***, 103099, (2021), https://doi.org/10.1016/j.firesaf.2020.103099.

[54] Weckman, E. J., Personal Communication, Email to A. Hamins, 28 August 2020.

[55] Wang, Z., Tam, W. C., Chen, J., Lee, K. Y. and Hamins, A., Thin Filament Pyrometry Field Measurements in a Medium-Scale Pool Fire, *Fire Technology*, ***56***, 837-861, (2020), https://10.1007/s10694-019-00906-9.

[56] Akita, K. and Yumoto, T., Heat Transfer in Small Pools and Rates of Burning of Liquid Methanol, *Proceedings of the Combustion Institute*, ***10***, 943-948, (1965).

[57] Yilmaz, A., *Radiation Transport Measurements in Methanol Pool Fires with Fourier Transform Infrared Spectroscopy*, NIST Grant/Contractor Report GCR 09-922, January 2009. https://www.nist.gov/publications/radiation-transport-measurements-methanol-pool-fires-fourier-transform-infrared

[58] Chen, J., Personal Communication, Email to A. Hamins, 29 August 2021.

[59] Hamins, A., Konishi, K., Borthwick, P. and Kashiwagi, T., Global Properties of Gaseous Pool Fires, *Symposium (International) on Combustion*, ***26***, 1429-1436, (1996), https://doi.org/10.1016/S0082-0784(96)80363-8.

Appendix A. Thermophysical Properties

Table A1. Thermochemical properties of liquid and gaseous fuels at 20 ºC [32].

Fuel	Chemical Formula	Density [*] [kg/m^3]	MW [g/mol]	Boiling Temperature [ºC]	ΔH_c [kJ/g]
Methanol	CH_3OH	791.01	32.04	64.7 ± 0.1	19.90
Ethanol	C_2H_6O	789.67	46.07	78.3 ± 0.5	26.82
Acetone	C_3H_6O	790.27	58.08	56.1 ± 0.3	28.52
Heptane	C_7H_{16}	683.82	100.20	98.4 ± 0.1	44.56
Methane	CH_4	0.6682	16.04	-161.6 ± 0.01	50.03
Propane	C_3H_8	1.8650	44.10	-42.2 ± 0.01	46.33

* Ref. [48]

Table A2. Thermophysical properties of platinum as a function of temperature.

Temperature [℃]	Specific heat [J/g-℃] [a]	Emissivity [-] [b]
100	0.14	0.00
200	0.14	0.03
300	0.14	0.05
400	0.14	0.07
500	0.15	0.09
600	0.15	0.10
700	0.15	0.12
800	0.15	0.13
900	0.16	0.14
1000	0.16	0.15
1100	0.16	0.17
1200	0.16	0.18
1300	0.17	0.19
1400	0.17	0.19

[a] Ref. [29]

[b] Ref. [28]

Polynomial fits for the temperature (℃) dependent specific heat $(c_{p,b})$ and emissivity (ϵ_b) of platinum:

$$c_{p,b} = 0.13 + 2.56(T - 273)$$
$$\epsilon_b = -0.1 + 3.24 \cdot 10^{-4}(T - 273) - 1.25 \cdot 10^{-7}(T - 273)^2 + 2.18 \cdot 10^{-11}(T - 273)^3 \quad \text{(A1)}$$

Table A3. Thermophysical properties of air as a function of temperature [27].

Temperature [ºC]	Density [kg/m³]	Specific Heat [J/kg-℃]	Thermal Conductivity [W/m-℃]	Dynamic Viscosity [kg/m-s]	Prandtl Number [-]
300	0.616	1044	0.044	2.93E-05	0.694
350	0.566	1056	0.047	3.10E-05	0.694
400	0.524	1069	0.050	3.26E-05	0.695
450	0.488	1081	0.053	3.42E-05	0.697
500	0.457	1093	0.056	3.56E-05	0.699
600	0.404	1115	0.061	3.85E-05	0.704
700	0.363	1135	0.066	4.11E-05	0.709
800	0.329	1153	0.070	4.36E-05	0.715
900	0.301	1169	0.075	4.60E-05	0.721
1000	0.277	1184	0.079	4.83E-05	0.726
1500	0.199	1234	0.096	5.82E-05	0.748
2000	0.155	1264	0.111	6.63E-05	0.754

Polynomial fits for the temperature (℃) dependent density (ρ), specific heat (c_p), thermal conductivity (λ), and dynamic viscosity (μ) of the air yield the following:

$$\rho = 351.90(T + 273.15)^{-1}$$

$$c_p = 948.38 + 0.36T - 1.43\text{E-}4 \cdot T^2 + 2.20\text{E-}8 \cdot T^3$$

$$\lambda = 0.024 + 7.56\text{E-}5 \cdot T - 2.52\text{E-}8 \cdot T^2 + 4.64\text{E-}12 \cdot T^3 \quad \text{(A2)}$$

$$\mu = 1.74\text{E-}5 + 4.463\text{E-}8 \cdot T - 2.40\text{E-}11 \cdot T^3 + 1.05\text{E-}14 \cdot T^3 - 1.99\text{E-}18 \cdot T^4$$

Appendix B. Pressure Transducer Information

Table B1. Calibration factor and response time of the pressure transducers.

Pressure Transducer	Maximum Pressure Range [kPa]	Calibration Factor [Pa/V]	Response time [a] τ_p [ms]
Setra-717	0.025	10.225	113 ± 9
Setra-568	0.25	101.764	192 ± 9
MKS-220D	0.13	13.333	270 ± 6
MKS-226A	0.027	2.742	21 ± 1

a. The response time of the pressure transducer (τ_p) is defined as the amount of time it takes for the output signal to reach 63.2 % of the actual pressure change from when the input changes occur. Response time measurements were repeated three times using a data acquisition system (DAQ, Model: SCXI-1600, National Instrument Inc) at a sampling rate of 10 Hz.

The combined standard (k=1) uncertainty of the response time of the pressure transducer, $u_c(\tau_p)$, is estimated as:

$$u_c(\tau_p) = \sqrt{\sigma_R(\tau_p)^2 + u_c(PT)^2 + u_c(DAQ)^2} \quad \text{(B1)}$$

where $\sigma_R(\tau_p)$ is the repeatability defined by taking the standard deviation of the repeat measurements. $u_c(PT)$ and $u_c(DAQ)$ indicate the measurement accuracy of the pressure transducer and the DAQ. According to its specifications, $u_c(PT)$ and $u_c(DAQ)$ are 1.0 % and 0.076 % [49] in the application range of interest, respectively. Figure B1 shows the voltage signal of the pressure transducer (Setra-717) as a function of time after an input change occurs. The response time is 113 ms. The uncertainty, $u_c(\tau_p)$, is 2.5 %, averaged over all four pressure transducers used in this study.

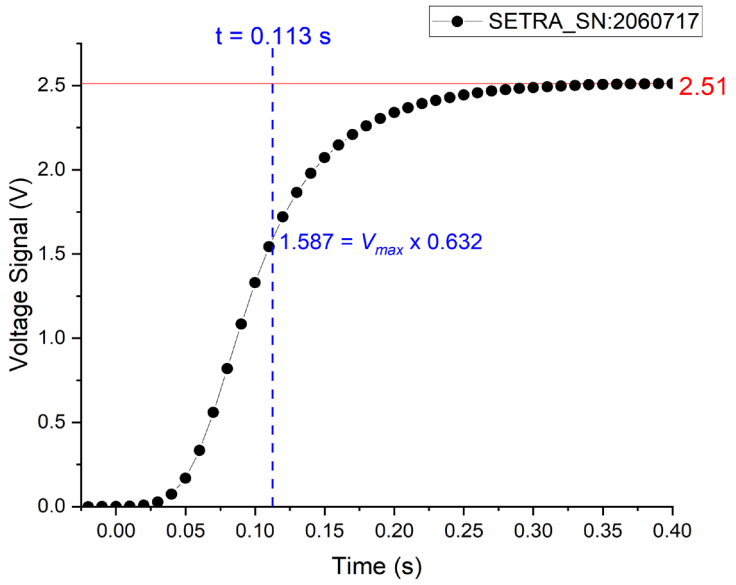

Fig. B1. Voltage signal of a pressure transducer (Setra-717) as a function of time after an instantaneous pressure change.

Appendix C. Thermocouple Information

A number of different thermocouples were used in the experiments. They are listed in Table C1 by their type, and the wire and bead diameters. All the beads were approximately spherical. Table C2 lists the thermocouple number, type, sampling location range (z, r), and the data acquisition rate (f_s) which varied from 60 Hz to 1 kHz.

Table C1. Thermocouple type, and wire and bead diameters.

Thermocouple No.	Type	Wire diameter d_w [µm]	Bead diameter d_b [µm]
TC 1	S	25	199
TC 2	S	12.5	52.1
TC 3	S	25	119
TC 4	R	25	102.7
TC 5	S	25	125
TC 6	S	50	150
TC 7	S	12.5	38.8

Table C2. Summary of the data acquisition sampling rate (f_s), temperature measurement positions and thermocouple number and type used in the experiments.

Fuel	Thermocouple Number†	Thermocouple Type	z [cm]	r [cm]	f_s [Hz]
Acetone	5*	S	3 to 131	0	250
Acetone	3	R	3 to 61	0	120
Acetone	4	S	3 to 101	0	250
Ethanol	5*	S	3 to 101	0	250
Ethanol	1	S	2 to 61	0	250
Heptane	5*	S	33 to 141	0	250
Methanol	5*	S	4 to 113	0	250
Methanol	2	S	0 to 111	0	1000
Methanol	1	S	2 to 61	0	250
Methanol	6	S	41 to 61	-5 to 18	60
Methane	5*	S	4 to 10	0	200
Methane	5*	S	20 to 88	0	20
Methane	3	R	1 to 75	0	1000
Methane	2	S	1 to 60	0	1000
Propane, 20 kW	7	S	2 to 100	0	1000
Propane, 34 kW	5*	S	4 to 75	0	200
Propane, 34 kW	5*	S	100 to 115	0	500
Propane, 34 kW	7*	S	2 to 125	0	1000
Propane, 34 kW	7	S	2 to 60	0	1000
Propane, 50 kW	7*	S	2 to 75	0	1000
Propane, 50 kW	7	S	2 to 150	0	1000

†Additional information on each of the thermocouples, including wire and bead diameter, can be found in Table C1.

*The thermocouple was positioned about 5 mm upstream of the leading edge of the bidirectional probe and offset about 2 mm from the outer edge of the probe.

**z is the axial distance from the fuel surface.

Appendix D. Effect of Bidirectional Probe on Temperature Measurements

To calculate the temperature-dependent gas properties in Eqs. 4 - 6, time series temperature measurements were conducted using a Type S, 25 µm wire diameter, bare -bead, thermocouple (TC5) positioned 5 mm upstream of the bidirectional probe (see Figure 6 in *Section 2.5*).

The thermocouple position was based on being as close to the probe as practical while preventing damage to the fine thermocouple by the fire, which tended to move the thermocouple downstream towards the bidirectional probe when inserted into the upward-

moving fire plume. In this section, the mean of the thermocouple bead temperature with and without a bidirectional probe at the same measurement positions were compared to understand the effect of the presence of the bidirectional probe on the temperature measurement results.

Table D1 shows the mean gas temperatures measured using thermocouples without the bidirectional probe ($T_{g,alone}$) present and with the thermocouple positioned below the bidirectional probe ($T_{g,TC5}$) in the methanol, acetone and ethanol pool fires. The relative difference of the measurements: ($|\overline{T}_{g,TC5} - \overline{T}_{g,alone}|/\overline{T}_{g,alone}$), referred to here as the *deviation*, is compared to the expanded (k=2) combined uncertainty of the mean gas temperature measured using thermocouples without the bidirectional probe ($U_c(T_{g,alone})$) present. The *deviation* is 4 % on-average, which is much less than the mean of the expanded (k=2) combined uncertainty of the mean gas temperature measured using thermocouples in the absence of the bidirectional probe. This indicates that the bidirectional probe has little influence on the gas temperature measurement.

Table D1. The mean thermocouple gas temperature measured in the presence ($T_{g,TC5}$) and absence ($T_{g,alone}$) of the bidirectional probe in the methanol, acetone and ethanol pool fires. The *deviation* of the mean gas temperature at each position is compared to the expanded (k=2) combined uncertainty of the mean gas thermocouple temperature without the bidirectional probe present ($U_c(T_{g,alone})$).

Fuel	z [cm]	$\overline{T}_{g,alone}$ [K]	$\overline{T}_{g,TC5}$ [K]	$U_c(\overline{T}_{g,alone})$ [%]	Deviation of $\overline{T}_g$ [%]
Acetone	3	702	653	35 %	7 %
Acetone	7	910	894	24 %	2 %
Acetone	11	1079	1066	13 %	1 %
Acetone	15	1200	1148	2 %	4 %
Acetone	21	1232	1187	9 %	4 %
Acetone	41	1142	1072	29 %	6 %
Acetone	46	1081	1034	14 %	4 %
Acetone	51	1048	1007	39 %	4 %
Acetone	61	918	890	22 %	3 %
Ethanol	3	969	933	7 %	4 %
Ethanol	5	1132	1109	4 %	2 %
Ethanol	7	1206	1221	6 %	1 %
Ethanol	11	1281	1260	3 %	2 %
Ethanol	15	1291	1265	5 %	2 %
Ethanol	21	1261	1217	5 %	3 %

----- Table D1 **Continued on Next Page** -----

Fuel	z [cm]	$\overline{T}_{g,alone}$ [K]	$\overline{T}_{g,TC5}$ [K]	$U_c(\overline{T}_{g,alone})$ [%]	Deviation of $\overline{T}_g$ [%]
Ethanol	31	1097	984	5 %	10 %
Ethanol	46	813	759	3 %	7 %
Ethanol	61	615	598	3 %	3 %
Methanol	4	1183	1236	2 %	4 %
Methanol	6	1251	1316	5 %	5 %
Average				12 %	4 %

Appendix E. Flame Height Correction for Parallax

The video-recorded flame can be distorted due to parallax, depending on the view angle formed between the target and the relative camera location. Figure E1 shows diagrams of the video-recorded flame height (d') relative to the actual flame height (d) for a video camera located at (x, y) from the center of the pool surface. The video-recorded flame height (d') is esimated as:

$$d' = 2\left(s \cdot \sin\frac{\theta}{2}\right) \tag{E1}$$

where s is the distance from the camera to the tip of the recorded flame. θ is the angle of view formed by the video-recorded flame height. The compensation method is divided into three cases, considering the actual flame height (d) and the camera location (x, y) seen in Fig. E1. The quantities s and θ in each case are given in Table E1. The actual flame height (d) is estimated as:

$$d = C(x, y, d') \times d' \tag{E2}$$

where $C(x, y, d')$ is the correction factor for parallax, defined here as (d/d')

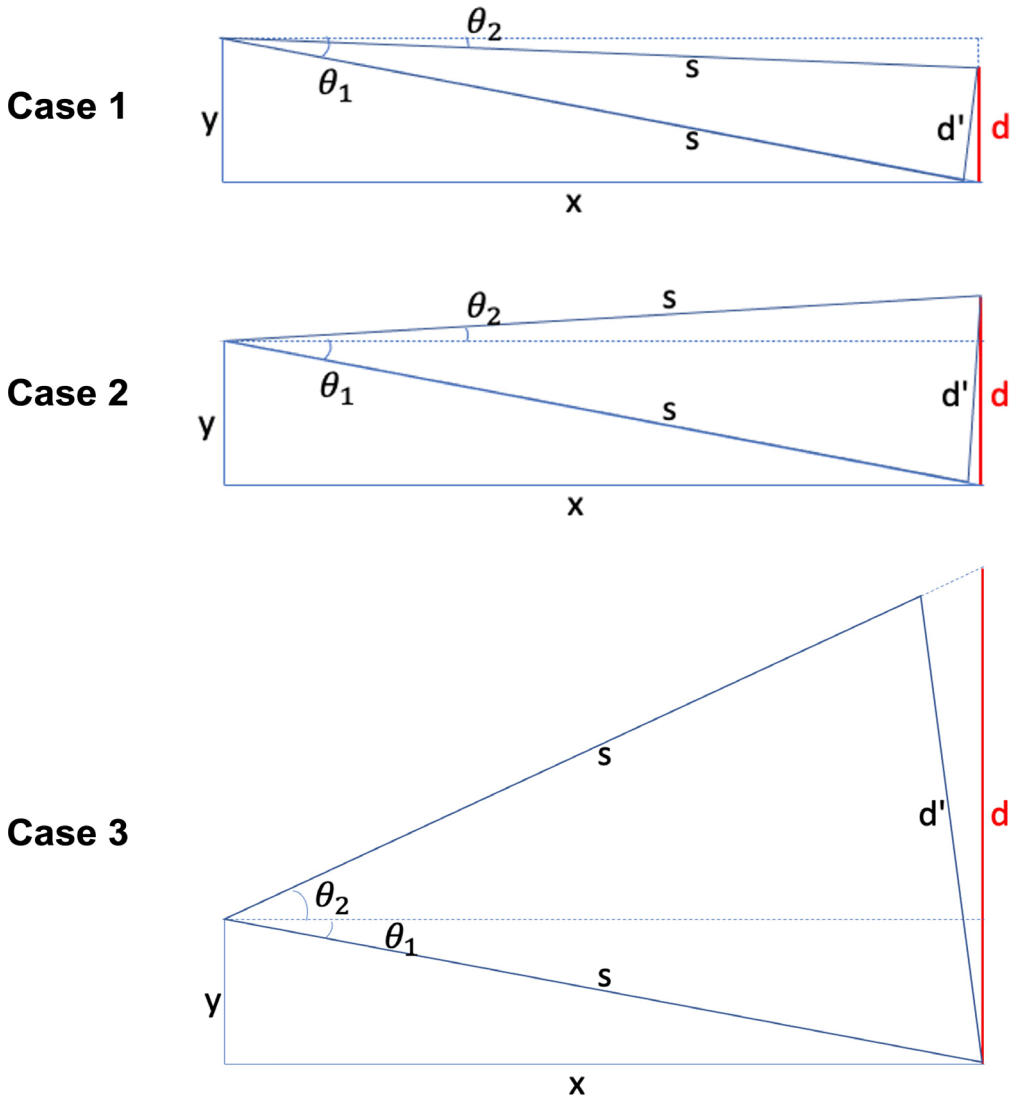

Fig. E1. Diagrams of the video-recorded flame height (d') relative to the actual flame height (*d*) for a video camera located at (*x, y*) from the center of the pool surface.

Table E1. Definition of parameters in Eqs E1 – E2 for estimating the flame height.

Case no.	Region	θ_1 [rad]	θ_2 [rad]	θ [rad]	s [cm]
1	$d < y$	$\text{atan}\left(\frac{y}{x}\right)$	$\text{atan}\left(\frac{y-d}{x}\right)$	$\theta_1 - \theta_2$	$\sqrt{x^2+(y-d)^2}$
2	$y \le d \le 2y$	$\text{atan}\left(\frac{y}{x}\right)$	$\text{atan}\left(\frac{d-y}{x}\right)$	$\theta_1 + \theta_2$	$\sqrt{x^2+(d-y)^2}$
3	$2y < d$	$\text{atan}\left(\frac{y}{x}\right)$	$\text{atan}\left(\frac{d-y}{x}\right)$	$\theta_1 + \theta_2$	$\sqrt{x^2+y^2}$

A video camera was located at $(x, z) = (216.5cm, 52cm)$ from the center of the pool surface in the experiments. Figure E2 shows the ratio of the actual flame height to the video-recorded flame height, (d/d') as a function of the video-recorded flame height (d'). The video-recorded flame height is equal to the actual flame height when the actual flame height is two times the camera height (y) and when the camera was focused on the center of the actual flame. On the other hand, the ratio (d/d') is less than 1 at the actual flame height. The recorded flame height is about 17 % smaller when the actual flame height is 2 m.

A piecewise fit was used to estimate the correction factor (C) as function of d'. The fitting results are compared with the original dataset in Fig. E2. The flame height in each video frame was corrected for image distortion error (parallax) using the fit functions with Eq. E2.

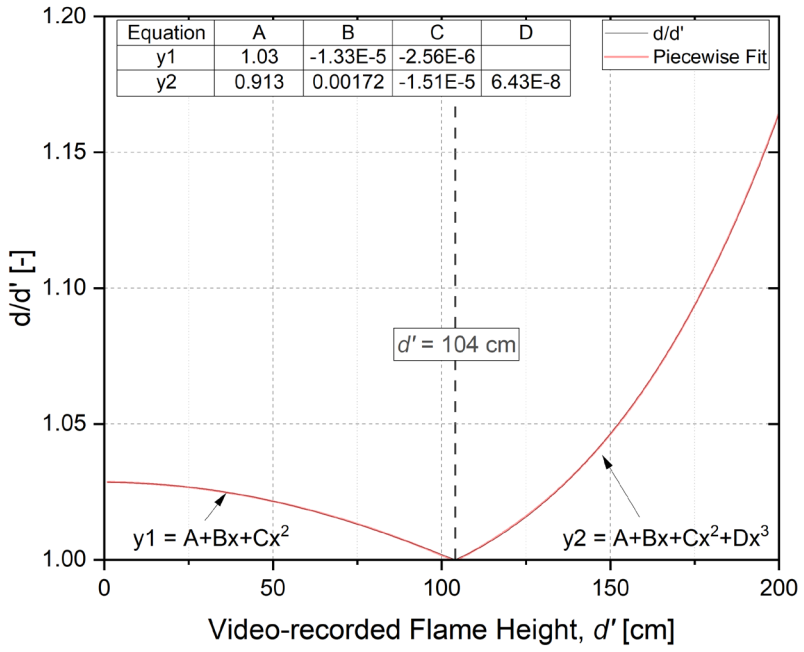

Fig. E2. The ratio of the actual flame height (d) to the video-recorded flame height (d') as a function of the video-recorded flame height where the camera is located at $(x, y) = (216.5\ cm, 52\ cm)$ (see diagram in Figure E1). The piecewise fitting line is also shown.

Appendix F. Uncertainty Analyses

Estimates of uncertainty are evaluated using the method described in Ref. [50]. A series of measurements, denoted by y, can be expressed as a function of its associated independent variables, x_i. The function f in Eq. F1 contains all quantities that significantly contribute to the measurement:

$$y = f(x_1, x_2, x_3, \cdots, x_N) \tag{F1}$$

In the case that all input parameters are uncorrelated, the combined standard uncertainty is given by Eq. F2, referred to as *the law of propagation of uncertainty*.

$$u_c(y) = \sqrt{\sum_{i=1}^{N} \left(s_i \cdot u(x_i)\right)^2} \tag{F2}$$

where $u_c(y)$ is the combined standard uncertainty and $u(x_i)$ is the standard uncertainty of each input parameter. The parameter, s_i, is the non-dimensional sensitivity coefficient, defined as:

$$s_i = \frac{\partial f}{\partial x_i}\frac{x_i}{y} \tag{F3}$$

A series of measurements allows computation of statistics of their uncertainties during steady burning, and the standard deviation of the output estimate, σ_y, is considered an uncertainty component. The expanded (k=2) combined uncertainty, $U_c(y)$, is defined as:

$$U_c(y) = k\sqrt{u_c(y)^2 + \sigma_y^2} \tag{F4}$$

where the coverage factor, k, is taken as equal to 2, so that the expanded (k=2) combined uncertainty, U_c, defines an interval corresponding to approximately a 95 % confidence level. *Appendices* F.1 and F.2 below describe the uncertainty of the gas velocity and temperature measurements, respectively.

F.1. Uncertainty of Ideal Heat Release Rate

The expanded (k=2) combined uncertainty of the ideal heat release rate calculated from the burning rate is estimated as:

$$U_c(\dot{Q}) = 2\sqrt{u(\dot{Q})^2 + \sigma_R\left(\overline{\dot{Q}}\right)^2 + u_c(\dot{m})^2} \tag{F5}$$

where $u(\dot{Q})$ is the standard uncertainty of the ideal heat release rate and $\sigma_R(\overline{\dot{Q}})$ is the repeatability of the measurement. $u_c(\dot{m})$ is the combined standard (k=1) uncertainty of the ideal mass burning rate. The mean and expanded (k=2) combined uncertainty of the ideal heat release rate is listed in Table 2.

F.2. Gas Temperature Uncertainty Methodology

The measured instantaneous thermocouple bead temperature ($T_b(t)$) is corrected to determine the gas temperature, considering the thermal inertia and radiative loss of the thermocouple. The gas temperature ($T_g(t)$) is related to the sum of the thermocouple measurement ($T_b(t)$), the thermal inertia correction term ($T_{the}(t)$) and the radiative loss correction term ($T_{rad}(t)$):

$$T_g(t) = T_b(t) + T_{the}(t) + T_{rad}(t) = T_b(t) + \tau \frac{dT_b(t)}{dt} + \frac{\epsilon\sigma}{h}(T_b^4(t) - T_{surr}^4) \qquad \text{(F6)}$$

The thermal inertia correction term has a negligible influence on the mean gas temperature, but does amplify the value of the instantaneous temperature extremes and impact the RMS calculation [7, 38]. Details of the uncertainty methodology for the gas temperature are described in Ref. [24].

In this study, the gas temperature was measured using many kinds of fine-wire, bare-bead, and platinum thermocouples using different data acquisition rates, as listed in Table C2. The measurements were typically repeated 2 to 3 times and as often as 10 times.

The pooled mean gas temperature at a particular measurement position ($\overline{T}_g$) is estimated by averaging the mean temperatures from all of the thermocouple measurements: $\overline{T}_g = \left(\sum_{n=1}^{N} \overline{T}_{g,n}\right)/N$, where n is the index of the thermocouple, and N is the total number of thermocouple measurements at the particular measurement location.

The pooled RMS of the gas temperature (σ_{T_g}) is estimated by taking the RMS of the N standard deviation values of the gas temperature time series datasets at a particular measurement location: $\sigma_{T_g} = [{}^1/_N \sum_{n=1}^{N} \sigma_{T_{g,n}}^2]^{1/2}$.

The expanded (k=2) combined uncertainty of the pooled mean gas temperature, $U_c(\overline{T}_g)$, is estimated as:

$$U_c(\overline{T}_g) = 2\sqrt{u_c(\overline{T}_b)^2 + u_c(\overline{T}_{rad})^2 + \sigma_R(\overline{T}_g)^2} \qquad \text{(F7)}$$

where the uncertainties $u_c(T_b)$ and $u_c(\overline{T}_{rad})$ were estimated considering the propagated error from the various terms in Eq. F6. The term $\sigma_R(\overline{T}_g)$ is the repeatability from multiple measurements, which is averaged at 2.5 % across all the measurements in all the pool fires. The sections below present the results of the uncertainty analysis for each fire considered in this report.

F.2.1. Methanol Fire

Table F1. Mean and RMS of the thermocouple bead temperature and the gas temperature along the centerline as a function of the axial distance above the fuel surface in the 30 cm methanol pool fire.

z [cm]	r [cm]	$\overline{T}_b$ [K]	$T_{b,RMS}$ [K]	$\overline{T}_g$ [K]	$T_{g,RMS}$ [K]	$U_c(\overline{T}_g)$ [K]	TCs N
0	0	335	2	335	8	17	1
1	0	919	266	922	293	48	1
2	0	1062	266	1090	371	57	2
3	0	1127	206	1145	370	60	1
4	0	1196	308	1210	528	63	2
5	0	1248	197	1273	340	66	1
6	0	1268	321	1284	531	67	2
7	0	1288	183	1315	312	68	1
8	0	1280	337	1290	405	67	1
10	0	1330	322	1355	685	70	1
11	0	1266	269	1283	363	67	2
14	0	1230	309	1238	393	64	1
15	0	1223	270	1238	375	64	2
20	0	1098	363	1112	791	58	1
21	0	1085	281	1094	399	57	2
30	0	856	341	862	729	45	1
31	0	883	262	887	383	46	2
34	0	836	299	838	404	44	1
41	0	719	265	720	369	37	1
42	0	626	245	628	529	33	1
46	0	628	137	629	245	33	1
51	0	594	208	595	285	31	1
61	0	501	127	501	193	26	2
63	0	449	124	450	268	23	1
64	0	484	131	484	182	25	1
91	0	403	67	403	97	21	1
93	0	385	55	385	118	20	1
111	0	377	45	377	63	20	1
113	0	362	38	363	81	19	1

Table F2. Mean and RMS of the thermocouple bead temperature and the gas temperature as a function of the radial distance from the burner at z = 41 cm, 51 cm, and 61 cm in the 30 cm methanol pool fire.

z [cm]	r [cm]	$\overline{T}_b$ [K]	$T_{b,RMS}$ [K]	$\overline{T}_g$ [K]	$T_{g,RMS}$ [K]	$U_c(\overline{T}_g)$ [K]	TCs N
41	-4	656	256	659	440	34	1
41	-2	727	258	730	444	38	1
41	2	730	221	732	422	41	1
41	4	655	213	657	393	38	1
41	6	586	209	588	375	34	1
41	8	530	179	530	362	31	1
41	10	504	179	504	310	28	1
41	12	461	153	462	299	26	1
41	14	455	162	455	253	24	1
41	16	404	133	404	259	24	1
51	-4	558	178	559	311	29	1
51	-2	620	196	621	340	32	1
51	2	602	169	603	327	33	1
51	4	573	173	574	305	31	1
51	6	539	162	539	300	30	1
51	8	495	146	495	282	28	1
51	10	458	135	458	255	26	1
51	12	473	146	473	232	24	1
51	14	416	120	416	241	25	1
51	16	406	119	406	192	22	1
61	-4	486	142	487	243	25	1
61	-2	521	135	522	240	27	1
61	2	532	135	533	263	28	1
61	4	520	130	520	244	28	1
61	6	489	132	489	231	27	1
61	8	469	117	470	229	25	1
61	10	440	103	440	202	24	1
61	12	421	94	421	177	23	1
61	14	394	83	394	164	22	1
61	16	377	74	377	138	20	1

F.2.2. Ethanol Fire

Table F3. Mean and RMS of the thermocouple bead temperature and the gas temperature along the centerline as a function of the axial distance above the fuel surface in the 30 cm ethanol pool fire.

z [cm]	r [cm]	$\overline{T}_b$ [K]	$T_{b,RMS}$ [K]	$\overline{T}_g$ [K]	$T_{g,RMS}$ [K]	$U_c(\overline{T}_g)$ [K]	TCs N
2	0	839	185	845	345	44	1
3	0	945	188	951	314	49	2
5	0	1108	181	1121	323	58	2
7	0	1197	186	1214	343	63	2
11	0	1252	176	1271	359	66	2
15	0	1260	174	1278	375	66	2
21	0	1222	200	1239	433	64	2
31	0	1031	237	1041	488	54	2
46	0	783	212	786	423	41	2
61	0	606	146	607	288	32	2
76	0	503	99	503	212	26	1
91	0	454	63	454	136	24	1
101	0	430	50	430	113	22	1

F.2.3. Acetone Fire

Table F4. Mean and RMS of the thermocouple bead temperature and the gas temperature along the centerline as a function of the axial distance above the fuel surface in the 30 cm acetone pool fire.

z [cm]	r [cm]	$\overline{T}_b$ [K]	$T_{b,RMS}$ [K]	$\overline{T}_g$ [K]	$T_{g,RMS}$ [K]	$U_c(\overline{T}_g)$ [K]	TCs N
3	0	684	87	686	135	36	3
5	0	818	141	821	163	43	2
7	0	901	145	905	180	47	3
9	0	916	136	949	160	49	1
11	0	1068	154	1075	226	56	3
15	0	1165	162	1174	316	61	2
16	0	1158	134	1168	163	61	1
21	0	1204	139	1215	276	63	3
31	0	1163	186	1172	344	61	3
33	0	1121	250	1131	590	59	1
35	0	1114	253	1124	608	58	1
37	0	1103	261	1113	602	58	1
41	0	1098	243	1107	473	58	2

----- Table F4 **Continued on Next Page** -----

z [cm]	r [cm]	$\overline{T}_b$ [K]	$T_{b,RMS}$ [K]	$\overline{T}_g$ [K]	$T_{g,RMS}$ [K]	$U_c(\overline{T}_g)$ [K]	TCs N
45	0	1015	277	1023	624	53	1
46	0	1050	242	1058	461	55	2
51	0	1020	253	1028	478	53	2
61	0	906	234	911	397	47	3
76	0	687	213	689	444	36	1
91	0	604	159	605	340	31	1
101	0	598	129	598	148	31	1
106	0	502	95	503	203	26	1
131	0	429	54	429	112	22	1

F.2.4. Heptane Fire

Table F5. Mean and standard deviation of the thermocouple bead temperature and the gas temperature near the downstream face of the probe as a function of axial distance above the fuel surface in the 30 cm heptane pool fire.

z [cm]	r [cm]	$\overline{T}_b$ [K]	$T_{b,RMS}$ [K]	$\overline{T}_g$ [K]	$T_{g,RMS}$ [K]	$U_c(\overline{T}_g)$ [K]	TCs N
33	0	1190	183	1202	541	63	1
41	0	1156	228	1166	582	61	1
51	0	1128	257	1138	619	59	1
61	0	1034	300	1042	670	54	1
71	0	968	318	975	668	51	1
91	0	787	234	790	392	41	1
101	0	689	187	691	271	36	1
121	0	562	153	563	214	29	1
131	0	499	121	500	186	26	1
141	0	460	96	460	159	24	1

F.2.5. Methane Fire

Table F6. Mean and RMS of the thermocouple bead temperature and the gas temperature as a function of the axial distance above the burner in the methane gas fire.

z [cm]	r [cm]	$\overline{T}_b$ [K]	$T_{b,RMS}$ [K]	$\overline{T}_g$ [K]	$T_{g,RMS}$ [K]	$U_c(\overline{T}_g)$ [K]	TCs N
1	0	784	227	787	301	41	2
2	0	969	255	975	332	51	2
4	0	1108	247	1118	346	58	3

----- Table F6 **Continued on Next Page** -----

z [cm]	r [cm]	$\overline{T}_b$ [K]	$T_{b,RMS}$ [K]	$\overline{T}_g$ [K]	$T_{g,RMS}$ [K]	$U_c(\overline{T}_g)$ [K]	TCs N
6	0	1200	237	1211	321	63	2
10	0	1314	228	1330	390	69	3
14	0	1334	223	1347	370	70	2
20	0	1321	230	1336	378	69	3
21	0	1274	200	1290	237	67	1
23	0	1235	221	1249	263	65	1
25	0	1198	241	1212	286	63	1
29	0	1165	248	1176	293	61	1
30	0	1204	309	1214	530	63	2
33	0	1102	258	1111	306	58	1
39	0	993	270	1000	319	52	1
45	0	930	300	934	466	49	3
47	0	920	266	925	528	48	1
60	0	740	279	743	412	39	3
62	0	719	267	721	466	37	1
75	0	598	187	600	294	31	2
88	0	536	146	537	176	28	1

F.2.6. Propane Fires

F.2.6.1. The 20 kW Fire

Table F7. Mean and RMS of the thermocouple bead temperature and the gas temperature near the downstream face of the probe as a function of axial distance above the burner in the 20 kW propane gas fire.

z [cm]	r [cm]	$\overline{T}_b$ [K]	$T_{b,RMS}$ [K]	$\overline{T}_g$ [K]	$T_{g,RMS}$ [K]	$U_c(\overline{T}_g)$ [K]
2	0	1105	227	1109	240	58
4	0	1258	236	1264	251	66
6	0	1329	237	1336	256	69
8	0	1327	244	1334	265	69
10	0	1332	255	1339	280	70
14	0	1274	296	1281	327	67
20	0	1146	332	1151	366	60
24	0	1088	350	1092	387	57
27	0	985	235	987	260	51
29	0	952	235	953	259	50

----- Table F7 **Continued on Next Page** -----

z [cm]	r [cm]	$\overline{T}_b$ [K]	$T_{b,RMS}$ [K]	$\overline{T}_g$ [K]	$T_{g,RMS}$ [K]	$U_c(\overline{T}_g)$ [K]
30	0	963	337	966	377	50
31	0	936	224	937	249	49
33	0	867	229	868	251	45
35	0	846	228	847	252	44
39	0	801	211	801	233	42
45	0	711	236	711	261	37
55	0	611	158	611	174	32
60	0	579	194	579	216	30
70	0	505	103	505	113	26
75	0	497	134	497	150	26
85	0	459	75	459	83	24
100	0	424	58	424	64	22

F.2.6.2. The 34 kW Fire

Table F8. Mean and RMS of the thermocouple bead temperature and the gas temperature near the downstream face of the probe as a function of axial distance above the burner in the 34 kW propane gas fire.

z [cm]	r [cm]	$\overline{T}_b$ [K]	$T_{b,RMS}$ [K]	$\overline{T}_g$ [K]	$T_{g,RMS}$ [K]	$U_c(\overline{T}_g)$ [K]
2	0	884	169	885	175	58
4	0	1008	202	1011	238	63
6	0	1117	221	1123	274	64
8	0	1210	199	1214	215	66
10	0	1221	215	1228	292	68
14	0	1267	241	1275	329	66
20	0	1286	243	1299	490	66
24	0	1254	225	1269	578	61
26	0	1250	227	1265	582	53
30	0	1164	284	1174	539	50
35	0	1026	237	1028	270	40
45	0	961	306	967	568	40
55	0	772	221	773	243	33
60	0	766	296	769	517	32
70	0	635	165	635	178	27
75	0	610	222	612	426	26
85	0	528	125	528	137	23

----- Table F8 **Continued on Next Page** -----

z [cm]	r [cm]	$\overline{T}_b$ [K]	$T_{b,RMS}$ [K]	$\overline{T}_g$ [K]	$T_{g,RMS}$ [K]	$U_c(\overline{T}_g)$ [K]
100	0	493	116	493	265	22
115	0	446	75	446	166	58
125	0	417	59	417	66	63

F.2.6.3. The 50 kW Fire

Table F9. Mean and RMS of the thermocouple bead temperature and the gas temperature near the downstream face of the probe as a function of axial distance above the burner in the 50 kW propane gas fire.

z [cm]	r [cm]	$\overline{T}_b$ [K]	$T_{b,RMS}$ [K]	$\overline{T}_g$ [K]	$T_{g,RMS}$ [K]	$U_c(\overline{T}_g)$ [K]
2	0	777	163	778	169	40
4	0	986	204	988	214	51
6	0	1106	207	1109	222	58
8	0	1178	219	1182	240	61
10	0	1195	219	1200	243	62
14	0	1248	243	1254	276	65
20	0	1202	281	1207	322	63
30	0	1161	294	1166	343	61
35	0	1109	232	1112	270	58
39	0	1060	240	1063	276	55
45	0	1026	297	1029	338	54
55	0	959	241	961	271	50
60	0	939	353	941	397	49
70	0	831	179	832	190	43
75	0	809	321	811	358	42
85	0	669	178	670	192	35
100	0	580	129	580	136	30
125	0	463	88	464	96	24
150	0	425	60	425	66	22

F.3. Gas Temperature Datasets for MaCFP

For simplification and consistency, the gas phase temperature data for the MaCFP database was down-selected from the full compilation of gas temperature measurements. Mean and RMS of the thermocouple bead temperature and the gas temperature in the methanol, acetone, ethanol, heptane, methane and propane fires are listed in Tables F10 - F18. Expanded

combined (k=2) uncertainty of the mean gas temperature and the bead diameter of the thermocouple used in each measurement are also listed in the tables.

Table F10. Mean and RMS of the thermocouple bead temperature and the gas temperature along the centerline as a function of the axial distance above the fuel surface in the 30 cm methanol pool fire.

z [cm]	r [cm]	$\overline{T}_b$ [K]	$T_{b,RMS}$ [K]	$\overline{T}_g$ [K]	$T_{g,RMS}$ [K]	$U_c(\overline{T}_g)$ [K]	d_b [μm]
0	0	335	2	335	8	17	52
1	0	919	266	922	293	48	52
2	0	1095	310	1145	358	60	52
4	0	1176	275	1183	318	62	52
6	0	1242	316	1251	373	65	52
8	0	1280	337	1290	405	67	52
11	0	1227	332	1235	414	64	52
14	0	1230	309	1238	393	64	52
15	0	1201	332	1209	433	63	52
21	0	1080	346	1085	460	56	52
31	0	901	321	904	435	47	52
34	0	836	299	838	404	44	52
41	0	719	265	720	369	37	52
51	0	594	208	595	285	31	52
61	0	503	153	503	216	26	52
64	0	484	131	484	182	25	52
91	0	403	67	403	97	21	52

Table F11. Mean and standard deviation of the thermocouple bead temperature and the gas temperature as a function of the radial distance from the burner at z = 41 cm, 51 cm, and 61 cm in the 30 cm methanol pool fire.

z [cm]	r [cm]	$\overline{T}_b$ [K]	σ_{T_b} [K]	$\overline{T}_g$ [K]	σ_{T_g} [K]	$U_c(\overline{T}_g)$ [K]	d_b [μm]
41	-4	656	256	659	440	34	150
41	-2	727	258	730	444	38	150
41	0	781	239	785	422	41	150
41	2	730	221	732	393	38	150
41	4	655	213	657	375	34	150
41	6	586	209	588	362	31	150
41	8	530	179	530	310	28	150

----- Table F11 **Continued on Next Page** -----

z [cm]	r [cm]	$\overline{T}_b$ [K]	σ_{T_b} [K]	$\overline{T}_g$ [K]	σ_{T_g} [K]	$U_c(\overline{T}_g)$ [K]	d_b [µm]
41	10	504	179	504	299	26	150
41	12	461	153	462	253	24	150
41	14	455	162	455	259	24	150
41	16	404	133	404	205	21	150
51	-4	558	150	559	311	29	150
51	-2	620	150	621	340	32	150
51	0	630	150	632	327	33	150
51	2	602	150	603	305	31	150
51	4	573	150	574	300	30	150
51	6	539	150	539	282	28	150
51	8	495	150	495	255	26	150
51	10	458	150	458	232	24	150
51	12	473	150	473	241	25	150
51	14	416	150	416	192	22	150
51	16	406	150	406	185	21	150
61	-4	486	142	487	243	25	150
61	-2	521	135	522	240	27	150
61	0	545	146	545	263	28	150
61	2	532	135	533	244	28	150
61	4	520	130	520	231	27	150
61	6	489	132	489	229	25	150
61	8	469	117	470	202	24	150
61	10	440	103	440	177	23	150
61	12	421	94	421	164	22	150
61	14	394	83	394	138	20	150
61	16	377	74	377	121	20	150

Table F12. Mean and RMS of the thermocouple bead temperature and the gas temperature along the centerline as a function of the axial distance above the fuel surface in the 30 cm ethanol pool fire.

z [cm]	r [cm]	$\overline{T}_b$ [K]	$T_{b,RMS}$ [K]	$\overline{T}_g$ [K]	$T_{g,RMS}$ [K]	$U_c(\overline{T}_g)$ [K]	d_b [µm]
2	0	839	185	845	345	44	199
3	0	961	192	969	339	50	199
5	0	1117	183	1132	313	59	199
7	0	1187	178	1206	294	63	199
11	0	1258	164	1281	271	67	199

----- Table F12 **Continued on Next Page** -----

z [cm]	r [cm]	$\overline{T}_b$ [K]	$T_{b,RMS}$ [K]	$\overline{T}_g$ [K]	$T_{g,RMS}$ [K]	$U_c(\overline{T}_g)$ [K]	d_b [µm]
15	0	1268	153	1291	258	67	199
21	0	1241	169	1261	286	66	199
31	0	1085	190	1097	320	57	199
46	0	809	195	813	330	42	199
61	0	614	146	615	253	32	199
76	0	503	99	503	212	26	125
91	0	454	63	454	136	24	125
101	0	430	50	430	113	22	125

Table F13. Mean and RMS of the thermocouple bead temperature and the gas temperature along the centerline as a function of the axial distance above the fuel surface in the 30 cm acetone pool fire.

z [cm]	r [cm]	$\overline{T}_b$ [K]	σ_{T_b} [K]	$\overline{T}_g$ [K]	σ_{T_g} [K]	$U_c(\overline{T}_g)$ [K]	d_b [µm]
3	0	743	127	745	145	39	103
5	0	856	156	859	177	45	103
7	0	943	164	947	185	49	103
11	0	1086	155	1093	177	57	103
15	0	1191	148	1200	171	62	103
21	0	1237	131	1248	154	65	103
31	0	1212	151	1222	176	64	103
46	0	1074	208	1081	236	56	103
61	0	906	215	910	243	47	103
101	0	598	129	598	148	31	103

Table F14. Mean and RMS of the thermocouple bead temperature and the gas temperature along the centerline as a function of the axial distance above the fuel surface in the 30 cm heptane pool fire.

z [cm]	r [cm]	$\overline{T}_b$ [K]	$T_{b,RMS}$ [K]	$\overline{T}_g$ [K]	$T_{g,RMS}$ [K]	$U_c(\overline{T}_g)$ [K]	d_b [µm]
33	0	1190	183	1202	541	63	125
41	0	1156	228	1166	582	61	125
51	0	1128	257	1138	619	59	125
61	0	1034	300	1042	670	54	125
71	0	968	318	975	668	51	125
91	0	787	234	790	392	41	125
101	0	689	187	691	271	36	125

----- Table F14 **Continued on Next Page** -----

z [cm]	r [cm]	$\overline{T}_b$ [K]	$T_{b,RMS}$ [K]	$\overline{T}_g$ [K]	$T_{g,RMS}$ [K]	$U_c(\overline{T}_g)$ [K]	d_b [µm]
121	0	562	153	563	214	29	125
131	0	499	121	500	186	26	125
141	0	460	96	460	159	24	125

Table F15. Mean and RMS of the thermocouple bead temperature and the gas temperature as a function of the axial distance above the burner in the methane gas fire.

z [cm]	r [cm]	$\overline{T}_b$ [K]	$T_{b,RMS}$ [K]	$\overline{T}_g$ [K]	$T_{g,RMS}$ [K]	$U_c(\overline{T}_g)$ [K]	d_b [µm]
1	0	743	224	744	240	39	52
2	0	949	266	953	287	50	52
4	0	1107	260	1112	281	58	52
6	0	1189	262	1196	290	62	52
10	0	1283	257	1292	310	67	52
14	0	1330	261	1339	348	70	52
20	0	1350	292	1360	420	71	52
30	0	1208	362	1216	527	63	52
45	0	966	373	970	524	50	52
60	0	748	330	749	440	39	52
75	0	591	181	592	346	31	119

Table F16. Mean and RMS of the thermocouple bead temperature and the gas temperature as a function of the axial distance above the burner in the 20 kW propane gas fire.

z [cm]	r [cm]	$\overline{T}_b$ [K]	$T_{b,RMS}$ [K]	$\overline{T}_g$ [K]	$T_{g,RMS}$ [K]	$U_c(\overline{T}_g)$ [K]	d_b [µm]
2	0	1105	227	1109	240	58	39
4	0	1258	236	1264	251	66	39
6	0	1329	237	1336	256	69	39
8	0	1327	244	1334	265	69	39
10	0	1332	255	1339	280	70	39
14	0	1274	296	1281	327	67	39
20	0	1146	332	1151	366	60	39
24	0	1088	350	1092	387	57	39
27	0	985	235	987	260	51	39
29	0	952	235	953	259	50	39
30	0	963	337	966	377	50	39

----- Table F16 **Continued on Next Page** -----

z [cm]	r [cm]	$\overline{T}_b$ [K]	$T_{b,RMS}$ [K]	$\overline{T}_g$ [K]	$T_{g,RMS}$ [K]	$U_c(\overline{T}_g)$ [K]	d_b [µm]
31	0	936	224	937	249	49	39
33	0	867	229	868	251	45	39
35	0	846	228	847	252	44	39
39	0	801	211	801	233	42	39
45	0	711	236	711	261	37	39
55	0	611	158	611	174	32	39
60	0	579	194	579	216	30	39
70	0	505	103	505	113	26	39
75	0	497	134	497	150	26	39
85	0	459	75	459	83	24	39
100	0	424	58	424	64	22	39

Table F17. Mean and RMS of the thermocouple bead temperature and the gas temperature as a function of the axial distance above the burner in the 34 kW propane gas fire.

z [cm]	r [cm]	$\overline{T}_b$ [K]	$T_{b,RMS}$ [K]	$\overline{T}_g$ [K]	$T_{g,RMS}$ [K]	$U_c(\overline{T}_g)$ [K]	d_b [µm]
2	0	850	168	851	174	44	39
4	0	1045	219	1048	228	54	39
6	0	1131	231	1135	244	59	39
8	0	1204	219	1208	236	63	39
10	0	1236	220	1241	242	65	39
14	0	1293	257	1300	291	68	39
20	0	1267	282	1273	326	66	39
30	0	1144	327	1149	377	60	39
34	0	1144	329	1148	383	60	39
45	0	900	340	903	381	47	39
60	0	731	291	732	325	38	39
70	0	635	165	635	178	33	39
85	0	528	125	528	137	27	39
125	0	417	59	417	66	22	39

Table F18. Mean and RMS of the thermocouple bead temperature and the gas temperature as a function of the axial distance above the burner in the 50 kW propane gas fire.

z [cm]	r [cm]	$\overline{T}_b$ [K]	$T_{b,RMS}$ [K]	$\overline{T}_g$ [K]	$T_{g,RMS}$ [K]	$U_c(\overline{T}_g)$ [K]	d_b [µm]
2	0	770	138	771	143	40	39
4	0	999	186	1001	194	52	39
6	0	1122	183	1125	194	59	39
8	0	1176	188	1180	203	61	39
10	0	1207	193	1212	211	63	39
14	0	1209	210	1213	236	63	39
20	0	1153	246	1157	279	60	39
30	0	1093	268	1096	307	57	39
35	0	1109	232	1112	270	58	39
39	0	1060	240	1063	276	55	39
45	0	1012	260	1014	296	53	39
55	0	959	241	961	271	50	39
70	0	831	179	832	190	43	39
85	0	669	178	670	192	35	39
100	0	580	129	580	136	30	39
125	0	463	88	464	96	24	39
150	0	425	60	425	66	22	39

F.4. Gas Velocity Uncertainty Methodology

The instantaneous gas velocity in the upward direction ($V_g(t)$) is estimated from the measurement of the pressure difference across a bidirectional probe and the gas temperature near the downward face of the probe, applying the velocity model for a bidirectional probe [17] as reproduced here:

$$V_g(t) = \frac{1}{k_p(t)}\sqrt{\frac{2\Delta P_c(t)}{\rho(t)}} \tag{F8}$$

where $\Delta P_c(t)$ and $\rho(t)$ are the instantaneous corrected pressure difference and gas density, respectively. The gas density $\rho(t)$ is determined from the thermocouple temperature measurement using a fine, bare-bead, Type S thermocouple corrected for radiative loss and the assumption that the gas constant corresponds to that of air. The instantaneous gas velocity for every measured data point is calculated with the time series of instantaneous measurements of the parameters in Eq. F8. The temperature-dependent gas properties are taken as those of air [27].

The time series of the gas velocity was acquired at each measurement location using multiple pressure transducers, which were typically repeated 2 to 3 times and as often as 10 times. The pooled mean gas velocity at a particular measurement position ($\overline{V}_g$) is estimated by averaging the mean gas velocities from all of the pressure transducers: $\overline{V}_g = \left(\sum_{n=1}^{N} \overline{V}_{g,n}\right)/N$ where n is the index of the pressure transducers and N is the total number of pressure transducers used. The expanded (k=2) combined uncertainty of the mean gas velocity at a particular measurement position, $U_c(\overline{V}_g)$, is estimated by considering the repeat measurements:

$$U_c(\overline{V}_g) = 2\sqrt{\left(\frac{1}{2}u_c(\Delta P_c)\right)^2 + \left(\frac{1}{2}u_c(\rho_g)\right)^2 + u_c(k_p)^2 + \sigma(PTs)^2 + \sigma_R(\overline{V}_g)^2} \qquad \text{(F9)}$$

where the term $u_c(k_p)$, is the uncertainty of the empirical correlation (defined in Eq. 8) estimated as 5 % [17]. The term $u_c(\rho_g)$ is the uncertainty of the air density, estimated as $u_c(T_g)$ with a value of 2.6 %. The term $\sigma_R(\overline{V}_g)$ is the repeatability from multiple measurements, which is averaged at 2.8 % across all the measurements in all the pool fires. The term $u_c(\Delta P_c)$ is the uncertainty of the pressure difference correction estimated as:

$$u_c(\Delta P_c) = \sqrt{u_c(\tau_p)^2 + u_c\left(\frac{d\Delta P}{dt}\right)^2} \qquad \text{(F10)}$$

where the term $u_c(\tau_p)$ is 2.5 % averaged across all the pressure transducers used here. The response time of the pressure transducer (τ_p) was measured as discussed in *Appendix B*. The uncertainty of the time derivative of the pressure difference $\left(u_c\left(\frac{d\Delta P}{dt}\right)\right)$ is estimated as 5.2 %, based on curve fitting error as described in Ref. [24].

In Eq. F9, the term $\sigma(PTs)$ is the repeatability of the gas velocity arising from using different pressure transducers during each measurement. It is defined as the ratio of the standard deviation (SD) of the average gas velocity ($\overline{V}_{g,n}$) to the pooled mean gas velocity ($\overline{V}_g$). Figure F1 shows the repeatability $\sigma(PTs)$ as a function of the pooled mean gas velocity ($\overline{V}_g$) in the pool fire tests used multiple pressure transducers. The uncertainty in repeatability increased by 47 % when $\overline{V}_g$ was less than 0.5 m/s due to the low accuracy of the pressure transducers in the low-velocity regime, but it subsequently decreased sharply. The $\sigma(PTs)$ is estimated using a power law fit: $\sigma(PTs) = 8.77\bar{V}_g^{-1.92}$.

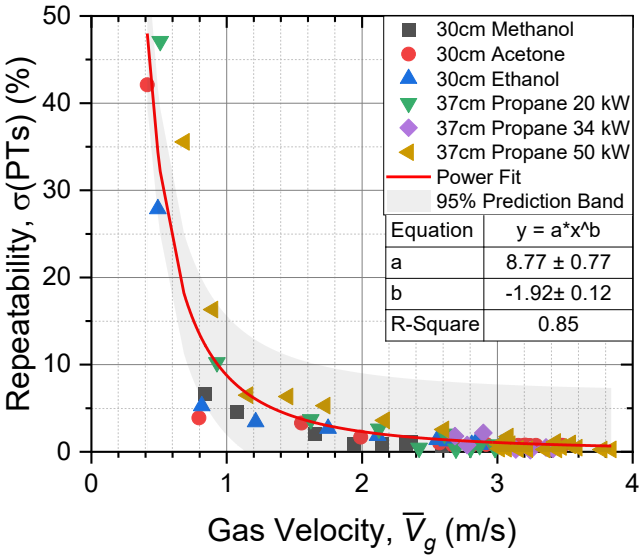

Fig. F1. Repeatability of the velocity measurement ($\sigma(PTs)$) as a function of the pooled mean gas velocity ($\overline{V}_g$) considering all the pool fire experiments. A power law fit (red line) is also shown.

Tables F19 - F20 present the combined uncertainty budget of the mean gas velocity at (*z*, *r*) = (2 cm, 0 cm) and (*z*, *r*) = (36 cm, 0 cm) in the 30 cm acetone fire, respectively. The variance associated with the use of multiple pressure transducers, $u_c(PTs)$, is the dominant factor affecting the combined uncertainty near the fuel surface. The type B uncertainties, such as $u_c(k_p)$ and $u_c(\Delta P_c)$, become more significant at distances farther from the burner. This trend is observed in all the pool fires.

Table F19. Uncertainty budget of the pooled mean gas velocity, $u_c(\overline{V}_g)$, at (*z*, *r*) = (2 cm, 0 cm) in the 30 cm acetone fire.

Parameter, x	$u_c(x)$ (-)	s_x (-)	Contribution (%)
ρ_g	2.6 %	-0.5	0.1 %
k_p	5.0 %	-1	0.3 %
ΔP_c	5.8 %	0.5	0.4 %
PTs	48 %	1	99 %
σ_R	2.8 %	1	0.3 %
$\bar{V}_g$	**48 % (k=1)**		100 %

Table F20. Uncertainty budget of the pooled mean gas velocity, $u_c(\overline{V}_g)$, at (*z*, *r*) = (36 cm, 0 cm) in the 30 cm acetone fire.

Parameter, x	$u_c(x)$(-)	s_x (-)	Contribution (%)
ρ_g	2.6 %	-0.5	4 %
k_p	5.0 %	-1	57 %
ΔP_c	5.8 %	0.5	19 %
PTs	0.9 %	1	2 %
σ_R	2.8 %	1	18 %
$\bar{V}_g$	**6.6 % (k=1)**		100 %

F.4.1. Methanol Fire

Table F21 shows the pooled mean gas velocity ($\overline{V}_g$) and the expanded (k=2) combined uncertainty ($U_c(\overline{V}_g)$) relative to the axial distance above the burner in the 30 cm methanol pool fire.

Table F21. The pooled mean gas velocity ($\overline{V}_g$) and its expanded (k=2) combined uncertainty ($U_c(V_g)$) as a function of axial distance above the fuel surface in the 30 cm methanol pool fire.

z [cm]	r [cm]	$\overline{V}_g$ [m/s]	$U_c(\overline{V}_g)$ [%]	Pressure Transducer, N	Repeat Measurements, M
4	0	0.84	0.23	3	1
6	0	1.08	0.22	3	1
10	0	1.65	0.24	3	3
20	0	2.36	0.32	3	3
30	0	2.59	0.35	3	3
42	0	2.59	0.35	3	1
63	0	2.33	0.32	3	3
93	0	2.15	0.29	3	4
113	0	1.94	0.27	3	2

F.4.2. Ethanol Fire

Table F22 shows the pooled mean gas velocity ($\overline{V}_g$) and the expanded (k=2) combined uncertainty ($U_c(\overline{V}_g)$) relative to the axial distance above the burner in the 30 cm ethanol pool fire.

Table F22. The pooled mean gas velocity ($\overline{V}_g$) and its expanded (k=2) combined uncertainty ($U_c(V_g)$) as a function of axial distance above the fuel surface in the 30 cm ethanol pool fire.

z [cm]	r [cm]	$\overline{V}_g$ [m/s]	$U_c(\overline{V}_g)$ [m/s]	Pressure Transducer, N	Repeat Measurements, M
3	0	0.49	0.23	2	3
5	0	0.82	0.22	2	5
7	0	1.21	0.24	3	5
11	0	1.75	0.32	3	6
15	0	2.12	0.35	3	7
21	0	2.56	0.35	3	7
31	0	2.84	0.32	3	7
46	0	3.04	0.29	3	7
61	0	3.02	0.27	3	7
76	0	2.87	0.23	3	7
91	0	2.81	0.22	3	5
101	0	2.63	0.24	3	2

F.4.3. Acetone Fire

Table F23 shows the pooled mean gas velocity ($\overline{V}_g$) and the expanded (k=2) combined uncertainty ($U_c(\overline{V}_g)$) relative to the axial distance above the burner in the 30 cm acetone pool fire.

Table F23. The pooled mean gas velocity ($\overline{V}_g$) and its expanded (k=2) combined uncertainty ($U_c(V_g)$) as a function of axial distance above the fuel surface in the 30 cm acetone pool fire.

z [cm]	r [cm]	$\overline{V}_g$ [m/s]	$U_c(\overline{V}_g)$ [m/s]	Pressure Transducer, N	Repeat Measurements, M
3	0	0.41	0.40	2	1
7	0	0.79	0.24	2	1
11	0	1.55	0.23	3	2
15	0	1.99	0.28	3	2
21	0	2.57	0.34	3	2
31	0	2.92	0.39	3	2
33	0	3.10	0.41	3	2
35	0	3.15	0.42	3	2
37	0	3.24	0.43	3	2

----- Table F23 **Continued on Next Page** -----

z [cm]	r [cm]	$\overline{V}_g$ [m/s]	$U_c(\overline{V}_g)$ [m/s]	Pressure Transducer, N	Repeat Measurements, M
41	0	3.29	0.44	3	2
45	0	3.45	0.46	3	2
46	0	3.43	0.45	3	1
51	0	3.48	0.46	3	2
61	0	3.47	0.46	3	2
76	0	3.21	0.42	3	2
91	0	3.20	0.42	3	2
106	0	2.81	0.37	3	2
131	0	2.67	0.36	3	2

F.4.4. Heptane Fire

Table F24 shows the pooled mean gas velocity ($\overline{V}_g$) and the expanded (k=2) combined uncertainty ($U_c(\overline{V}_g)$) relative to the distance above the burner in the 30 cm heptane pool fire.

Table F24. The pooled mean gas velocity ($\overline{V}_g$) and its expanded (k=2) combined uncertainty ($U_c(V_g)$) as a function of axial distance above the fuel surface in the 30 cm heptane pool fire.

z [cm]	r [cm]	$\overline{V}_g$ [m/s]	$U_c(\overline{V}_g)$ [m/s]	Pressure Transducer, N	Repeat Measurements, M
33	0	3.08	0.40	3	2
41	1	3.42	0.24	3	3
51	2	3.70	0.23	3	1
61	3	3.76	0.28	3	1
71	4	3.71	0.34	3	1
91	5	3.54	0.39	3	1
101	6	3.38	0.41	3	1
121	7	3.11	0.42	3	1
131	8	2.67	0.43	3	1
141	9	2.44	0.44	3	1

F.4.5. Methane Fire

Table F25 shows the pooled mean gas velocity ($\overline{V}_g$) and the expanded (k=2) combined uncertainty ($U_c(\overline{V}_g)$) relative to the axial distance above the burner in the 37 cm methane gas fire.

Table F25. The pooled mean gas velocity ($\overline{V}_g$) and its expanded (k=2) combined uncertainty ($U_c(V_g)$) as a function of axial distance above the burner in the methane gas fire.

z [cm]	r [cm]	$\overline{V}_g$ [m/s]	$U_c(\overline{V}_g)$ [m/s]	Pressure Transducer, N	Repeat Measurements, M
4	0	0.64	0.28	1	1
10	0	1.65	0.24	1	1
20	0	2.63	0.35	1	1
21	0	2.70	0.36	1	1
23	0	2.77	0.37	1	1
25	0	2.88	0.38	1	1
29	0	3.09	0.41	1	1
30	0	3.15	0.42	1	1
33	0	3.25	0.43	1	1
39	0	3.37	0.45	1	1
45	0	3.41	0.45	1	1
60	0	3.44	0.45	1	2
75	0	3.23	0.43	1	2
88	0	3.07	0.41	1	1

F.4.6. Propane Fires

F.4.6.1. The 20 kW Fire

Table F26 shows the pooled mean gas velocity ($\overline{V}_g$) and the expanded (k=2) combined uncertainty ($U_c(\overline{V}_g)$) relative to the distance above the burner in the 20 kW propane gas fire.

Table F26. The pooled mean gas velocity ($\overline{V}_g$) and its expanded (k=2) combined uncertainty ($U_c(V_g)$) as a function of axial distance above the burner in the 20 kW propane gas fire.

z [cm]	r [cm]	$\overline{V}_g$ [m/s]	$U_c(\overline{V}_g)$ [m/s]	Pressure Transducer, N	Repeat Measurements, M
4	0	0.51	0.33	3	2
6	0	0.93	0.22	3	2
10	0	1.62	0.24	3	2
14	0	2.12	0.29	3	2
20	0	2.61	0.35	3	2
24	0	2.78	0.37	1	3

----- Table F26 **Continued on Next Page** -----

z [cm]	r [cm]	$\overline{V}_g$ [m/s]	$U_c(\overline{V}_g)$ [m/s]	Pressure Transducer, N	Repeat Measurements, M
27	0	2.89	0.38	3	1
29	0	2.96	0.39	3	1
30	0	2.87	0.38	3	3
31	0	3.06	0.41	3	1
33	0	2.99	0.40	3	1
35	0	3.05	0.40	3	2
39	0	3.12	0.41	3	1
40	0	2.99	0.40	3	3
45	0	3.03	0.40	3	11
55	0	3.01	0.40	3	2
60	0	2.8	0.37	3	9
70	0	2.77	0.37	3	1
75	0	2.69	0.36	3	6
85	0	2.75	0.37	3	2
100	0	2.51	0.34	3	7

F.4.6.2. The 34 kW Fire

Table F27 shows the pooled mean gas velocity ($\overline{V}_g$) and the expanded (k=2) combined uncertainty ($U_c(\overline{V}_g)$) relative to the xial distance above the burner in the 34 kW propane gas fire.

Table F27. The pooled mean gas velocity ($\overline{V}_g$) and its expanded (k=2) combined uncertainty ($U_c(V_g)$) as a function of axial distance above the burner in the 34 kW propane gas fire.

z [cm]	r [cm]	$\overline{V}_g$ [m/s]	$U_c(\overline{V}_g)$ [m/s]	Pressure Transducer, N	Repeat Measurements, M
2	0	0.73	0.25	3	1
4	0	0.99	0.22	3	1
6	0	1.24	0.22	3	1
8	0	1.51	0.23	3	1
10	0	1.77	0.25	3	1
14	0	2.18	0.30	3	1
20	0	2.6	0.35	3	1
24	0	2.78	0.37	2	8
26	0	2.95	0.39	1	6

----- Table F27 **Continued on Next Page** -----

z [cm]	r [cm]	$\overline{V}_g$ [m/s]	$U_c(\overline{V}_g)$ [m/s]	Pressure Transducer, N	Repeat Measurements, M
27	0	3.06	0.41	3	1
29	0	3.1	0.41	3	2
30	0	3.06	0.41	3	7
31	0	3.21	0.42	3	2
34	0	3.24	0.43	3	7
35	0	3.33	0.44	3	3
39	0	3.26	0.43	3	3
45	0	3.41	0.45	3	11
55	0	3.42	0.45	3	3
60	0	3.36	0.44	2	5
70	0	3.34	0.44	3	2
75	0	3.14	0.42	3	4
85	0	3.01	0.40	3	4
100	0	2.9	0.39	3	5
115	0	2.69	0.36	3	10

F.4.6.3. The 50 kW Fire

Table F28 the pooled mean gas velocity ($\overline{V}_g$) and the expanded (k=2) combined uncertainty ($U_c(\overline{V}_g)$) relative to the axial distance above the burner in the 50 kW propane gas fire.

Table F28. The pooled mean gas velocity ($\overline{V}_g$) and its expanded (k=2) combined uncertainty ($U_c(V_g)$) as a function of axial distance above the burner in the 50 kW propane gas fire.

z [cm]	r [cm]	$\overline{V}_g$ [m/s]	$U_c(\overline{V}_g)$ [m/s]	Pressure Transducer, N	Repeat Measurements, M
2	0	0.69	0.26	3	2
4	0	0.9	0.23	3	1
6	0	1.16	0.22	3	1
8	0	1.45	0.23	3	1
10	0	1.73	0.25	3	1
14	0	2.17	0.30	3	1
20	0	2.6	0.35	3	1
27	0	3.02	0.40	3	3
29	0	3.07	0.41	3	1
30	0	3.08	0.41	3	1

----- Table F28 **Continued on Next Page** -----

z [cm]	r [cm]	$\overline{V}_g$ [m/s]	$U_c(\overline{V}_g)$ [m/s]	Pressure Transducer, N	Repeat Measurements, M
31	0	3.15	0.42	3	1
33	0	3.22	0.43	3	1
35	0	3.35	0.44	3	2
39	0	3.44	0.45	3	1
45	0	3.54	0.47	3	2
55	0	3.77	0.50	3	2
70	0	3.84	0.51	3	1
85	0	3.59	0.47	3	3
100	0	3.47	0.46	3	2
125	0	3.09	0.41	3	1

F.5. Uncertainty of the Estimate of Radiative Fraction Based on a Single- Point Measurement

The expanded (k=2) combined uncertainty of the radiative fraction estimate is estimated, considering Eq. 10 in *Section 2.8*:

$$U_c(\chi_{rad}) = 2\sqrt{u_c(\dot{m})^2 + u_c(\dot{q}'')^2 + u_c\left(\dot{Q}_{rad,model}\right)^2 + \left(2u_c(r)\right)^2 + \sigma_R(\chi_{rad})^2} \qquad \text{(F11)}$$

where the term $u_c(\dot{m})$ is the combined standard (k=1) uncertainty of the burning rate. The term $\sigma_R(\chi_{rad})$ represents measurement repeatability. The term $u_c(r)$ is the positioning uncertainty of the radial distance, which is 1 % in general.

Modak [30] suggests that a distance five times the diameter of a fire is adequate to use a single-point location measurement to estimate the total radiative flux (assuming isotropy). This approach tends to underestimate the total radiative energy emitted by the flame. At *r/D* = 5, the bias is about 2 % Modak [30]. This bias is treated as an uncertainty in the single point radiation estimate of $u_c(\dot{Q}_{rad,model})$.

The measured (uncorrected) heat flux can be affected by the temperature of the surroundings (walls, calorimeter hood, and so on). This temperature increase causes the heat flux background to slightly increase during the steady burning period. The background heat flux is subtracted from the measured heat flux, and the background heat flux estimate details are described in Ref. [24]. In Eq. F11, the combined uncertainty of the corrected heat flux, $u_c(\dot{q}'')$, is estimated as:

$$u_c(\dot{q}'') = \sqrt{u_c(\dot{q}_b'')^2 + u_c(cal.)^2 + u_c(DAQ)^2} \quad \text{(F12)}$$

where the term $u_c(\dot{q}_b'')$ is the heat flux background subtraction uncertainty of 5 %. The heat flux gauges were calibrated using a secondary standard gauge in a well-characterized calibration facility [51]. The calibration method and apparatus are described in Ref. [52]; the systematic uncertainty for the calibration, $u_c(cal)$, is estimated as 4.5 % [51]. The measurement accuracy of the data acquisition system (DAQ, Model: SCXI-1600), $u_c(DAQ)$, is 0.076 % for the application range used here [49].

Table F29 lists the uncertainty budget of the estimated radiative fraction estimate based on a single point measurement in the 30 cm methanol fire. The table shows that the combined (68 % confidence level) uncertainty $\left(u_c(\chi_{rad})\right)$ of the radiative fraction estimate is about 10%.

Table F29. The combined standard (k=1) uncertainty $(u_c(\chi_{rad}))$ of the single point radiative fraction estimate in the 30 cm methanol pool fire considering heat flux measurements at various radial distances (r) from the fire (listed in Table 8 and Tables F30 - F35 below).

Parameter	$s_i(x)$ [-]	Combined uncertainty $u_c(x)$ [-]	Contributions [-]
Burning rate, $\dot{m}$	1	2.5 %	7 %
Heat flux, $\dot{q}''$	1	6.7 %	49 %
Repeatability, σ_R	1	5.8 %	36 %
Single point radiation model	1	2.0 %	4 %
Radial distance, r	2	1.0 %	4 %
χ_{rad}	Sum	9.6 %	100 %

F.5.1. Methanol Fire

Table F30 shows the results of 12 heat flux measurements made at six radial positions varying from 10 to 17 radii from the burner centerline. Each experiment used two heat flux gauges at different distances from the fire. The mean radiative fraction χ_{rad} is 23 % with a standard deviation of about 0.01.

Table F30. Mass loss, ideal heat release rate, heat flux gauge locations, fluxes and calculated radiative fractions for four experiments with gauges at various radial distances (r) directed towards the fire and located at a vertical position, z =15 cm, in the 30 cm methanol fire. The uncertainties are expressed as the standard deviation of the measurements.

r [m]	z [m]	$\dot{q}''$ [kW/m^2]	$\dot{Q}$ [kW]	χ_{rad} [-]	n
1.92	0.15	0.09	18.3	0.22	2
2.00	0.15	0.08	18.5	0.21	2
2.07	0.15	0.08	18.3	0.23	1
2.31	0.15	0.06	18.4	0.23	1
2.50	0.15	0.05	18.5	0.23	5
3.00	0.15	0.04	18.5	0.23	1
Average ± SD			18.4 ± 0.3	0.23 ± 0.01	

F.5.2. Ethanol Fire

Table F31 shows the results of experiments where heat flux measurements were made at distances from 6.9 to 8.4 radii from the pool burner center. The mean radiative fraction χ_{rad} is 26 %.

Table F31. The ideal heat release rate and radiative fractions measured at various radial distances (r) directed towards the fire with z = 15 cm in the 30 cm ethanol fire. The uncertainties are expressed as the standard deviation (SD) of the measurements.

r [m]	z [m]	$\dot{q}''$ [kW/m^2]	$\dot{Q}$ [kW]	χ_{rad} [-]	n
2.07	0.15	0.13	27.5	0.25	1
2.52	0.15	0.09	28.0	0.26	2
Average ± SD			27.8 ± 0.2	0.26 ± 0.001	

F.5.3. Acetone Fire

Table F32 shows the results of experiments in which heat flux measurements were made at distances from 6.8 to 10.2 radii from the pool burner center. The mean radiative fraction χ_{rad} is 31 %.

Table F32. The ideal heat release rate and radiative fractions measured at various radial distances (r) directed towards the fire with z = 15 cm in the 30 cm acetone fire. The uncertainties are expressed as the standard deviation (SD) of the measurements.

r [m]	z [m]	$\dot{q}''$ [kW/m²]	$\dot{Q}$ [kW]	χ_{rad} [-]	n
2.05	0.15	0.24	40.0	0.32	3
2.50	0.15	0.15	43.5	0.27	1
3.06	0.15	0.12	43.6	0.31	3
Average ± SD			42.0 ± 3.2	0.31 ± 0.01	

F.5.4. Heptane Fire

Table F33 shows the results of two experiments in which heat flux measurements were made at distances from 15.1 to 16.7 radii from the pool burner center. The mean radiative fraction χ_{rad} is 35 % with a standard deviation of about 0.03.

Table F33. The ideal heat release rate and radiative fractions measured at various radial distances (r) directed towards the fire and at two vertical positions, z = 15 cm and 46 cm, in the 30 cm heptane fire. The uncertainties are expressed as the standard deviation (SD) of the measurements.

r [m]	z [m]	$\dot{q}''$ [kW/m²]	$\dot{Q}$ [kW]	χ_{rad} [-]	n
2.05	0.15	0.62	101.4	0.32	1
2.34	0.46	0.61	111.8	0.38	1
Average ± SD			106.6 ± 5.2	0.35 ± 0.03	

F.5.5. Methane Fire

Table F34 shows the results of four experiments in which heat flux measurements were made at distances from 10 to 12.4 radii from the pool burner center. The mean radiative fraction χ_{rad} is 21 %.

Table F34. The ideal heat release rate and radiative fractions measured at various radial distances (r) directed towards the fire and at two vertical positions, z = 40 cm and 60 cm, in the methane gas fire. The uncertainties are expressed as the standard deviation (SD) of the measurements.

r [m]	z [m]	$\dot{q}''$ [kW/m^2]	$\dot{Q}$ [kW]	χ_{rad} [-]	n
1.85	0.40	0.17	34.5	0.21	1
1.85	0.60	0.17	34.5	0.21	1
2.04	0.40	0.15	34.5	0.23	1
2.04	0.60	0.14	34.5	0.21	1
2.29	0.40	0.11	34.5	0.21	1
2.29	0.60	0.11	34.5	0.21	1
Average ± SD				0.21 ± 0.01	

F.5.6. Propane Fires

Table F35 shows the results of experiments for the 20 kW, 34 kW, and 50 kW in which heat flux measurements were made at distances from 11 to 12.4 radii from the pool burner center. The mean radiative fractions, χ_{rad}, are 23%, 30 %, and 33 % for the 20 kW, 34 kW, and 50 kW fires, respectively. The standard deviations of the measurements are also listed in Table F35.

Table F35. The ideal heat release rate and radiative fractions measured at various radial distances (r) directed towards the fire and located at a vertical position, z = 27 cm and 40 cm, in the 20 kW, 34 kW, and 50 kW propane gas fires. The uncertainties are expressed as the standard deviation (SD) of the measurements.

		$\dot{Q}$ = 20.7 kW		$\dot{Q}$ = 34.4 kW		$\dot{Q}$ = 50.1 kW	
r [m]	z [m]	$\dot{q}''$ [kW]	χ_{rad} [-]	$\dot{q}''$ [kW]	χ_{rad} [-]	$\dot{q}''$ [kW]	χ_{rad} [-]
2.04	0.27	-	-	0.20	0.30	0.32	0.34
2.04	0.40	0.09	0.23	0.19	0.29	0.31	0.32
2.22	0.27	0.08	0.24	0.17	0.30	0.26	0.33
2.29	0.40	0.07	0.22	0.16	0.30	0.24	0.32
Average ± SD			0.23 ± 0.01		0.30 ± 0.004		0.33 ± 0.01

F.6. Uncertainty of the Fractional Total Heat Feedback to the Fuel Surface

The expanded (k=2) combined uncertainty of the total heat feedback onto the burner ($U_c(\dot{Q}_b)$) is estimated, considering Eq. 9 in *Section 2.8*:

$$U_c(\dot{Q}_b) = 2\sqrt{u_c(\dot{V}_w)^2 + u_c(TC)^2 + \sigma_R(\dot{Q}_b)^2} \quad \text{(F13)}$$

where and $u_c(\dot{V}_w)$ is the standard uncertainty of the volumetric flow rate of cooling water, considering a reading accuracy of the graduated cylinder (± 1 ml). The accuracy of the K-type thermocouple, $u_c(TC)$, is 0.75 %[6] . $\sigma_R(\dot{Q}_b)$ is the repeatability. The expanded (k=2) uncertainty of the fractional total heat feedback onto the burner, $U_c(\chi_b)$, is estimated as $\sqrt{U_c(\dot{Q})^2 + U_c(\dot{Q}_b)^2}$

Table F36. Mean values of the burner cooling water temperature, water flow rate, heat feedback, and the fractional heat feedback to the surface of the burner during the methane fire.

Test #	$\overline{\dot{Q}}$ [kW]	$\overline{\Delta T_w}$ [°C]	$\overline{\dot{V}_w}$ [mL/s]	$\overline{\dot{Q}_b}$ [kW]	$\overline{\chi_b}$ [-]
25	34.5	39	15.3	2.5	0.072
27	34.5	37	16.3	2.5	0.073
29	34.5	43	13.7	2.5	0.071
30	34.5	43	13.7	2.4	0.071
31	34.5	44	13.3	2.4	0.070
32	34.5	44	13.3	2.4	0.070

Table F37. Mean values of the burner cooling water temperature, water flow rate, heat feedback, and the fractional heat feedback on the burner in 20 kW, 34 kW, and 50 kW propane fires.

Date	$\overline{\dot{Q}}$ [kW]	$\overline{T_i}$ [ºC]	$\overline{T_o}$ [ºC]	$\overline{\Delta T_w}$ [°C]	$\overline{\dot{V}_w}$ [mL/s]	$\overline{\dot{Q}_b}$ [kW]	$\overline{\chi_b}$ [-]
2019/11/20	20.7	31	42	12	54	2.6	0.13
2019/11/20	20.7	28	39	12	54	2.6	0.13
2019/11/20	20.7	27	38	12	54	2.6	0.13
2019/11/20	20.7	27	39	12	54	2.7	0.13
2019/11/20	20.7	27	39	12	54	2.7	0.13
2021/11/02	20.7	26	54	28	22	2.5	0.12
2019/11/13	34.4	28	41	13	56	3.0	0.09
2019/11/13	34.4	26	38	12	56	2.9	0.09
2019/11/13	34.4	26	39	12	56	2.9	0.08
2021/11/02	34.4	27	58	30	22	2.7	0.08
2021/11/02	50.1	27	55	28	22	2.6	0.05
2021/11/05	50.1	27	60	33	18	2.4	0.05

[6] https://www.omega.com/en-us/resources/thermocouple-types.

Table F38. The measured local heat feedback towards the fuel surface in the 30 cm methanol, acetone, ethanol fires [11] and heptane fires [8]. The r and z locations are the radial distance from burner center and axial distance from the fuel surface, respectively. The standard deviation of the local heat flux ($\sigma(\dot{q}'')$) is determined from repeat measurements.

Fuel	r [cm]	Z [cm]	$\dot{q}''$ [kW/m^2]	$\sigma(\dot{q}'')$ [kW/m^2]	Repeat [-]
Methanol	0	1.3	26.5	1.7	5
Methanol	3	1.3	24.9	-	1
Methanol	6	1.3	26.9	2.1	7
Methanol	10	1.3	22.6	3.1	4
Methanol	12	1.3	18.1	3.4	4
Methanol	13	1.3	16.0	0.5	2
Methanol	14	1.3	5.3	0.5	4
Methanol	14.5	1.3	4.0	-	1
Methanol	14.7	1.3	3.5	-	1
Acetone	0	1.3	25.6	2.4	9
Acetone	3	1.3	27.8	1.3	4
Acetone	6	1.3	25.3	2.9	17
Acetone	8	1.3	25.1	1.5	2
Acetone	10	1.3	22.0	1.0	8
Acetone	12	1.3	22.5	1.4	5
Acetone	13	1.3	20.6	0.7	2
Acetone	14	1.3	26.0	7.4	9
Acetone	14.5	1.3	24.4	8.8	5
Ethanol	0	1.3	32.4	0.1	2
Ethanol	3	1.3	29.2	-	1
Ethanol	6	1.3	28.7	0.7	4
Ethanol	10	1.3	24.8	0.4	2
Ethanol	12	1.3	21.6	2.1	2
Ethanol	14	1.3	12.8	0.8	2
Ethanol	14.5	1.3	7.1	-	1
Heptane	0	1.3	21.6	-	1
Heptane	2	1.3	20.9	-	1
Heptane	4	1.3	19.4	-	1
Heptane	5	1.3	20.1	-	1
Heptane	6	1.3	19	-	1
Heptane	8	1.3	18.6	-	1
Heptane	10	1.3	17.8	-	1

----- Table F38 **Continued on Next Page** -----

Fuel	r [cm]	Z [cm]	$\dot{q}''$ [kW/m^2]	$\sigma(\dot{q}'')$ [kW/m^2]	Repeat [-]
Heptane	12	1.3	16.2	-	1
Heptane	13	1.3	14.4	-	1
Heptane	14	1.3	15.6	-	1
Heptane	15	1.3	20.1	-	1

Appendix G. Liquid Fuel Temperature

Table G1. The measured fuel temperature changes in time (T_f) at various measurement positions (r, z) in the methanol fire.

Time [s]	T_f [K]	T_f [K]	T_f [K]	T_f [K]	T_f [K]
r [cm]	1.0	13.0	1.0	13.0	1.0
z [cm]	-0.8	-0.9	-3.3	-3.5	-6.8
-50	291.1	290.9	291.1	291.2	291.0
0	291.1	290.9	291.1	291.2	291.0
50	299.3	293.6	291.2	291.3	291.1
100	307.6	298.1	291.5	291.5	291.3
150	315.4	303.5	291.4	291.4	291.2
200	320.1	307.9	292.0	292.0	291.6
250	323.1	310.6	292.0	292.0	291.6
300	324.3	312.3	292.2	292.1	291.6
350	325.6	313.9	292.6	292.2	291.6
400	326.3	315.1	292.7	292.2	291.4
450	327.5	316.7	293.2	292.5	291.6
500	327.8	317.8	293.7	292.9	291.8
550	328.8	318.8	294.4	293.3	292.0
600	328.9	319.5	294.6	293.4	291.9
650	329.5	320.0	295.0	293.9	292.1
700	330.5	320.8	295.1	294.1	292.1
750	330.4	320.8	295.1	294.0	291.8
800	331.1	321.5	295.5	294.5	292.0
850	331.0	322.6	296.2	295.1	292.3
900	331.1	322.6	296.4	295.1	292.2
950	332.2	323.4	296.8	295.6	292.5
1000	331.8	323.5	296.9	295.7	292.3
1050	332.5	323.5	297.2	295.9	292.3

----- Table G1 **Continued on Next Page** -----

Time [s]	T_f [K]	T_f [K]	T_f [K]	T_f [K]	T_f [K]
1100	332.2	324.0	297.7	296.3	292.6
1150	332.2	324.2	297.7	296.3	292.5
1200	332.1	324.1	297.8	296.5	292.4
1250	332.1	324.0	298.0	296.8	292.5
1300	332.1	324.4	298.6	297.4	293.0
1350	332.2	324.2	298.3	297.1	292.6
1400	332.1	324.1	298.4	297.1	292.7
1450	332.5	324.2	298.7	297.4	292.8
1500	333.0	324.4	299.2	297.8	292.8
1550	332.9	324.8	299.2	297.8	292.7
1600	332.6	324.8	299.6	298.2	293.0
1650	332.7	325.1	299.9	298.4	293.0
1700	332.9	324.7	299.6	298.3	292.9
1750	333.3	325.6	300.2	298.8	293.2
1800	332.4	325.4	300.0	298.7	292.8
1850	333.0	325.7	300.5	299.1	293.2
1900	333.2	325.8	300.4	299.0	292.9
1950	333.3	326.0	300.5	299.1	293.0
2000	333.3	326.1	300.6	299.2	293.0
2050	333.4	326.2	300.7	299.3	293.1
2100	333.5	326.4	300.8	299.4	293.1
2150	333.5	326.5	301.0	299.5	293.2
2200	333.6	326.7	301.1	299.6	293.2
2250	333.7	326.8	301.2	299.7	293.3
2300	333.7	326.9	301.3	299.8	293.3
2350	333.8	327.1	301.4	299.9	293.4
2400	333.9	327.2	301.5	300.0	293.4

Table G2. The measured fuel temperature changes in time (T_f) at various positions (r, z) in the ethanol fire.

Time [s]	T_f [K]	T_f [K]	T_f [K]	T_f [K]	T_f [K]	T_f [K]
r [cm]	13.2	3.7	11.1	3.7	11.1	3.7
z [cm]	-1.0	-1.4	-1.4	-4.0	-4.0	-8.0
-50	292.3	292.5	292.8	292.7	292.7	292.7
0	304.3	292.5	292.7	292.7	292.7	292.7

----- Table G2 **Continued on Next Page** -----

Time [s]	T_f [K]	T_f [K]	T_f [K]	T_f [K]	T_f [K]	T_f [K]
50	335.1	292.6	292.9	292.8	292.8	292.7
100	342.7	292.7	293.1	292.9	292.9	292.7
150	344.6	293.2	293.3	293.0	292.9	292.8
200	345.5	293.8	293.5	293.1	292.9	292.8
250	347.8	294.5	293.7	293.3	292.9	292.8
300	348.7	295.2	294.1	293.6	293.0	292.8
350	349.3	296.5	294.8	294.0	293.0	292.8
400	349.1	298.0	295.4	294.4	293.0	292.8
450	349.7	298.9	295.8	294.9	293.0	292.8
500	349.7	300.1	296.5	295.3	293.0	292.8
550	350.0	301.1	297.2	295.8	293.1	292.8
600	350.8	302.4	297.8	296.3	293.1	292.8
650	351.0	303.5	298.4	296.8	293.1	292.8
700	350.6	304.0	299.0	297.3	293.1	292.8
750	350.4	304.7	299.6	297.8	293.1	292.8
800	350.6	305.2	300.1	298.3	293.1	292.8
850	350.3	306.1	300.7	298.8	293.1	292.8
900	350.3	306.7	301.2	299.3	293.2	292.8
950	350.1	307.0	301.7	299.7	293.2	292.8
1000	350.7	307.8	302.2	300.1	293.2	292.9
1050	351.3	308.7	302.7	300.5	293.2	292.9
1100	350.9	309.1	303.1	300.9	293.2	292.9
1150	350.8	309.5	303.6	301.3	293.3	292.9
1200	351.1	310.6	303.8	301.6	293.3	292.9
1250	350.8	310.7	304.3	302.0	293.3	292.9
1300	350.8	310.6	304.7	302.3	293.3	292.9
1350	350.5	311.3	305.1	302.7	293.3	292.9
1400	350.5	311.8	305.4	303.0	293.3	292.9
1450	350.4	312.1	305.8	303.3	293.4	292.9
1500	350.3	312.5	306.1	303.6	293.4	292.9
1550	350.6	313.0	306.4	303.8	293.4	292.9
1600	351.0	313.3	306.7	304.2	293.5	292.9
1650	350.7	313.1	307.1	304.5	293.5	292.9
1700	351.0	313.7	307.3	304.7	293.5	293.0
1750	350.9	314.1	307.6	305.0	293.6	293.0
1800	350.9	314.2	307.8	305.2	293.6	293.0

----- Table G2 **Continued on Next Page** -----

Time [s]	T_f [K]	T_f [K]	T_f [K]	T_f [K]	T_f [K]	T_f [K]
1850	351.0	314.0	308.1	305.5	293.6	293.0
1900	351.1	314.8	308.3	305.7	293.6	293.0
1950	350.8	315.1	308.5	306.0	293.6	293.0
2000	350.9	314.9	308.8	306.1	293.7	293.0
2050	351.0	314.9	309.0	306.4	293.7	293.0
2100	351.6	315.5	309.2	306.6	293.7	293.0
2150	351.5	315.7	309.5	306.9	293.8	293.0
2200	351.4	316.1	309.7	307.1	293.8	293.0
2250	351.3	315.7	309.8	307.2	293.8	293.0
2300	351.2	315.9	310.0	307.4	293.9	293.1
2350	351.7	315.8	310.2	307.5	293.9	293.1
2400	351.2	316.2	310.4	307.7	294.0	293.1
2450	351.3	316.2	310.6	308.0	294.0	293.1
2500	351.3	316.5	310.8	308.3	294.0	293.1
3500	351.2	319.5	313.4	310.8	294.6	293.2
3550	351.5	319.3	313.5	310.9	294.6	293.2
3600	352.0	319.6	313.6	311.0	294.7	293.2
3650	351.9	319.5	313.7	311.2	294.7	293.2
3700	352.0	319.7	313.8	311.3	294.7	293.2
3750	351.6	319.8	313.9	311.3	294.7	293.2
3800	351.5	320.2	313.9	311.3	294.8	293.2
3850	351.5	320.0	314.0	311.5	294.8	293.3
3900	351.5	319.9	314.1	311.5	294.8	293.3
3950	351.6	320.2	314.2	311.7	294.9	293.3
4000	351.5	320.1	314.4	311.8	294.9	293.3

Table G3. The measured fuel temperature changes in time (T_f) at various positions (r, z) in the acetone fire.

Time [s]	T_f [K]	T_f [K]	T_f [K]	T_f [K]	T_f [K]	T_f [K]	T_f [K]	T_f [K]	T_f [K]
r [cm]	13.2	3.7	11.1	3.7	11.1	3.7	15	15	15
z [cm]	-1.0	-1.4	-1.4	-4.0	-4.0	-8.0	-1.0	-4.0	-8.5
-50	287.8	289.2	289.5	289.5	289.4	289.5	291.2	290.8	290.7
0	294.5	289.2	289.5	289.5	289.4	289.5	316.7	292.4	291.9
50	327.4	293.3	292.7	292.4	290.6	289.9	389.2	314.4	296.2
100	328.7	298.5	296.1	295.1	290.6	290.2	385.1	318.0	297.1

----- Table G3 **Continued on Next Page** -----

Time [s]	T_f [K]	T_f [K]	T_f [K]	T_f [K]	T_f [K]	T_f [K]	T_f [K]	T_f [K]	T_f [K]
150	329.2	302.4	299.5	297.7	291.0	290.5	381.1	319.7	297.5
200	329.6	305.4	301.9	300.1	291.7	290.8	385.2	321.4	298.3
250	329.7	307.7	304.1	302.2	292.0	291.0	379.1	322.5	298.9
300	329.7	309.9	305.9	303.9	292.5	291.2	383.8	322.8	298.4
350	329.8	311.6	307.5	305.4	292.7	291.4	376.7	323.5	299.0
400	329.8	312.7	308.9	306.8	293.3	291.6	380.9	324.5	299.7
450	329.9	314.1	310.2	308.0	293.7	291.8	379.3	325.0	300.0
500	329.8	315.2	311.4	309.1	294.1	292.0	379.3	325.6	300.4
550	329.8	316.4	312.5	310.2	294.5	292.1	384.4	326.6	301.0
600	329.9	317.0	313.3	311.1	294.8	292.4	378.4	326.7	301.3
650	330.1	318.2	314.2	312.0	295.3	292.5	376.5	327.3	301.7
700	330.1	319.2	315.1	312.8	295.6	292.7	383.9	327.8	302.2
750	330.1	319.9	315.9	313.7	296.0	292.8	378.7	328.2	302.6
800	330.0	320.3	316.7	314.4	296.4	292.9	376.5	328.8	303.0
850	330.1	321.4	317.5	315.1	296.8	293.1	379.4	329.4	303.4
900	330.1	322.2	318.2	315.9	297.1	293.2	384.6	330.1	304.0
950	330.0	322.5	318.9	316.6	297.5	293.4	385.0	330.6	304.2
1000	329.9	323.5	319.5	317.2	297.8	293.5	382.8	331.0	304.3
1050	329.9	323.5	319.9	317.6	298.1	293.7	382.2	331.3	304.9
1100	330.1	323.6	320.2	317.8	298.4	293.8	381.2	331.3	305.0
1150	330.0	323.6	320.3	318.0	298.6	294.0	377.9	330.8	305.2
1200	330.1	324.2	320.4	318.1	298.9	294.2	379.4	330.5	305.3
1250	330.1	323.9	320.5	318.3	299.1	294.4	380.2	330.6	305.7
1300	330.1	324.2	320.6	318.4	299.4	294.7	379.2	330.4	305.8
1350	330.1	324.0	320.6	318.5	299.6	294.9	379.2	330.3	306.0
1400	330.2	323.9	320.7	318.6	299.8	295.1	376.9	330.2	306.0
1450	330.2	324.3	320.8	318.7	300.1	295.2	378.4	330.5	306.7
1500	330.2	324.2	320.9	318.8	300.3	295.3	382.6	330.6	306.8
1550	330.3	324.3	321.0	318.9	300.5	295.5	377.7	330.5	306.8
1600	330.3	324.4	321.1	319.1	300.7	295.6	374.8	330.4	307.0
1650	330.4	324.4	321.2	319.2	300.9	295.8	374.0	330.2	307.1
1700	330.4	324.2	321.3	319.3	301.1	295.9	374.7	330.5	307.5
1750	330.5	324.7	321.4	319.4	301.3	296.0	374.6	330.4	307.5
1800	330.5	324.3	321.5	319.5	301.5	296.1	375.5	330.5	307.7
1850	330.4	324.5	321.6	319.7	301.7	296.2	374.9	330.4	307.9
1900	330.5	324.6	321.8	319.9	301.9	296.4	376.4	330.3	307.8

----- Table G3 **Continued on Next Page** -----

Time [s]	T_f [K]	T_f [K]	T_f [K]	T_f [K]	T_f [K]	T_f [K]	T_f [K]	T_f [K]	T_f [K]
1950	330.4	325.1	321.9	320.0	302.0	296.5	378.3	330.9	308.6
2000	330.4	324.9	322.2	320.2	302.2	296.6	374.2	331.0	308.7
2050	330.3	324.5	322.4	320.5	302.4	296.7	378.5	331.0	308.8
2100	330.6	325.7	322.7	320.7	302.7	296.9	377.1	331.4	309.0
2150	330.5	325.5	322.8	320.9	302.9	297.0	376.7	331.4	309.1
2200	330.6	325.8	323.0	321.1	303.0	297.1	375.2	331.6	309.2
2250	330.3	325.1	323.2	321.3	303.1	297.1	377.3	331.9	309.6
2300	330.2	325.5	323.3	321.4	303.3	297.2	378.9	332.0	309.7
2350	330.2	325.7	323.5	321.6	303.5	297.3	377.1	332.0	309.8
2400	330.1	325.6	323.8	321.9	303.7	297.4	375.1	332.0	309.9
2450	330.2	326.0	323.9	322.1	303.9	297.6	382.1	332.0	309.9
2500	330.8	327.5	324.2	322.3	304.1	297.7	380.5	332.2	310.1
2550	329.8	325.3	325.8	323.8	304.5	297.8	386.4	335.3	311.0
2600	381.9	327.5	328.3	326.0	305.1	298.0	386.1	336.8	311.6
2650	393.4	332.6	331.0	328.4	305.8	298.3	393.1	339.5	312.3
2700	397.4	333.2	333.5	331.2	306.5	298.4	397.0	342.1	313.2
2750	356.3	330.6	330.4	329.9	306.3	298.2	329.4	329.8	309.3
2800	317.1	306.0	326.5	326.7	306.6	298.2	319.3	323.0	309.5
2850	307.2	303.5	325.2	325.1	306.9	298.2	317.9	321.6	310.6
2900	302.7	302.3	323.0	323.0	307.1	298.2	315.6	319.4	310.5

Appendix H. Local Heat Flux Distribution

Tables H1 - H5 list the local radiative heat flux for each of the fires in the radial direction as a function of the vertical location at a distance (r) from the pool centerline and in the downward direction as a function of position in the radial direction at a *z*-location equal to the fuel surface or gas burner (see Fig. 7). The expanded (k=2) combined uncertainty, $U_c(\dot{q}'')$, scaled by a factor 2 from the $u_c(\dot{q}'')$ defined in Eq. F12.

Table H1. Local heat flux measurements in the radial and downward directions in the 30 cm methanol fire at a radial distance (r) from the centerline and axial distance (z) from the fuel surface.

Radial Direction				Downward Direction			
r [cm]	z [cm]	$\dot{q}''$ [kW/m^2]	$U_c(\dot{q}'')$ [kW/m^2]	r [cm]	z [cm]	$\dot{q}''$ [kW/m^2]	$U_c(\dot{q}'')$ [kW/m^2]
60	0	0.81	0.11	16.1	1	3.33	0.66
60	1	0.77	0.10	19	1	2.40	0.48
60	10	0.95	0.13	21.9	1	2.05	0.41

----- Table H1 Continued on Next Page -----

Radial Direction				Downward Direction			
r [cm]	z [cm]	$\dot{q}''$ [kW/m^2]	$U_c(\dot{q}'')$ [kW/m^2]	r [cm]	z [cm]	$\dot{q}''$ [kW/m^2]	$U_c(\dot{q}'')$ [kW/m^2]
60	14	0.90	0.12	23	1	2.05	0.41
60	20	0.98	0.13	30	1	1.19	0.24
60	30	0.90	0.12	38.8	1	0.72	0.14
60	40	0.83	0.11	47.2	1	0.47	0.093
60	50	0.71	0.095	56.5	1	0.32	0.063
60	60	0.55	0.074	66.2	1	0.24	0.048
60	70	0.46	0.061	75.7	1	0.18	0.036
60	80	0.37	0.050	150	1	0.04	0.0079
60	90	0.27	0.036	-	-	-	-
60	100	0.19	0.025	-	-	-	-
60	110	0.17	0.022	-	-	-	-
60	120	0.07	0.0094	-	-	-	-
60	130	0.00	0.0	-	-	-	-
83	20	0.55	0.073	-	-	-	-
83	50	0.46	0.062	-	-	-	-
83	80	0.30	0.040	-	-	-	-
83	110	0.21	0.028	-	-	-	-

Table H2. Local heat flux measurements in the radial and downward directions in the 30 cm ethanol fire at a radial distance (r) from the centerline and axial distance (z) from the fuel surface.

Radial Direction				Downward Direction			
r [cm]	z [cm]	$\dot{q}''$ [kW/m^2]	$U_c(\dot{q}'')$ [kW/m^2]	r [cm]	z [cm]	$\dot{q}''$ [kW/m^2]	$U_c(\dot{q}'')$ [kW/m^2]
183	1	0.20	0.027	18	1	5.21	0.38
183	35	0.17	0.023	22	1	3.62	0.29
183	97	0.13	0.018	47	1	0.76	0.12
183	158	0.10	0.013	85	1	0.19	0.015
183	219	0.07	0.0088	183	1	0.04	0.0060

Table H3. Local heat flux measurements in the radial and downward directions in the 30 cm acetone fire at a radial distance (r) from the centerline and axial distance (z) from the fuel surface.

Radial Direction				Downward Direction			
r [cm]	z [cm]	$\dot{q}''$ [kW/m^2]	$U_c(\dot{q}'')$ [kW/m^2]	r [cm]	z [cm]	$\dot{q}''$ [kW/m^2]	$U_c(\dot{q}'')$ [kW/m^2]
184	1	0.38	0.050	18	1	7.09	0.54

----- Table H3 **Continued on Next Page** -----

Radial Direction				Downward Direction			
r [cm]	z [cm]	$\dot{q}''$ [kW/m^2]	$U_c(\dot{q}'')$ [kW/m^2]	r [cm]	z [cm]	$\dot{q}''$ [kW/m^2]	$U_c(\dot{q}'')$ [kW/m^2]
184	35	0.30	0.041	22	1	5.20	0.39
184	97	0.26	0.035	48	1	1.42	0.12
184	158	0.20	0.026	81	1	0.48	0.038
184	219	0.14	0.019	184	1	0.10	0.0070

Table H4. Local heat flux measurements in the radial and downward directions in the 37 cm methane fire at a radial distance (r) from the centerline and axial distance (z) from the fuel surface.

Radial Direction				Downward Direction			
r [cm]	z [cm]	$\dot{q}''$ [kW/m^2]	$U_c(\dot{q}'')$ [kW/m^2]	r [cm]	z [cm]	$\dot{q}''$ [kW/m^2]	$U_c(\dot{q}'')$ [kW/m^2]
177	0	0.18	0.025	24	0	2.47	0.22
177	25	0.15	0.019	29	0	1.79	0.16
177	86	0.13	0.017	54	0	0.47	0.048
177	147	0.09	0.011	89	0	0.12	0.012
177	209	0.06	0.0083	177	0	0.02	0.0038

Table H5. Local heat flux measurements in the radial and downward directions in the 20 kW, 34 kW, and 50 kW propane fires at a radial distance (r) from the centerline and axial distance (z) from the fuel surface.

			$\dot{Q}$ = 20.7 kW		$\dot{Q}$ = 34.4 kW		$\dot{Q}$ = 50.1 kW	
Direction	r [cm]	z [cm]	$\dot{q}''$ [kW/m^2]	$U_c(\dot{q}'')$ [kW/m^2]	$\dot{q}''$ [kW/m^2]	$U_c(\dot{q}'')$ [kW/m^2]	$\dot{q}''$ [kW/m^2]	$U_c(\dot{q}'')$ [kW/m^2]
Radial	177	0	0.10	0.014	0.28	0.037	0.46	0.061
	177	25	0.083	0.011	0.22	0.030	0.37	0.050
	177	86	0.067	0.0090	0.19	0.026	0.33	0.044
	177	147	0.061	0.0082	0.18	0.025	0.33	0.044
	177	209	0.041	0.0055	0.11	0.015	0.20	0.026
Downward	24	0	1.5	0.10	3.3	0.22	4.9	0.33
	29	0	1.0	0.070	2.4	0.16	3.7	0.25
	54	0	0.21	0.014	0.66	0.044	1.2	0.080
	89	0	0.058	0.0039	0.20	0.013	0.39	0.026
	177	0	0.013	8.7E-4	0.048	0.0032	0.093	0.0062

Appendix I. Summary of References Associated with Table 1.

Table I1 lists the references that provide detailed descriptions of the measurement results and uncertainty analysis of the global and local parameters that are associated with each of the entries in Table 1. Reference to a previously studied steadily burning 100 cm pool fire is also included.

Table I1. List of references that provide descriptions of the measurements and uncertainty analysis associated for the eight pool fires considered in Table 1. Information on a 100 cm methanol pool fire is also listed.

	Fuel	Methanol	Ethanol	Acetone	Heptane	Methane	Propane	Propane	Propane	Methanol
	Nominal pool diameter (cm)	**30**	**30**	**30**	**30**	**100**	**37**	**37**	**37**	**100**
	Idealized heat release rate (kW)	**19.1**	**26.1**	**38.0**	**112.2**	**34.5**	**20.7**	**34.4**	**50.1**	**249**
	Measurement									
Global	**Mass burning flux**	[5, 7-9, 11, 44-46, 53-58]	[5, 11, 45, 46, 53]	[5, 11, 45, 46, 53]	[8, 9, 46]	[46]	[46]	[46]	[46]	[38, 45]
	Flame height	[8, 46, 53, 58]	[46]	[46]	[8, 46]	[46, 59]	[46]	[46]	[46]	[9, 38]
	Puffing frequency	[7, 8, 46, 54, 55]	[46]	[46]	[8]	[46]	[46]	[46]	[46]	[38]
	CO yield	[46]	[46]	[46]	[46]	[46]	[46]	[46]	[46]	[46]
	Soot yield	[46]	[46]	[46]	[46]	[46]	[46]	[46]	[46]	[46]
	Radiative fraction	[8, 9, 45, 46]	[46]	[46]	[9, 46]	[31, 46]	[31, 46]	[31, 46]	[46]	[9, 38]
	Total heat flux to pool surface	[11]	[11]	[11]	[8]	[31, 46]	[31, 46]	[31, 46]	[31, 46]	na
Local	**Gas-phase temp profile**	[7, 46]	[40, 46]	[38, 46]	[46]	[46]	[46]	[46]	[46]	[38]
	Gas-phase velocity profile	[7, 46]	[46]	[38, 46]	[46]	[46]	[46]	[46]	[46]	[38]
	Radiative flux to surroundings	[11, 46]	[46]	[46]	[46]	[46]	[46]	[46]	[46]	[38]
	Radiative flux onto fuel surface	[11]	[11]	[11]	[8]	[46]	[46]	na	na	[38]
	Heat flux profile on fuel surface	[11]	[11]	[11]	[8]	[46]	[46]	na	na	[38]
	Fuel surface temperature	[46]	[46]	[46]	[46]	[46]	[46]	[46]	[46]	[38]
	In-depth liquid fuel temperature	[46]	[46]	[46]	[46]	[46]	na	na	na	[38]

- Parameters indicated by “na” are not available.
- Ref.[46] is NIST Technical Note 2162 and its revision 1 (this report).